6-30-2016

# The Development Of A High Resolution Deep-UV Spatial Heterodyne Raman Spectrometer

Nirmal Lamsal
*University of South Carolina*

## Recommended Citation

Lamsal, N.(2016). *The Development Of A High Resolution Deep-UV Spatial Heterodyne Raman Spectrometer.* (Doctoral dissertation). Retrieved from https://scholarcommons.sc.edu/etd/3422

# The Development of a High Resolution Deep-UV Spatial Heterodyne Raman Spectrometer

by

Nirmal Lamsal

Master of Science
Tribhuvan University, 2008

---

Submitted in Partial Fulfillment of the Requirements

For the Degree of Doctor of Philosophy in

Chemistry

College of Arts and Sciences

University of South Carolina

2016

Accepted by:

S. Michael Angel, Major Professor

Donna A. Chen, Committee Member

Hui Wang, Committee Member

MVS Chandrashekhar, Committee Member

Lacy Ford, Senior Vice Provost and Dean of Graduate Studies

# Dedication

I dedicate this work to my parents who relentlessly helped me in every step of my life to achieve my goals.

# Acknowledgements

First and foremost, I would like to express my heartfelt gratitude to my advisor Dr. S. Michael Angel for giving me an opportunity to pursue an excellent research work in his lab. I am grateful to him for his guidance, support and exceptional supervision throughout my graduate career, without which I would not have been able to complete the difficult journey of the graduate program. The knowledge, skills, and thoughtfulness that I have learned from him will always help me move forward in the future.

I would also like to thank my committee members, Dr. Donna A Chen, Dr. Hui Wang and Dr. MVS Chandrasekhar for serving on my committee. Their constructive criticism and feedback helped me be a better researcher.

Thank you to my lab mates in the Angel group, past and present. I would like to start with Janna Register, she was very friendly and has always been a great help no matter the task or circumstance. Nate Gomer, thank you for all support and mentoring me early on in my career. Thanks to Joseph Bonvallet, Alicia Strange, Pattrick Barnet, Josh Hungtington and Ashely Allen for your support and guidance throughout years. I learned a lot from you and I feel proud to be a part of such a nice group.

Special thanks go to Dr. Shiv K Sharma, one of our collaborators from the University of Hawaii for giving me a wonderful opportunity to conduct a significant part of my research work in his lab. I also owe my sincere gratitude to his student Tayro Acosta for assisting me throughout my time at the University of Hawaii.

# Abstract

Raman spectroscopy is a light scattering technique that has a huge potential for standoff measurements in applications such as planetary exploration because a Raman spectrum provides a unique molecular fingerprint that can be used for unambiguous identification of target molecules. For this reason, NASA has selected a Raman spectrometer as one of the major instruments for its new Mars lander mission, Mars 2020, in the search for biomarkers that would be the indicators of past or present life. Raman scattering is strongest at UV wavelengths because of the inherent increase in the Raman cross section at shorter wavelengths and because of the possibility of UV resonance enhancement. Thus, a Raman spectrometer for planetary exploration would ideally be a UV instrument. However, existing UV Raman spectrometers are not optimal to integrate for planetary exploration because they are large and heavy. Existing UV Raman spectrometers also offer very low light throughput due to the need for narrow entrance slits to provide high spectral resolution.

This thesis discusses the development of a new type of Fourier transform (FT) Raman spectrometer; a spatial heterodyne Raman spectrometer (SHRS), which offers several advantages for field-based UV Raman applications. The SHRS generates a spatial interferogram using stationary diffraction gratings and an imaging detector. The SHRS is lightweight, contains no moving parts, and allows very high spectral resolution Raman measurements to be made in an exceptionally small package, even in the deep UV.

In this study, for the first time, we developed a SHRS system for deep UV applications using 244 nm excitation that has a spectral resolution less than 5 $cm^{-1}$ and a spectral bandpass of 2600 $cm^{-1}$. Raman spectra of several liquid and solid compounds were measured using a 244 nm laser to demonstrate the spectral resolution and range of the system. The SHRS has a large entrance aperture and wide collection angle, which was shown to be beneficial for the deep UV measurements of photosensitive materials like $NH_4NO_3$ by using a large laser spot size with low laser irradiance on the sample. This is not possible using conventional UV Raman systems where the need to focus the laser on sample often leads to photodecomposition. In addition, the use of deep-UV excitation to mitigate fluorescence was demonstrated by measuring Rh6G, a highly fluorescent compound, in acetonitrile solution. We also evaluated the performance of the SHRS for standoff Raman measurements in ambient light conditions using pulsed lasers and a gated ICCD detector. Standoff UV and visible Raman spectra of a wide variety of materials were measured at distances of 3-18 m, using 266 nm and 532 nm pulsed lasers, with 12.4” and 3.8” aperture telescopes, respectively. We observed that the wide acceptance angle of the SHRS simplifies optical coupling of the spectrometer to the telescope and makes alignment of the laser on the sample easier. More recently, we improved the SHRS design by replacing the cube beamsplitter with a custom-built higher quality plate beamsplitter, designed to operate in the range of 240-300 nm, with higher transmission, higher surface flatness and better refractive index homogeneity. The new design addresses two major issues of the previous UV SHRS design, namely, optical losses and poor fringe visibility; as a result, the Raman spectra obtained with new design have much higher signal to noise ratio than the measurements made using previous design.

## Table of Contents

# List of Tables

# List of Figures

# Chapter 1

## General Discussion of Deep UV Raman Spectroscopy

### 1.1 Introduction

The phenomenon of inelastic scattering of light was first discovered by Indian Professor C. V Raman in 1928,[1] for which he was awarded the Nobel Prize in Physics in 1930. Raman spectroscopy is a non-destructive vibrational technique that provides detailed molecular and structural information of the sample under investigation. The technique is based on the inelastic scattering of the light, where a photon interacts with matter to produce scattered radiation at different wavelengths or frequencies. Since, the difference in frequency corresponds to the vibrational or rotational energy level of a molecule, the Raman spectrum can be treated as a molecular "fingerprint" and can be used to determine molecular structure.

Although highly versatile, historically, the technique of Raman spectroscopy was limited to a few sophisticated research labs and was rarely used for 'real-world' chemical analysis because of fundamental and technical limitations, including extremely weak Raman intensity, fluorescence interference, and the unavailability of efficient light collection and detection systems. In recent years, instrumental and technological developments such as the invention of charge coupled device (CCD) detectors, holographic optical filters, and efficient spectrometers have led to major improvements in Raman spectrometers. As a result, the technique is widely used today in many applications including pharmaceutical analysis,[2–4] explosive detection,[5–10] forensic science,[11–13] and planetary exploration[14–19], biochemistry and medical applications etc. Raman is beneficial for these applications because it is a non-invasive *in situ* technique that does not require sample preparation and provides accurate chemical information for the samples in many forms (gas, liquid or solid state).

## 1.2 Raman Theory

Raman spectroscopy is an inelastic light scattering technique, in which the sample is excited from the ground state energy level to a higher, shorter-lived virtual state by illuminating with a monochromatic light source, typically a laser with wavelength $\lambda_o$ or frequency $\nu_o$. Most light scattering take place with no loss in energy, and therefore no frequency ($\nu_o$). This is known as Rayleigh or mie scattering. However, a very small fraction of light (1 in every $10^6$-$10^8$ photons)[20] scatter with a loss of energy to the molecule and this is known as Raman scattering. As illustrated in Fig. 1.1, Raman scattered photons are shifted in frequencies (i.e. Raman shift) because the excitation photon energy is either transferred to or received from the sample, as a result of a change in vibrational or rotational modes of the molecules in the sample. Photons with lower energy ($\nu_o - \nu_m$) than the incident photon are known as Stokes Raman photon, while the photon with higher energy ($\nu_o + \nu_m$) are known as anti-Stokes Raman photons. Raman spectra are plotted as scattered light intensity versus Raman shift, ($\Delta$ cm$^{-1}$), the energy difference between the laser photons and the Raman scattered photons. Elastically scattered light is removed using a combination of extremely narrow band notch filters and proper design of the spectrograph.

Although IR and Raman are both vibrational "fingerprint" techniques, the selection rules are different. Raman requires a change in molecular polarizability while IR requires a change in the dipole moment during a normal mode of vibration. Due to the different selection rules, many molecules, which are not IR active such as $H_2$, $N_2$, and $O_2$, which can be measured using Raman spectroscopy. By the same token, Raman spectroscopy can be used to measure bands of symmetric linkages such as -S-S-, -C-S-, -C=C-, which are weak in an infrared spectrum.[20]

## 1.3 Raman Instrumentation

A typical Raman system consists of four major components: a monochromatic light source to excite the sample, filtering and collection optics to collect the scattered light of specific interest, a spectrometer to disperse the light into its spectral components, and a detector to record the spectrum. In the following section, each of the components are described in detail.

### 1.3.1 Excitation Source

Since Raman cross sections are very low, a powerful light source is required to produce sufficient Raman scattered photons. Although the first Raman measurements were made using sunlight,[1] all modern Raman spectrometers use lasers exclusively as the light source. Lasers are ideal for Raman spectroscopy because they are highly monochromatic, possess low divergence, and are therefore easy to collimate, can provide high power density on the sample and most importantly are available in the wavelength regions ranging from UV to IR. Both CW and pulsed lasers are used for Raman. Pulsed lasers combined with gated detectors have been shown to be very effective in eliminating background light while conducting the Raman measurements in ambient light conditions.[7] The proper selection of laser wavelength is a critical for the success of Raman spectroscopy. Raman cross section is inversely proportional to the fourth power of excitation wavelength ($1/\lambda^4$). thus shorter wavelengths can yield higher Raman signals.[21] Therefore, visible wavelengths are most commonly used in Raman. Also, visible lasers produce relatively high power and are cost effective. However, a strong fluorescence background, from either the analyte or impurities, can be a significant problem when using visible excitation. Lower energy NIR wavelengths reduce the likelihood of fluorescence background but are not very desirable, because the Raman scattering is inherently weak. Deep-UV excitation can be used to avoid fluorescence interference, while preserving the sensitivity of the system, as the Raman shift occurs in a spectral region far from fluorescence wavelengths. The use of UV excitation, however, is limited to a few applications largely due to laser-induced damage to the sample, the lack of suitable UV transmissive optics, and larger, more complex, and expensive UV lasers.

### 1.3.2 Filtering and Collection optics

With Raman scattering, being a very weak phenomenon, a big part of experimental effort goes into setting up the excitation and collection optics to gather as much scattered light as possible. Typically, lenses are used to focus the laser onto the sample and to collect the scattered radiation. Either a single lens or a combination of lenses can be used to transfer the light into the spectrometer. Normally, $90^o$ collection geometry is used for transparent liquids, whereas $180^o$ backscattering collection geometry is typically employed for opaque samples. The light gathering capacity of a lens is defined in terms of an F-number (F#), which is the ratio of focal length (f) to diameter (D) of the lens (i.e., F#=f/D).

It is necessary to match the F# of the lens with the spectrometer in order to maximize the optical throughput. Fiber optic cables are also employed to collect light, mainly in handheld instruments and for online monitoring, and *in-situ* analysis.[22,23] Fiber optic systems consist of single fiber or multiple fibers, where one fiber delivers the laser to the sample and adjacent fibers collects and transmit the scattered light into the spectrometer. In remote Raman measurements, telescopes are employed to compensate for the decrease in signal due to sample distance. The telescope is coupled to the spectrometer either through fiber optics or using intermediate lenses.[24,25] Standoff measurements are of great benefit for hazardous samples such as explosives[5,7,8,26,27], where direct contact could be potentially harmful or for planetary exploration,[17,19,24] to extend the range over which the samples are accessible.

Since most of the scattered photons have the same frequency as the laser (Rayleigh scattering), it is essential to block these photons from entering the system. Usually, notch filters or long pass filters are incorporated to block laser scattered light while transmitting Raman scattered light. Notch filters blocks a small wavelength band, a few nanometers wide, centered on the laser wavelength. This allows both Stokes and anti-Stokes band to be recorded, while blocking the Rayleigh scattered light.

### 1.3.3 Spectrometers

The available spectrometers for Raman systems can be divided into two categories; dispersive grating based spectrometers and Fourier transform interferometers. In dispersive system, the collected light is first focused onto the entrance slit of the spectrometer, which is then collimated by a concave mirror or lens and directed to a diffraction grating. The light is dispersed into its component wavelengths, a small bandpass of which is then allowed to exit towards the detector. The extent of dispersion depends on the gratings groove density and the focal length of the spectrometer. Although optically efficient, the tradeoff between the resolution and sensitivity sometimes create difficulty implementing dispersive spectrometer especially for high-resolution measurements. The Fourier transform (FT) Raman uses multiplex spectrometer such as Michelson interferometer, which measure all wavelengths of light simultaneously producing interferogram as output. The intensity spectrum is then recovered by applying Fourier transformation to the interferogram. Unlike dispersive spectrometers, the noise from each of the wavelengths are distributed throughout the spectrum. Therefore, it is essential to block any scattered light like laser, fluorescence or any out of band light for successful operation of FT interferometer. FT Raman spectroscopy was first developed by Hirschfeld and Chase[28] and used infrared excitation to avoid fluorescence background. The less energetic IR excitations were difficult to implement with dispersive spectrometers because of the shot noise limited detectors[29], such as PMT, which had very low quantum efficiency in IR.

### 1.3.4 Detectors

The charge coupled device (CCD) and the intensified charge coupled device (ICCD) are the preferred detectors for low light measurements such as for Raman spectroscopy. Both have a two dimensional array of pixels to store and manipulate the photons in the form of electrical charges. The choice of the CCD detectors depends on the excitation wavelength, spectral range, sensitivity and speed of the data acquisition. The properties that influence the performance of CCD detectors include quantum efficiency, number of channels, dark noise and readout noise. Most of the modern CCD detectors possess extremely low thermal and readout noise (i.e., shot noise limited) and have high quantum efficiency from UV to IR. They can also record a full Raman spectrum in a single measurement, typically without scanning the spectrometer. The two dimensional CDD array also allows to perform spatial resolution of the sample and can be used to take the full image of the sample.

## 1.4 UV Raman Spectroscopy

As stated previously, there are several advantages using UV excitation in Raman spectroscopy. Short wavelength excitation can provide richest Raman sensitivity, since the Raman scattering efficiency is proportional to $1/\lambda^4$. [21] Also, there is a possibility of resonance enhancement, which occurs when excitation wavelength is close to the wavelength of an electronic state within the molecule. Many organic and inorganic materials show resonance enhancement[30,31] up to $10^6$ times when excited in the deep-UV. As an example of increased sensitivity in the UV, Fig. 2 compares Raman spectra of argenine measured using both 532-nm and 244-nm excitation. The 244-nm Raman spectral intensity was 4670 times higher for argenine using 244-nm excitation because of the $1/\lambda^4$ scattering efficiency dependence and resonance effects, in addition to lower fluorescence using UV excitation. In addition to enhanced Raman scattering, fluorescence suppression is an advantage at deep UV wavelengths, since the Raman spectrum will be shifted to wavelengths below the longer wavelength fluorescence.[32] Fluorescent samples will still fluoresce, but the fluorescence will appear at wavelengths that are far removed from the Raman bands and thus the two signals can be completely isolated using optical filters.

There are many practical difficulties and disadvantages using UV for Raman measurements. A major disadvantage of UV excitation is photo-and thermal-degradation of the sample. Some solutions to this problem include the use of low laser power, moving the sample rapidly, or using a large laser spot size on the sample to reduce laser irradiance. Low laser power would produce a less Raman signal, and moving the sample is possible, but not desirable for field based standoff measurements. Using a large laser spot size is also not compatible with existing slit-based UV Raman spectrometers. Moreover, the Raman spectral window occurs over a narrow range of wavelengths when excited in the UV. Existing grating based UV spectrometers, therefore, incorporate narrow entrance slits, long focal length optics and large gratings to achieve the resolution required to separate the light into small wavelength regions. This tends to make UV spectrometers large and heavy with low light throughput, limiting the prospective of UV Raman for field applications, where available space is a concern. In this perspective, the spatial heterodyne Raman spectrometer (SHRS) looks promising for UV Raman measurements, which has potential to resolve a number of issues related to deep UV excitations. The system design and its applications will be discussed in the next several chapters.

## 1.5 References

1. C.V. Raman, K.S. Krishnan. “A New Type of Secondary Radiation”. Nature. 1928. 121(3048): 501–502.

2. T. Vankeirsbilck, A. Vercauteren, W. Baeyens, G. Van der Weken, F. Verpoort, G. Vergote, “Applications of Raman spectroscopy in pharmaceutical analysis”. TrAC Trends Anal. Chem. 2002. 21(12): 869–877.

3. B. D. Patel, P. J. Mehta. “An Overview: Application of Raman Spectroscopy in Pharmaceutical Field”. Curr. Pharm. Anal. 2010. 6(2): 131–141.

4. S. Sasic, Pharmaceutical applications of Raman spectroscopy. Wiley-Interscience, Hoboken, N.J, 2008.

5. K.L. McNesby, R.A. Pesce-Rodriguez. “Applications of Vibrational Spectroscopy in the Study of Explosives”. In: J.M. Chalmers, P.R. Griffiths, editors. Handbook of Vibrational Spectroscopy. John Wiley & Sons, Ltd, Chichester, UK, 2006.

6. K.L. McNesby, C.S. Coffey. “Spectroscopic Determination of Impact Sensitivities of Explosives”. J. Phys. Chem. B. 1997. 101(16): 3097–3104.

7. J.C. Carter, S.M. Angel, M. Lawrence-Snyder, J. Scaffidi, R.E. Whipple, J.G. Reynolds. “Standoff Detection of High Explosive Materials at 50 Meters in Ambient Light Conditions Using a Small Raman Instrument”. Appl. Spectrosc. 2005. 59(6): 769–775.

8. S. Sadate. “Standoff Raman Spectroscopy of Explosive Nitrates Using 785 nm Laser”. Am. J. Remote Sens. 2015. 3(1): 1-10.

9. M.L. Ramírez-Cedeño, N. Gaensbauer, H. Félix-Rivera, W. Ortiz-Rivera, L. Pacheco Londoño, S.P. Hernández-Rivera. “Fiber Optic Coupled Raman Based Detection of Hazardous Liquids Concealed in Commercial Products”. Int. J. Spectrosc. 2012. 2012:1–7.

10. G. Tsiminis, F. Chu, S. Warren-Smith, N. Spooner, T. Monro. “Identification and Quantification of Explosives in Nanolitre Solution Volumes by Raman Spectroscopy in Suspended Core Optical Fibers”. Sensors. 2013. 13(10): 13163–13177.

11. F.J. Bergin. “A microscope for fourier transform Raman spectroscopy”. Spectrochim Acta Part Mol. Spectrosc. 1990. 46(2): 153–159.

12. A.H. Kuptsov. “Applications of Fourier transform Raman spectroscopy in forensic science”. J. Forensic Sci. 1994. 39(2).

13. E.G. Bartick, P. Buzzini. “Raman Spectroscopy in Forensic Science”. In: R.A. Meyers, editor. Encyclopedia of Analytical Chemistry. John Wiley & Sons, Ltd, Chichester, UK, 2009.

14. National Research Council (U.S.), National Research Council (U.S.), eds. Vision and voyages for planetary science in the decade 2013-2022. National Academies Press, Washington, D.C, 2011.

15. Wang, B.L. Jolliff, L.A. Haskin. “Raman spectroscopic characterization of a highly weathered basalt: Igneous mineralogy, alteration products, and a microorganism”. J. Geophys. Res. 1999. 104 (E11): 27067.

16. P. Vandenabeele, J. Jehli ka. “Mobile Raman spectroscopy in astrobiology research”. Philos. Trans. R. Soc. Math. Phys. Eng. Sci. 2014. 372(2030): 20140202–20140202.

17. N. Tarcea, T. Frosch, P. Rösch, M. Hilchenbach, T. Stuffler, S. Hofer, et al. “Raman Spectroscopy—A Powerful Tool for in situ Planetary Science”. Space Sci. Rev. 2008. 135(1-4): 281–292.

18. S.E. Jorge Villar, H.G.M. Edwards. “Raman spectroscopy in astrobiology”. Anal. Bioanal. Chem. 2006. 384(1): 100–113.

19. S.M. Angel, N.R. Gomer, S.K. Sharma, C. McKay. “Remote Raman Spectroscopy for Planetary Exploration: A Review”. Appl. Spectrosc. 2012. 66(2): 137–150.

20. E. Smith, G. Dent. Modern Raman spectroscopy: a practical approach. J. Wiley, Hoboken, NJ, 2005.

21. R.L. McCreery. Raman spectroscopy for chemical analysis. John Wiley & Sons, New York, 2000.

22. I.R. Lewis, M.L. Lewis. “Fiber-Optic Probes for Raman Spectrometry”. In: J.M. Chalmers, P.R. Griffiths, editors. Handbook of Vibrational Spectroscopy. John Wiley & Sons, Ltd, Chichester, UK, 2006.

23. R.L. McCreery, M. Fleischmann, P. Hendra. “Fiber optic probe for remote Ramanspectrometry”. Anal. Chem. 1983. 55(1): 146–148.

24. S.K. Sharma. “New trends in telescopic remote Raman spectroscopic instrumentation”. Spectrochim. Acta. A. Mol. Biomol. Spectrosc. 2007. 68(4): 1008–1022.

25. S.M. Angel, N.R. Gomer, S.K. Sharma, C. McKay. “Remote Raman Spectroscopy for Planetary Exploration: A Review”. Appl. Spectrosc. 2012. 66(2): 137–150.

26. M. Gaft, L. Nagli. “UV gated Raman spectroscopy for standoff detection of explosives”. Opt. Mater. 2008. 30(11): 1739–1746.

27. J. Moros, J.A. Lorenzo, K. Novotný, J.J. Laserna. “Fundamentals of stand-off Raman scattering spectroscopy for explosive fingerprinting: Raman scattering spectroscopy for explosive fingerprinting”. J. Raman Spectrosc. 2013. 44(1): 121–130

28. T. Hirschfeld, B. Chase. “FT-Raman spectroscopy: development and justification”. Appl. Spectrosc. 1986. 40(2): 133–137.

29. B. Chase. “FT–Raman Spectroscopy: A Catalyst for the Raman Explosion?” J. Chem. Educ. 2007. 84(1): 75.

30. S.A. Asher. “Ultraviolet Raman Spectrometry”. In: J.M. Chalmers, P.R. Griffiths, editors. Handbook of Vibrational Spectroscopy. John Wiley & Sons, Ltd, Chichester, UK, 2006.

31. M. Ghosh, L. Wang, S.A. Asher. “Deep-Ultraviolet Resonance Raman Excitation Profiles of $NH_4NO_3$, PETN, TNT, HMX, and RDX”. Appl. Spectrosc. 2012. 66(9): 1013–1021.

32. S. Asher, C. Johnson. “Raman spectroscopy of a coal liquid shows that fluorescence interference is minimized with ultraviolet excitation”. Science. 1984. 225(4659): 311–313.

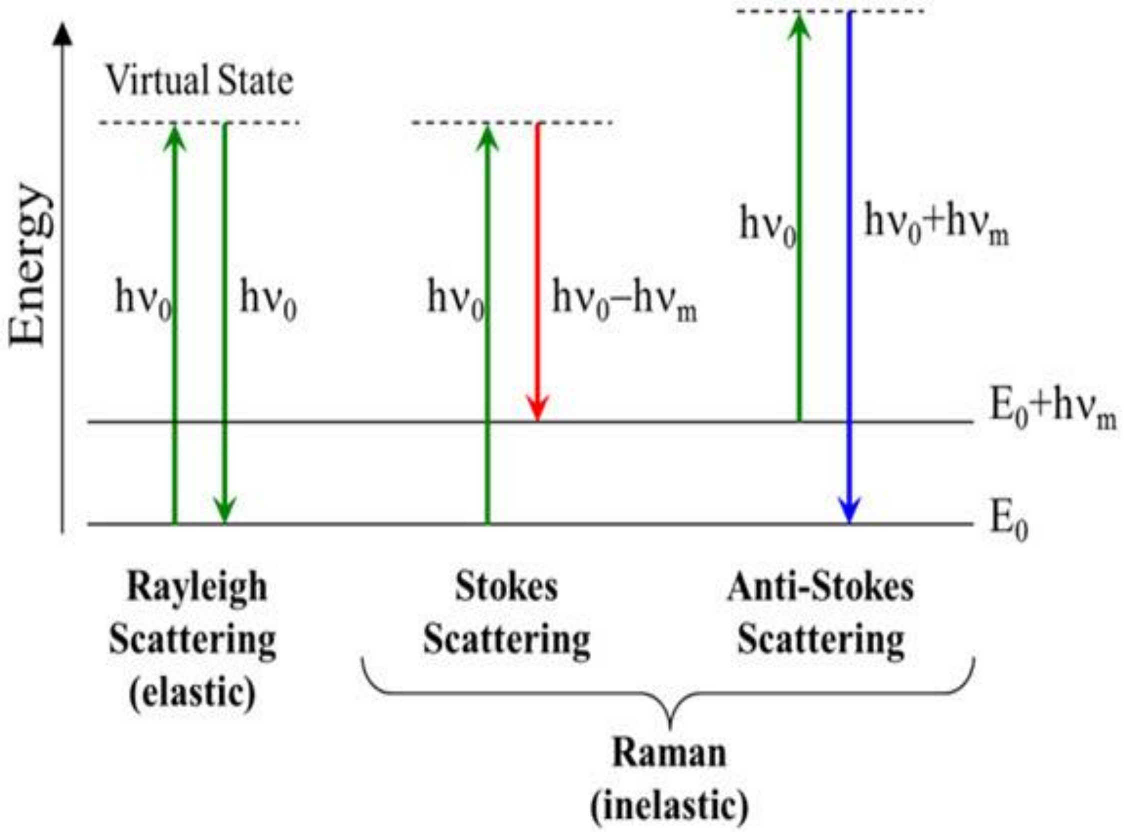

Figure 1.1. Energy level diagram showing energy transitions for Rayleigh and Raman. The energy changes that produce stokes and anti-Stokes emissions are depicted in the middle and in the right respectively. The two differ from the Rayleigh radiation with frequencies corresponding to νm, the energy of the first vibrational level of the ground state.

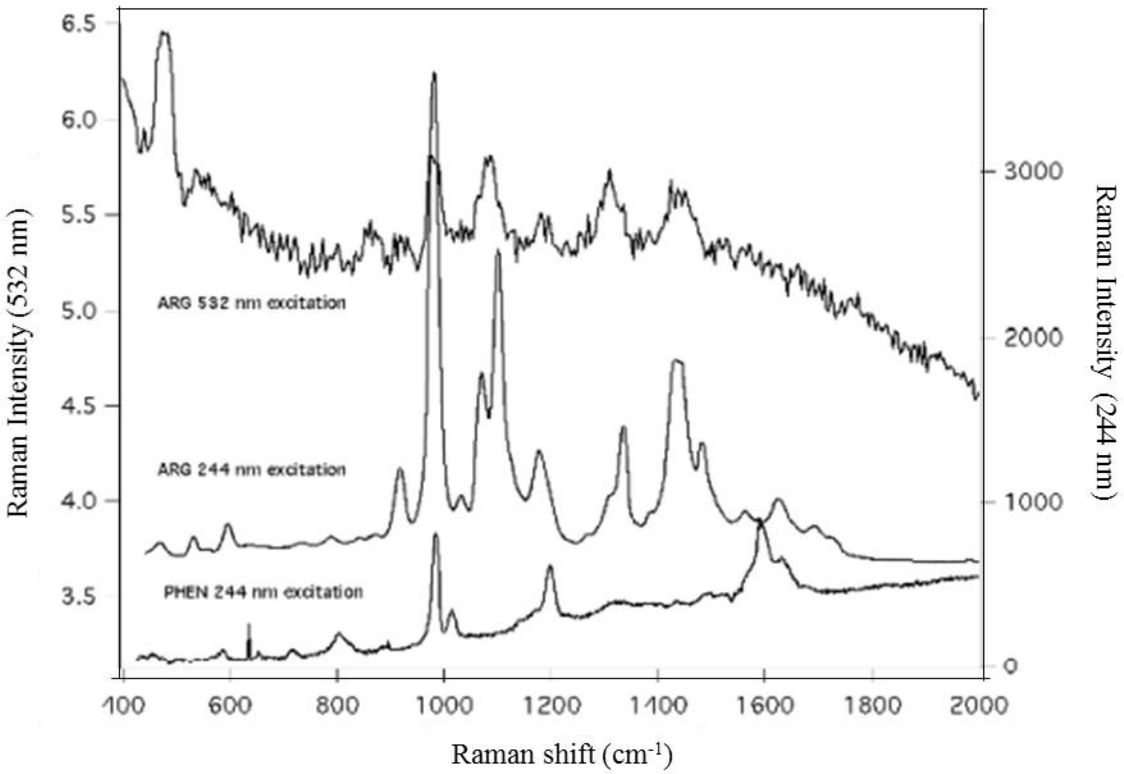

Figure 1.2. Raman Spectra of argenine using 532nm (top) and 244 nm laser excitation, and phenylalanine (lower) using 244 nm laser excitation. The spectra were measured in Angel's lab.

# Chapter 2

## Spatial Heterodyne Raman Spectroscopy

This chapter describes the working principle, design, and development of the spatial heterodyne spectrometer for Raman measurements. The first part of the chapter discusses the interferometer and the design considerations of two-beam interferometers. The second part of the chapter describes the details of various aspects of the spatial heterodyne Raman spectrometer including resolving power, bandpass, optical throughput and instrumentation.

### 2.1 Introduction to Interferometry

Interferometry refers to techniques, in which electromagnetic waves, such as light waves are combined to produce an interference pattern, which contains information about the original waves. Interferometry is based on the superposition principle, which means when two oscillating electromagnetic waves with the same frequency interfere with each other; the resulting pattern at some point in space is determined by the phase or the path difference between the two waves. [1] If two waves are in phase they will reinforce each other, and undergo constructive interference; waves that are out of phase will cancel each other, and undergo destructive interference. An instrument based on this technique is known as interferometer and has numerous applications in astronomy, spectroscopy, quantum mechanics, remote sensing, seismology, nuclear and particle physics.[1] Although physicist Thomas Young led the way for interferometry from his double slit experiments performed in 1801, a major breakthrough in interferometry was brought about by Albert Michelson and Morley in 1887[2] from their famous failed experiment where they attempted to detect luminiferous aether using the Michelson interferometer. Their failed experiments changed the way scientists view the workings of the universe.

The Michelson interferometer is the most widely used interferometer to date and works by splitting a beam of light into two beams. The light reflects by using two mirrors back towards the beamsplitter where it recombines to create an interference pattern. Spectroscopic techniques based on interferometry such as FTIR and FT-Raman[3] have several advantages over conventional grating based spectrometers. Interference spectrometers enjoy much higher light throughput as they lack an entrance slit, and are therefore useful to make measurements of faint and extended sources. [4] Additionally, interferometers measure all wavelengths simultaneously and a high resolving power can be attained in a very small package, which is rather difficult to achieve in grating based spectrometer.[3]

## 2.2 Theoretical Consideration to Interferometry

Interference is the phenomenon that occurs when the light is combined in space. The phenomenon can be defined more explicitly using the classical wave theory of light. Light is an electromagnetic wave made up of oscillating electric and magnetic fields, however, only electric field (E) is relevant to optics. Even more accurately, it is the field intensity, or, the time average of the electric field intensity squared, $E * E = E^2$, which is of most importance in optics. This value, also known as irradiance (I), is actually sensed by a detector. If we consider two coherent electromagnetic waves, with amplitude $E_0$ and the angular frequency (ω), emanating from two sources very close to each other, then the electric field of two waves at some point in space would be:

$$E_1 = E_0 \sin \omega t \qquad (1)$$

$$E_2 = E_0 \sin (\omega t + \phi) \qquad (2)$$

Where, ϕ is the phase difference between two waves. The sum of the combined electric field during interference is given by,

$$E = E_1 + E_2 = E_0 \sin \omega t + E_0 (\sin \omega t + \phi) \qquad (3)$$

Using the trigonometric identity,

$$\sin A + \sin B = 2 \sin \frac{(A+B)}{2} \cos \frac{(A-B)}{2}$$

and considering, A= ωt +ϕ, B= ωt, Eq. 3 can be written in the form:

$$E = 2E_0 \cos\left(\frac{\phi}{2}\right) \sin\left(\omega t + \frac{\phi}{2}\right) \qquad (4)$$

Then irradiance may be written as,

$$I = E * E = 4E_0^2\, cos^2\left(\frac{\phi}{2}\right) \qquad (5)$$

Equation 5 shows that the intensity will be maximum, or constructive interference will occur when ϕ=2mπ, and destructive interference will occur when ϕ = (2m+1) π for any integer m and zero. In this way, the intensity pattern i.e. bright or dark pattern depends upon the phase difference between the waves interfering with each other. Since, a path difference of ‘λ’ corresponds to the phase difference of 2π rad for constructive interference; equation 5 can also be written in the form of a path difference (δ) between two waves. The path difference δ is related to phase difference by

$$\phi = \frac{2\pi}{\lambda}\, \delta \qquad (6)$$

In order to observe a high quality interference fringe pattern between the two beams, several conditions must be met.[1] First the phase difference between the two light beams should not exceed the coherence length, which will be discussed in detail later. Secondly, the polarization properties of two light waves must match with each other and thirdly the relative intensities of the two beams should be close to each other.

## 2.3 Spatial Heterodyne Raman Spectrometer

### 2.3.1 General Overview

The spatial heterodyne Raman spectrometer (SHRS) is a type of Fourier Transform spectrometer, first described by Gomer et al.,[5] for visible Raman measurements, and extended into the deep UV by Lamsal et al.[6,7] The goal was to develop a small, lightweight and high throughput spectrometer with no moving parts that offered the resolving power required for high resolution UV Raman measurements, and overcome issues in conventional grating based UV spectrometers, which tend to be rather large and bulky with low throughput. The SHRS follows the design of the basic spatial heterodyne spectrometer (SHS) as described by John Harlander.[8,9] The basic design of the SHS is similar to a Michelson interferometer but with tilted diffraction gratings instead of moving mirrors. There are no moving parts, and like a Michelson interferometer, there is no entrance slit. The small footprint, large input aperture, and lack of moving parts makes the SHRS ideal for space applications. The SHRS design also offers other advantages, including high spectral resolution, equal to the resolving power of the combined diffraction gratings, very high optical etendue, high resolution in the UV and the ability to do 2D imaging. The SHS has been utilized for applications like atmospheric sensing,[9,10] flame absorption spectroscopy,[11] and infrared spectroscopy.[12] The SHS boasts a wide acceptance angle at the gratings, from 1° or 10° using field widening prisms,[10] and thus a wide-area measurement capability. SHRS is also compatible with a pulsed laser and gated detector and the measurement can be performed in ambient light conditions. The use of pulsed laser also helps to “freeze out” vibrational instabilities in the SHRS.

The high resolution and high throughput offered by the SHRS design is ideal for deep-UV Raman spectroscopy where the Raman spectrum covers a very small wavelength range, thus requiring a high-resolution spectrometer to resolve the Raman bands. Because of the large acceptance angle, the SHRS allows the use of large laser spots on the sample. This gives lower laser irradiance and minimizes laser-induced damage caused by focusing a laser onto the sample; consequently, samples can be illuminated using relatively high laser power. It is also worth noting that the SHRS has only a weak coupling of resolution and throughput, and as a result, a high-resolution SHRS instrument can be built in a very small package, useful for space applications where the instrument size is a concerned.

### 2.3.2 Spatial Heterodyne Raman Spectrometer Working Principle

The SHRS follows the design of the basic spatial heterodyne interferometer as described by Harlander,[8] modified for Raman applications by the inclusion of holographic laser line rejection filters (Figure 2.1). Despite the modifications, the SHRS maintains the advantages of a Fourier Transform interferometer including high light throughput (as there is no input slit), small size, larger field of view and the multiplex advantage. The use of stationary diffraction gratings makes the SHRS design free from any moving parts, a distinct advantage over the Michelson interferometer where a mirror has to be continuously moved during measurements.

During SHRS measurements, the scattered Raman light is collected, collimated and passed through the entrance aperture and divided into two coherent beams by a 50/50 fused silica beamsplitter. The two beams are then diffracted by the tilted diffraction gratings back towards the beamsplitter, where they recombine. The SHRS operates in the Littrow configuration, that is, the gratings are tilted to a specific angle at which a wavelength of interest retro-reflects, i.e., the angle of incidence will be equal to the angle of diffraction, producing a zero optical path difference between the beams and producing no interference pattern. (Figure 2.2, left). This wavelength of interest is known as the Littrow wavelength, and grating angle is known as the Littrow angle, which can be calculated using grating equation,

$$n\,\lambda = d(sin\alpha + sin\beta) \qquad (7)$$

where n is the order, λ is the desired wavelength, m is grating groove density, α is the angle of incidence and β is the angle of diffraction. The Littrow angle for specific wavelength λ, will be

$$\Theta_L = sin^{-1}\left(\frac{\lambda}{2d}\right) \qquad (8)$$

All wavelengths other than the Littrow wavelength will diffract at a slightly different angle and will cross each other when combining at the beamsplitter thus producing an interference pattern (Figure 2.2 right). Since, the extent of diffraction (or crossing angle between two wavefronts) is directly related to the wavelength of light, for each wavelength, a unique fringe pattern is formed. The frequency of the fringe pattern is given by,[8–10]

$$f = 4\,(\sigma - \sigma_L)\,\tan\theta_L \qquad (9)$$

Where f is in fringes/cm, $\sigma_L$ is the Littrow wavenumber, $\sigma$ is a wavenumber other than the Littrow wavenumber and $\Theta_L$ is the Littrow angle. Since, the Littrow angle and Littrow wavenumber are fixed, any change in input wavenumber will change the fringe spacing in such a way that bands close to Littrow band will produce wide less frequent fringes, while bands further from Littrow will have thinner, more frequent fringes. The resultant fringe pattern is imaged onto the two dimensional array detector, typically a CCD or ICCD camera,[8-10] with the fringe modulation intensity varying along the horizontal axis of the detector, which also corresponds to the dispersion plane of the gratings. The intensity distribution of the fringe pattern *I(x)*, for a complex spectrum as a function of detector position, *x*, along the dispersion plane of the grating is given by,[8–10]

$$I(x) = \int_0^\infty B(\sigma)[1 + \cos\{8\pi(\sigma - \sigma_L)\, x \tan\theta_L\}]\, d\sigma \qquad (10)$$

where B ($\sigma$) is the input spectral intensity at wave number $\sigma$. The Fourier transform of *I(x)* recovers the power spectrum. Figure 2.2 illustrates the process with a fringe image, the image cross section and the corresponding power spectrum obtained by applying a one dimensional Fourier transform to the cross section. The measurement is accomplished without mechanically scanning or moving any parts of the system. Also, as the Littrow position can be tuned to any wavenumber by tilting the gratings, the measurements can be performed at any wavelength.

It is to be noted that light does not propagate as a perfect sinusoidal wavefront but rather in bundles of wavefronts where the individual wavefronts of light are in phase with each other only for a specified interval of length, known as the coherence length. The optimum interference pattern can only be obtained from the superposition of light beams propagating in phase (i.e., from coherent source). The coherence length of light is a function of the bandwidth of the light,[13] which is given by,

$$l = \frac{c}{\Delta\nu} = \frac{\lambda^2}{\Delta\lambda} \tag{11}$$

where $l$ is the coherence length, c is the speed of light, $\Delta\nu$ and $\Delta\lambda$ are the spectral width in terms of frequency and wavelength respectively. As Eq. 11 shows, monochromatic sources like lasers have very long coherence lengths, for example, a 632 nm He-Ne laser with bandwidth 1GHz has a coherence length of 30 cm. Raman bands are typically broad with very short coherence lengths, in the range of micrometers. In the SHRS, the path length of each arm of the SHRS is adjusted to match within the coherence length of the Raman band. When adjusting the Littrow wavelength, the rotational angle of the gratings must be matched to the a few hundredths of a degree. A mismatch in the arm lengths can lead to interferogram fringe distortion and reduction in fringe visibility resulting in retrieval error and increased noise in the spectrum. The optical path difference between the two arms can be precisely matched by measuring the white light fringe image, as white light has extremely short coherence length[14] (i.e., in an order of a few microns).

### 2.3.3 Optical Throughput of the SHRS

The sensitivity of any spectrometer is related to the light throughput. One measure of light throughput in an optical system is etendue[15] (E), defined as $E=\Omega A_l$, where $\Omega$ is the collection solid angle of the optical system and $A_l$ is the area of the limiting aperture of the collection system. The etendue provides a good comparison of system sensitivity, since it describes the maximum collection and throughput of an optical system. In dispersive spectrometers, the entrance slit often limits the system etendue because of the entrance slit being smaller than the image of the excited region of the sample. For a dispersive spectrometer, the entrance aperture slit size can range from 10-300 microns wide. Utilizing the SHRS with a 1-inch aperture would give it a throughput advantage $10^4$ times greater than a dispersive system with a 10-micron entrance slit. (Calculations shown below). An f/4 monochromator (very fast for a UV system) with a 10-micron entrance slit has an optical etendue of ~$4.8\text{x}10^{-5}$ sr $\text{cm}^2$. The basic SHRS design provides a much larger etendue, where the limiting aperture is the diffraction grating and Ω is defined by the resolution. Of the system as $\Omega_{max} = 2\pi/R$. In the case of the SHRS system described below with R=7500, $\Omega_{max}$ =~8 $\text{x}10^{-4}$ sr, and E =~$5\text{x}10^{-3}$ sr $\text{cm}^2$, about two orders of magnitude larger than the monochromator.

### 2.3.4 Spectral Resolution and Bandpass

The spectral resolution of the SHRS does not depend on a slit and is not a strong function of spectrometer size. At a given wavenumber the resolving power, R, is determined by the total number of grooves illuminated on the two gratings. For the SHRS incorporating gratings of size *W* mm with *d* grooves per millimeter,[16]

$$R = 2\,W\,d = \frac{\lambda}{\Delta\lambda} = \frac{\sigma}{\Delta\sigma} \qquad (12)$$

In equation 12, λ is the center wavelength (or wavenumber) and Δλ, or, Δσ is the smallest resolvable wavelength difference that can be measured by the spectrometer. For the SHRS instruments, the resolving power is the same as a diffraction limited dispersion monochromator with equivalent gratings and an infinitely small slit[8] i.e., equal to the total number of grooves illuminated on the diffraction grating—physically impossible using a conventional dispersive-grating Raman spectrometer. Thus, small gratings can be used in the SHRS and still give high spectral resolution. For example, a 50-mm diffraction grating with 600 grooves per mm will produce a resolving power of 30,000 when used in first order, providing spectral resolution of ~1 $cm^{-1}$ using a 266 nm excitation laser. This is much higher than is required for most Raman measurements and demonstrates one of the key design issues. A moderate resolving power of ~7500 is sufficient to provide spectral resolution (~ 5 $cm^{-1}$) over a wide spectral range.

The theoretical maximum band pass of the SHRS is determined by the resolving power, $R$, and the number of pixels, $N$, in the horizontal direction (i.e., x-axis) on the detector. The Nyquist limit sets the highest frequency that can be measured by the detector to the frequency that produces N/2 fringes.[8] For wavelength ($\lambda$), the maximum band pass of the SHRS can be written as:

$$R = \frac{N\,\lambda}{2\,R} \tag{13}$$

For samples related to planetary exploration, a spectral range for a typical Raman measurement is about 300-3500 $cm^{-1}$. Using a 244 nm laser, this corresponds to a wavelength range of ~246 to ~267 nm, for a band pass of ~21 nm. For the measurements that require a larger spectral range, the bandpass can be extended by using the detector with more horizontal pixels or by reducing the resolution of the system.

### 2.3.5 The Significance of Spatial Heterodyne Raman Spectroscopy in Planetary Applications

It is generally accepted that Raman spectroscopy is useful for planetary missions. NASA has already selected a Raman spectrometer as one of the major instruments for its upcoming Mars lander mission, Mars 2020[17,18] that is proposed to be launched in 2020. Two Raman spectrometers are being developed for this mission, a visible and a UV spectrometer. UV Raman provides much higher sensitivity than infrared or visible Raman because of the $1/\lambda^4$ dependence of Raman scattering[19] (e.g., ~100 times higher signal using 266 nm versus 785 nm excitation), the possibility of resonance Raman enhancement[20,21] for highly absorbing molecules, and the relative absence of fluorescence[22] in this wavelength region. However, existing UV Raman spectrometers do not meet the following necessary criteria to be considered for planetary missions: high spectral resolution (5 $cm^{-1}$ or better), large spectral band pass (250-3500 $cm^{-1}$), high sensitivity, small size and low weight. Dispersive, diffraction grating based, UV Raman systems are inherently large in order to provide the required spectral resolution, and have a very low light throughput because of the resolution requirement of small slit widths.

A typical commercial UV spectrometer for Raman applications (e.g., Acton Model, F/6.7) provides 6.5 $cm^{-1}$ spectral resolution with a 266 nm laser. The dimensions are 76x30x20 $cm^3$ and it weighs ~21 kg (46 lbs), without the detector or input optics. The size of such an instrument is inherent in the design of any dispersive diffraction grating system because of the requirements of long focal length optics and large gratings to achieve high spectral resolution. Existing non-dispersive UV Raman systems have very poor spectral resolution (e.g., tunable filter, FT Raman, Hadamard, coded-aperture, etc.) or are not compatible with pulsed laser excitation and gated detection. Pulsed excitation and gated detection have been shown to be essential for daylight Raman measurements.[23].

### 2.3.6 The SHRS Design Considerations

The typical spatial heterodyne Raman spectrometer is comprised of the following major components: collection and filtering optics, two diffraction gratings, a beamsplitter, imaging or relay optics and a two-dimensional photo detector. The success of the SHRS operation depends on the careful selection of each of these components.

One of the limitations of interferometer-based spectrometers, including the SHRS, is the multiplex noise, which comes from signals outside the pass band of interest[24] and must be controlled properly. Therefore, filtering unwanted light is an essential part of SHRS measurements. For Raman measurements, potential sources of multiplex noises are scattered laser light, fluorescence, unresolved Raman bands, stray light and grating order overlap. These sources contribute in background noise, and can also reduce the contrast of the interference pattern. Laser scattering can be easily controlled using commercially available Raman edge filters or holographic notch filters. Short pass or bandpass filters are employed to restrict longer wavelength fluorescence. Band pass filters with a spectral window in the desire spectral range should be used to eliminate unresolved bands or any bands out of the spectrometer spectral range.

The beamsplitter is another critical component of SHRS. It is the heart of the interferometer, and any optical losses in it can result into the poor sensitivity. The ability of the beamsplitter to transmit and reflect the input light intensity is functionalized by its efficiency ($\eta$),[25]

$$\eta = 4R_\lambda T_\lambda \qquad (14)$$

where, T and R are the transmission and reflectance coefficient of the beamsplitter at wavelength $\lambda$. Equation (14) infers that $\eta = 1$ only when, $T_\lambda = R_\lambda = 0.5$. Any losses or uneven ratio of transmission and reflectance decreases the efficiency of the beamsplitter. Additionally, any deviation in optical qualities like surface flatness, material homogeneity and the presence of defects may distort the transmitted wavefront. Therefore, it is essential to use a beamsplitter with higher efficiency, good surface flatness and fewer surface defects in order to observe a high quality interferogram. Beamsplitters can typically be found as plates or as cubes. For visible applications, cube beamsplitters are preferred because they are easy to align and are cost effective. But it is rather difficult to find a cube beamsplitter for deep UV because the cement used for binding the prisms tends to absorb UV light strongly. In this context, the plate beamsplitter seems to be a good option for UV Raman.

The selection of diffraction gratings is also very important. The gratings disperse the light. The extent of dispersion controls the resolving power, which in turn affect the bandpass of the system. The gratings with higher groove density yield greater resolving power, but that will also reduce the bandpass of the system, therefore, it is required to select the gratings wisely to achieve the best compromise between the resolution and usable bandpass. Ideal deep UV Raman applications require a resolution 5 cm$^{-1}$ and a bandpass of 3500 cm$^{-1}$. Apart from bandpass and resolution, it is also necessary to block higher diffraction order from reaching the detector, which may significantly increase the noise of the system. The gratings and beam splitters must be separated at least by a distance that will prevent 0-order and 2nd-order diffraction from the grating from entering the beam splitter For example, for an SHRS with 25.4 mm 150 gr/mm gratings the required minimum separation is about 300 mm for Raman measurements with 532 nm excitation laser.

The physical properties of the gratings, primarily surface properties, plays a significant role in the performance of the gratings. Defects such as dust, scratches, pinholes and unevenness in the gratings lead to unwanted scattering, resulting into higher background. In addition, irregularities in groove spacing and unevenness in the depth of the grooves leads to wavefront distortions resulting in poor fringe contrast. Holographic gratings have fewer aberrations than ruled reflection gratings, but holographic gratings are not usually made with coarse groove spacings. Therefore, while a holographic grating is the best choice for higher resolution measurements, for measurements that require a large bandpass, ruled gratings are typically the best available option.

Another important component of the SHRS is imaging lenses or relay optics, which transfer the fringe image onto the detector. Since the overlap of diffracted wavefronts occurs virtually in front of each of the gratings, an optic or set of optics is required to precisely image this plane onto the detector. High quality single or multi-component lens systems are required to eliminate any optical aberrations and to preserve the integrity of the interferogram. It is important to note that the lenses have inherent limitations to spatial resolution of the formed image. The ability of a lens to transfer information from object to image is defined in terms of the modulation transfer function (MTF), which will be described in detail in chapter 7. Bands with larger wavenumber shifts produce more closely spaced fringes. It is critical to use the lenses with the highest MTF to maintain high and presence of high frequency information in the interferogram

While the spectral resolution is determined by the gratings, the spectral range is determined by the number of pixels on the CCD or ICCD camera in the SHRS instrument. A large format CCD camera is needed to build SHRS instruments with high-resolution and broad spectral coverage. Scientific grade large format CCD cameras such as 2048 × 2048 formats are commercially available. The performance of the CCD camera depends on quantum efficiency, thermal noise and readout noise. In a thermoelectrically cooled CCD, thermal noise is very low, and the CCD can be built with unichrome coating for enhanced UV performance to allow for higher quantum efficiency in the UV region. For field-based measurements, an ICCD detector is ideal, which along with a pulsed laser helps to avoid ambient light background, and allows so an entire Raman spectrum to be acquired with each laser pulse. The pulsed laser can also “freeze out” vibrational instabilities in the SHRS.

## 2.4 References

1. P. Hariharan. Basics of interferometry. 2nd ed. Elsevier Academic Press, Amsterdam, Boston, 2007.

2. A.A. Michelson, E.W. Morley. "On the relative motion of the Earth and the luminiferous ether". Am. J. Sci. 1887.3-34(203): 333–345.

3. T. Hirschfeld, B. Chase. "FT-Raman spectroscopy: development and justification". Appl. Spectrosc. 1986. 40(2): 133–137.

4. F.L. Roesler. "Fabry-Perot Instruments for Astronomy". Methods in Experimental Physics. Elsevier, 1974. Pp. 531–569.

5. N.R. Gomer, C.M. Gordon, P. Lucey, S.K. Sharma, J.C. Carter, S.M. Angel. "Raman Spectroscopy Using a Spatial Heterodyne Spectrometer: Proof of Concept". Appl. Spectrosc. 2011. 65(8): 849–857.

6. N. Lamsal, S.M. Angel, S.K. Sharma, T.E. Acosta. Visible and UV Standoff Raman Measurements in Ambient Light Conditions Using a Gated Spatial Heterodyne Raman Spectrometer. Lunar and Planetary Science Conference. 2015. P. 1459.

7. N. Lamsal, S.M. Angel. "Deep-Ultraviolet Raman Measurements Using a Spatial Heterodyne Raman Spectrometer (SHRS)". Appl. Spectrosc. 2015. 69(5): 525-534.

8. J.M. Harlander. "Spatial Heterodyne Spectroscopy: Interferometric Performance at any Wavelength Without Scanning." PhD Thesis. 1991. 62.

9. J. Harlander, R. Reynolds, F. Roesler. "Spatial Heterodyne Spectroscopy for the Exploration of Diffuse Interstellar Emission-Lines at Far-Ultraviolet Wavelengths". Astrophys. J. 1992. 396(2): 730–740.

10. J.M. Harlander, F.L. Roesler, C.R. Englert, J.G. Cardon, R.R. Conway, C.M. Brown, "Robust monolithic ultraviolet interferometer for the SHIMMER instrument on STPSat-1". Appl. Opt. 2003. 42(15): 2829.

11. R.J. Bartula, J.B. Ghandhi, S.T. Sanders, E.J. Mierkiewicz, F.L. Roesler, J.M. Harlander. "OH absorption spectroscopy in a flame using spatial heterodyne spectroscopy". Appl. Opt. 2007. 46(36): 8635.

12. C. Englert. "Long-wave IR sensing using spatial heterodyne spectroscopy". SPIE Newsroom. 2009.

13. S.K. Saha. Aperture Synthesis: Methods and Applications to Optical Astronomy. Springer New York, NY, 2011.

14. A. Donges. “The coherence length of black-body radiation”. Eur. J. Phys. 1998. 19(3): 245.

15. J.D. Ingle, S.R. Crouch. Spectrochemical analysis. Prentice Hall, Englewood Cliffs, N.J, 1988.

16. W. Harris, F. Roesler, L. Ben-Jaffel, E. Mierkiewicz, J. Corliss, R. Oliversen, et al. “Applications of spatial heterodyne spectroscopy for remote sensing of diffuse UV–vis emission line sources in the solar system”. J. Electron Spectrosc. Relat. Phenom. 2005. 144-147: 973–977.

17. A. Burton, S. Clegg, P.G. Conrad, K. Edgett, B. Ehlmann, F. Langenhorst, et al. “SHERLOC: Scanning Habitable Environments With Raman & Luminescence for Organics & Chemicals, an”. n.d.

18. “SHERLOC-2020MissionPlans”.http://mars.nasa.gov/mars2020/mission/science/for-scientists/instruments/sherloc/

19. R.L. McCreery. Raman spectroscopy for chemical analysis. John Wiley & Sons, New York, 2000.

20. S.A. Asher. “UV resonance Raman spectroscopy for analytical, physical, and biophysical chemistry. Part 1”. Anal. Chem. 1993. 65(2): 59A–66A.

21. M. Ghosh, L. Wang, S.A. Asher. “Deep-Ultraviolet Resonance Raman Excitation Profiles of NH4NO3, PETN, TNT, HMX, and RDX”. Appl. Spectrosc. 2012. 66(9): 1013–1021.

22. S.A. Asher, C.R. Johnson. “Raman Spectroscopy of a Coal Liquid Shows that Fluorescence Interference is Minimized with Ultraviolet Excitation”. Science. 1984. 225(4659): 311–313.

23. J.C. Carter, S.M. Angel, M. Lawrence-Snyder, J. Scaffidi, R.E. Whipple, J.G. Reynolds. “Standoff Detection of High Explosive Materials at 50 Meters in Ambient Light Conditions Using a Small Raman Instrument”. Appl. Spectrosc. 2005. 59(6): 769–775.

24. D.B. Chase. “Fourier transform Raman spectroscopy”. J. Am. Chem. Soc. 1986. 108 (24): 7485–7488.

25. P.R. Griffiths, J.A. de Haseth. Fourier Transform Infrared Spectrometry. John Wiley & Sons, Inc., Hoboken, NJ, USA, 2007.

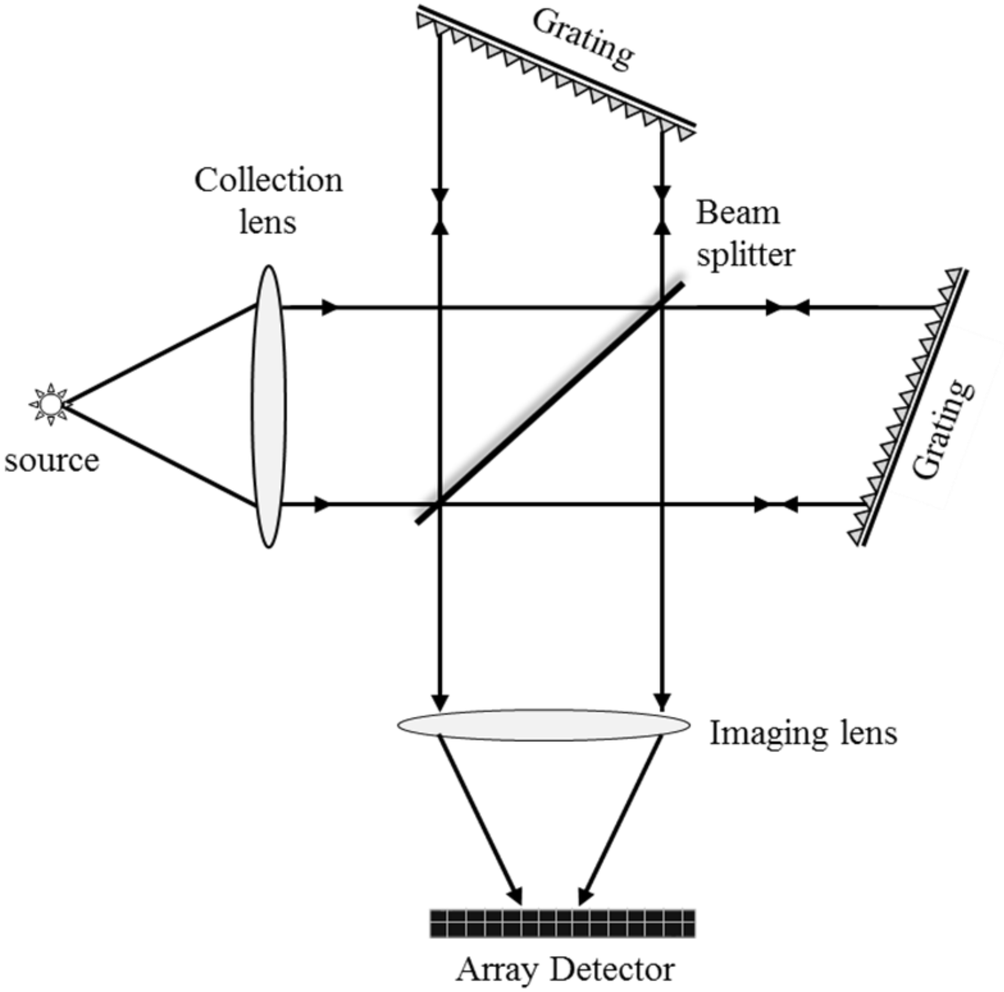

Figure 2.1. Optical layout of a spatial heterodyne Raman spectrometer.

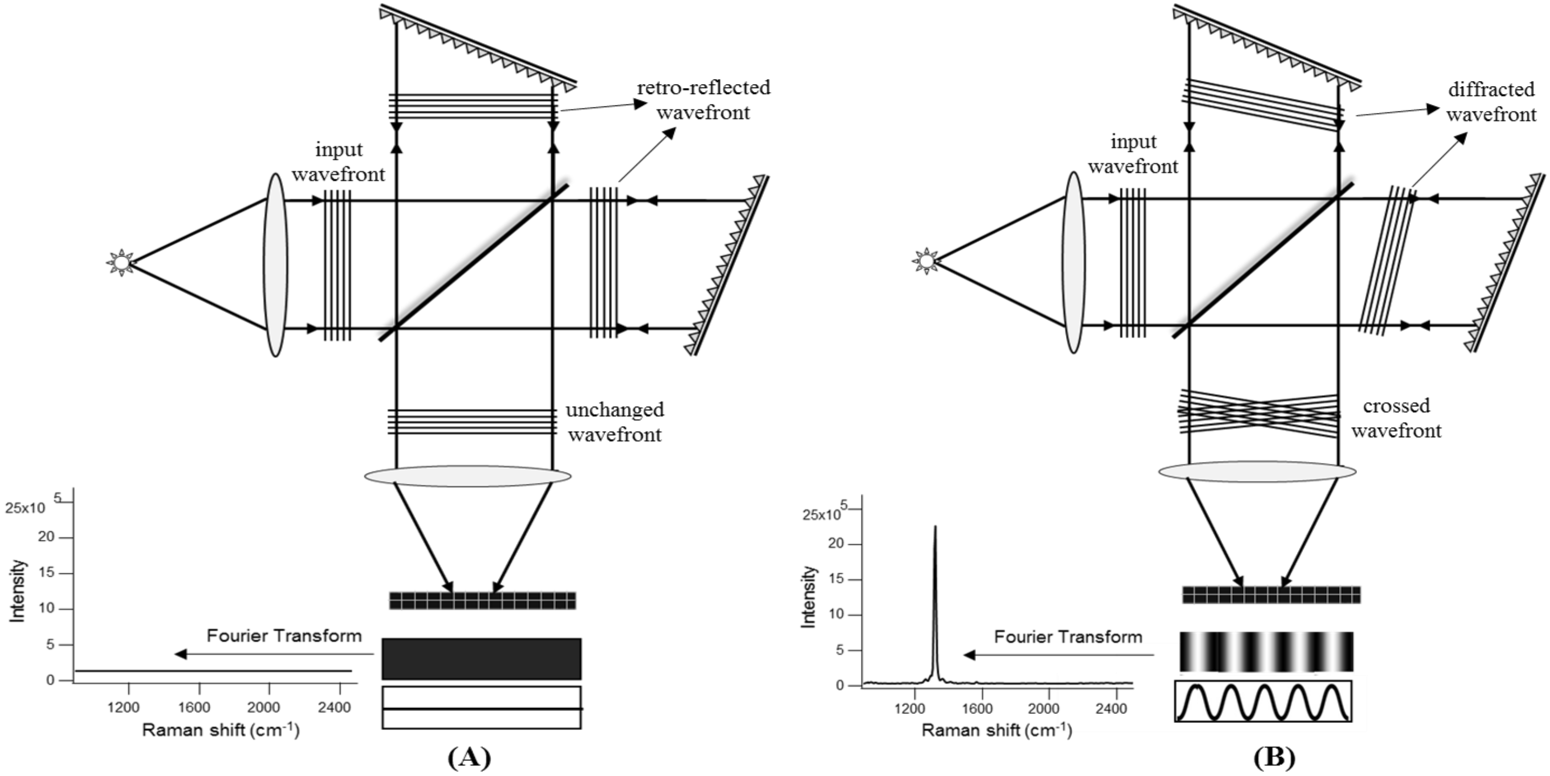

Figure 2.2. Optical layout that shows the working principle of SHRS. For specific wavelength, λ, figure on top (A) corresponds to Littrow configuration in which angle of incidence will be equal to angle of diffraction and no interference pattern is formed. But for any wavelength other than λ, figure on bottom (B) diffraction occurs and crossed wavefront is formed resulting into interference pattern which on Fourier transformation gives intensity spectrum

# Chapter 3

## Deep-UV Raman Measurements Using a Spatial Heterodyne Raman Spectrometer (SHRS)[A]

### 3.1 Abstract

A deep-UV, 244-nm excitation, spatial heterodyne Raman spectrometer (SHRS) is demonstrated for the first time. The deep-UV SHRS has no moving parts and though it is small for a deep-UV Raman spectrometer the spectral resolution is shown to be about 4 cm$^{-1}$. The deep-UV SHRS also has a large input aperture and acceptance angle, and the resulting large field of view is shown to be useful to avoid laser-induced sample degradation. In this feasibility study, Raman spectra of several compounds are measured to demonstrate the spectral resolution and range of the system. A photosensitive compound is also measured to demonstrate the ability of using a large laser spot to minimize UV laser-induced sample degradation.

---

[A] The final, definitive version of this paper has been published in Applied Spectroscopy, Vol. 69, Issue 5, May 2014 by SAGE Publications Ltd, All rights reserved. © [Nirmal Lamsal, S. Micheal Angel)]. The online version of this article can be found at http://asp.sagepub.com/content/69/5/525.short.

### 3.2 Introduction

One of the motivations for developing a UV SHRS is for planetary exploration using a lander or rover. There is a need for smaller more powerful instruments for geochemical measurements, and to measure biomarkers, both organic and inorganic, in

research for past or present life on other planets.[1] Raman spectroscopy is ideally suited for planetary exploration because Raman spectra provide detailed structural information for both organic and inorganic samples, including crystallinity, polymorphism, solvates, phase and intrinsic stress/strain for mineralogical analysis.[2–7] The advantage of the SHRS for planetary exploration is that it is small, robust and can be used for deep-UV, UV or visible Raman measurements.

Although a highly versatile technique, Raman spectroscopy has inherent limitations. Raman scattering is an extremely weak phenomenon, and the fluorescence background from sample impurities can mask the Raman signal completely. Both of these difficulties can be addressed by moving the excitation wavelength to the deep-UV. Deep-UV excitation can yield larger Raman signals because the Raman scattering cross section increases exponentially at shorter wavelengths[8] proportional to $1/\lambda^4$. Also, in the deep-UV the Raman spectrum occurs at much shorter wavelengths, in a spectral region that is free from longer wavelength fluorescence.[9,10] Additionally, there is a possibility of resonance enhancement at UV wavelengths that can result in several orders of magnitude enhancement in Raman signals.[11] Utilizing UV excitation for Raman is rather challenging. It requires a high-resolution spectrometer, thus low light throughput, to discern the Raman signal that occurs over a very narrow wavelength or spectral range. Moreover, there is a high risk of UV laser induced photo or thermal degradation of the sample, which is usually minimized by moving or spinning the sample in the laser beam. Spectrometers that provide sufficiently high spectral resolution for deep-UV Raman typically are large and have very low light throughput because of the need for large, high dispersion gratings, long focal length optics, and narrow slits.

In the context of a small UV Raman spectrometer for planetary exploration, the SHRS design looks very promising. The SHRS is small, lightweight and compact with no moving parts, properties important for an instrument that will be flown in space. The SHRS can provide high-resolution spectra (5 $cm^{-1}$ or better using deep-UV excitation) with a spectral band pass >2450 $cm^{-1}$. In addition, the SHRS has a large entrance aperture with a large acceptance angle, i.e. high light throughput. Furthermore, the SHRS is compatible with pulsed laser excitation and gated detection, an essential feature for standoff measurements in ambient light conditions. All these characteristics together make the SHRS potentially suitable for planetary exploration.

In an earlier proof-of principle study, the Raman spectra of several solid and liquid samples were measured with a SHRS using 532 nm excitation[12]. In this work, we present the first use of the SHRS to perform deep-UV Raman measurements using 244 nm excitation. Example Raman spectra are shown with a discussion of the performance of the SHRS, namely the spectral resolution, system bandpass, the ability to conduct wide area measurements and fluorescence rejection.

## 3.3 Experimental

The UV spatial heterodyne Raman spectrometer is shown schematically in Fig. 1. The basic design of the SHRS is similar to one described earlier[12]. The SHRS interferometer consists of a pair of 300 grooves/mm 25 mm square reflective diffraction gratings blazed for 300 nm wavelength, and a 20 mm fused silica quartz beamsplitter. The gratings were mounted in piezo motor driven optical mounts (Newport, AG-UC8 model) with a piezo motor controller and positioned on a precision rotation stepper (Newport, URS75BPP model) for setting the angle precisely to the desired Littrow wavelength. Images of the diffraction gratings were imaged onto a thermo-electrically-cooled back-illuminated UV-enhanced CCD detector with 2048×512, 13.5 micron pixels (PIXIS-2048 2KBUV, Princeton Instruments) using a 105 mm focal length**,** f/4.5 fused silica lens (JENOPTIK CoastalOpt® 105 mm UV-Vis SLR lens). The imaging lens (IL in Fig. 1) was placed approximately 245 mm (~2.33 focal length, m ~0.75) from the gratings and ~185 mm from the detector to form a 15 mm square interferogram image on the 7 mm high CCD.

A 244-nm, intracavity frequency-doubled Ar-ion laser (Lexel, 95 SHG model) was used as the excitation source for all spectra shown. The UV laser power varied from 5 to 13 mW at the sample. The laser beam was directed onto the sample using $45^o$ dielectric laser line mirrors (M in Fig. 1), with >98% reflectivity over a 244-257 nm range, to clean up the 244 nm line from the 488 nm fundamental wavelength. The laser was focused onto the sample using a 75 mm focal length quartz lens (not shown in Fig. 1), mounted on a translational microstage to allow changing the size of the laser spot on the sample. Liquid samples were placed in a 1-cm quartz cuvette, centered on the focus of both the collection lens and the laser focus. Solid samples, either ground and packed in quartz cuvettes or pressed into pellets, were illuminated in the same way, but were mounted on an x-y stage for front-surface illumination. Scattered light from the sample was collected using either a 50 mm or 75 mm focal length quartz lens, with the laser incident on the sample at $150^o$ with respect to the optical axis of the collection lens. Collimated light was guided into the interferometer by two high performance dielectric mirrors placed in a $90^0$ arrangement (not shown in Fig. 1). These mirrors have reflectivity over 95% in the wavelength range 244-266 nm, which is equivalent to a Raman range of 0-3400 cm$^{-1}$ using 244 nm excitation. The diameter of the SHRS entrance aperture was 20 mm, to match the size of the beamsplitter. A long pass filter (Semrock, 229/244 nm stopline dual-notch filter) with OD >4 (at 244 nm) was used to block scattered laser light.

The interferometer Littrow wavelength (i.e., grating angles) was set using either the laser line, narrow lines from a low-pressure mercury lamp, or a narrow Raman line. CCD fringe images were measured using Princeton Instruments Light Field software provided with the detector. Apart from the fringe image, three other images were acquired for each spectrum; two by blocking each of the gratings separately and one by blocking both gratings simultaneously. These additional images were sometimes used for background corrections of the fringe images. Fourier transforms of the fringe images were performed using the fast Fourier transform (FFT) function in Matlab. Each spectrum was apodized using a Hamming function to reduce ringing effects in the spectral baseline. The Raman spectra were calibrated by locating the position of known Raman bands and using a polynomial fit.

For this feasibility study, no flat field or instrument efficiency corrections, smoothing, sharpening, or any other post-processing was used for any of the data presented in this paper. For this reason some of the spectra shown show artifacts that are caused by such things as pixel-to-pixel variations in the CCD, optical imaging aberrations, and wavefront distortions caused by imperfections in the optics such as poor surface flatness in the beam splitter, the presence of grating scratches and irregularities, and other irregularities in the optics. Post image processing and phase corrections in the SHRS images are essential to eliminate spectral artifacts and improve signal to noise ratio. This is the subject of a future study. Exposure times for all spectra are shown in the figure captions but were typically 60 seconds.

### 3.4 Results and Discussions

The basic design of the spatial heterodyne Raman spectrometer is similar to the previously described setup.[13–17] In the interferometer (Fig. 2), light from the sample is collimated and passed through a 50/50 quartz beam splitter, which divides the beam into two parts which are directed onto tilted diffraction gratings. Light diffracted from the gratings recombines at the beamsplitter as crossing wave fronts, generating an interference pattern as shown in Fig. 2. The interference pattern is imaged onto the CCD to produce a fringe image. A Fourier transform of the fringe image provides the intensity spectrum[13,14]. For a specific grating tilt angle, '$\theta_L$', there is one wavelength, known as the Littrow wavelength, for which the crossing angle is zero and no interference pattern is produced. For any wavelength other then Littrow, the crossed wave fronts generate a fringe pattern that is imaged onto the detector. The number of fringes produced is given by:

$$f = 4\,(\sigma - \sigma_L)\,\tan\theta_L \qquad (1)$$

where $f$ is fringes/cm, $\sigma$ is the wave number of the Raman band of interest, $\sigma_L$ is Littrow in wavenumbers, and $\theta_L$ is the Littrow angle.[13,14] The intensity of resultant fringes obtained as a function of position, $x$, is given by:

$$I(x) = \int_0^{\infty} B(\sigma)[1 + \cos\{8\pi(\sigma - \sigma_L)\,x \tan\theta_L\}]\,d\sigma \qquad (2)$$

where $B(\sigma)$ is the input spectral intensity at wave number $\sigma$, $x$ is the position on the detector, and the Fourier transform of $I(x)$ yields the Raman spectrum[13–16].

### 3.4.1 Spectral Resolution of the Deep-UV SHRS

For the SHRS incorporating gratings of size $W$ mm with $d$ grooves per millimeter, the resolving power (R) is equal to the total number of grooves illuminated on both gratings, expressed as:

$$R = 2Wd \qquad (3)$$

where resolving power is defined in equation 4.

$$R = \lambda/\Delta\lambda = \sigma/\Delta\sigma \qquad (4)$$

In equation 4, λ is the center wavelength (or wavenumber) and Δλ, or Δσ, is the smallest resolvable wavelength difference that can be measured by the spectrometer. The theoretical resolving power of the SHRS using 300 grooves/mm 25 mm diffraction gratings and a 20 mm beamsplitter is 12,000, where the number of grooves illuminated is limited by the 20 mm beam splitter. Based on equation 3, the theoretical spectral resolution for the SHRS is 3.4 cm$^{-1}$ (40,984 cm$^{-1}$/12,000) or 0.02 nm at 244 nm, the laser excitation wavelength.

In order to estimate the actual resolution of the SHRS in the UV, we measured the Raman spectrum of an industrial grade diamond crystal using 244 nm excitation. Diamond was selected as a resolution standard because it has a very sharp band at 1332 cm$^{-1}$ (C-C stretch), the FWHM of which is reported as 1.2 cm$^{-1}$.[18] Figure 3 shows the UV Raman spectrum of diamond that was recorded using the SHRS with the Littrow wavelength set to 1300 cm$^{-1}$. Note: the feature that looks like a cutoff band around 1300 cm$^{-1}$ is an artifact caused by laser light that is not completely blocked by the laser rejection filter. Similar features are seen in Figures 5, 7 and 8. The top inset in Fig. 3 (FI) shows the diamond interferogram fringe image. The two bright side lobes in the image are caused by grating order overlap from higher order diffracted light striking the detector, resulting in poor interferogram fringe visibility and increased background. This type of background contribution can be eliminated by careful placement of the interferometer optical components and by the use of spatial filters. Background issues in the SHRS are the topic of a future paper. The middle inset in Fig. 3 (I) shows the intensity cross section of the CCD interferogram fringe image, where the intensities in each column of CCD pixels are summed. In the spectrum the full width half-maximum (FWHM) of the 1332 cm$^{-1}$ band is ~4.2 cm$^{-1}$, only a wavenumber larger than the theoretical resolution of 3.4 cm$^{-1}$. The spectrum is shown without apodization, background correction or post processing of any kind in order to minimize spectral broadening. The small discrepancy in spectral resolution could be due to imperfect focusing of the CCD imaging lens or imprecise alignment of the gratings. For the other Raman measurements, the interferogram is apodized and background corrections are performed to improve the SNR.

Figure 4 shows the SHRS-Raman spectra of three solid compounds; Teflon (a), potassium perchlorate, $KClO_4$, (b) and calcite (c), acquired using 244 nm laser excitation and 5 mW of laser power. The arrows above each spectrum refer to the appropriate intensity axis for that spectrum. There was no evidence of laser induced sample damage for any of these samples so the laser was focused to a small spot on the sample. In the Teflon spectrum (a), the prominent band at 734 cm$^{-1}$, with a FWHM of about 16 cm$^{-1}$, is due to a symmetric F-C-F stretching vibration.[18,19] The three closely spaced bands in the 1200 to 1400 cm$^{-1}$ region are due to an anti-symmetric F-C-F vibrational mode at 1215 cm$^{-1}$, and C-C vibrational modes at 1296 and 1378 cm$^{-1}$. Although no attempt was made to correct the intensity of these bands for the instrument response, the relative intensities and band widths of these Raman bands look qualitatively like published UV Raman spectra of these compounds[20–22]. The SHRS Raman spectrum of $KClO_4$ (b) exhibits bands in the 629-1125 $cm^{-1}$ region. The strong Raman band at 942 $cm^{-1}$ with a FWHM of ~11 $cm^{-1}$, corresponds to the symmetric vibrational mode of $ClO_4^-$. The weaker band at 629 $cm^{-1}$ corresponds to the antisymmetric bending mode, and the weak bands at 1087 and 1125 $cm^{-1}$ correspond to the antisymmetric stretching mode. All of these observed features are in good agreement with previously published results.[23,24] Figure 4(c) shows the SHRS-Raman spectrum of calcite with a prominent band at 1087 $cm^{-1}$, from the symmetric stretching vibration of the $CO_3^{2-}$ ion.[25] The weak Raman features at 715, 1437, and 1749 $cm^{-1}$ are due to asymmetric stretching, symmetric deformation and combination of symmetric stretch and symmetric deformation bands, respectively.[25]

### 3.4.2 Band Pass of the SHRS

The theoretical maximum band pass of the SHRS is determined by the resolving power, $R$, and the number of pixels, $N$, in the horizontal direction (i.e., x-axis) on the detector. The Nyquist limit sets the highest frequency that can be measured by the detector to the frequency that produces N/2 fringes[14-15]. For wavenumber λ, the maximum band pass of the SHRS can be written as[15]:

$$BP = N\,\lambda/2\,R \qquad (5)$$

For the SHRS with 12,000 resolving power and with ~1536 pixels illuminated on the CCD (only 75% of the 2048 CCD pixels in the *x* direction are illuminated because of the system magnification), the maximum spectral bandpass at the laser wavelength of 244 nm (40984 $cm^{-1}$) is 15.6 nm or ~2623 $cm^{-1}$. The spectral range would be larger if all the pixels on the detector were fully illuminated. However, the grating image was reduced on the CCD from 20 mm to 15 mm so that less light would be lost on the 7 mm high detector.

Figure 5 shows the SHRS Raman spectrum of acetonitrile obtained by setting Littrow to ~700 $cm^{-1}$. The interferogram cross section is shown in the inset. The spectrum shows Raman bands from 921 $cm^{-1}$ (C-C stretching region) to 2943 $cm^{-1}$ (C-H stretching region) and the total spectral range shown, 2800 $cm^{-1}$, is slightly larger than the theoretical spectral bandpass. The resolution of the bands at 2263 $cm^{-1}$ and 2943 is ~18 and 20 $cm^{-1}$ respectively, lower than expected partly because of the large spectral range shown. In comparison to previously published UV Raman spectra of acetonitrile,[20-21] the relative intensities of the 2943 and 2263 $cm^{-1}$ (CN stretching) bands are much lower relative to the 921 $cm^{-1}$ band, because the instrument response function (see dashed line in Fig. 5) decreases rapidly for the highest energy bands that are far away from the Littrow wavelength.

The interferogram shown in the inset of Fig. 5 illustrates another issue with the current deep-UV SHRS system, poor fringe visibility. Fringe visibility (FV) is one measure of the efficiency of the interferometer and calculated using Eqn. 6:

$$FV = (\mathrm{I_{max}} - \mathrm{I_{min}})/(\mathrm{I_{max}} + \mathrm{I_{min}}) \qquad (6)$$

where, $I_{max}$ and $I_{min}$ are the bright and dark line intensity of the interferogram fringes. The fringe visibility is equal to one for an ideal interferogram. Values less than one indicate incoherent light reaching the detector that does not contribute to the spectral intensity, and thus increases the background leading to higher levels of shot noise in the spectrum. The fringe visibility for the acetonitrile Raman fringe pattern is about 0.08 and this is one of the main sources of the high noise level in the spectrum shown. Some of the main reasons for the poor fringe visibility in the current deep-UV SHRS system include imperfect focusing of the fringe image onto the CCD, poor optical quality of the beam splitter and diffraction gratings, and high levels of background from grating order overlap and other reflected light that reaches the CCD. We also sometimes have issues with table vibrations that can wash out the highest frequency fringes. A higher quality UV beam splitter would solve the former problem while background light issues might be addressed by a combination of spatial filters at the entrance and exit of the interferometer along with more careful component layout. Poor fringe visibility is currently the main limitation of the deep-UV SHRS.

The instrument response is estimated by the dashed line in Fig. 5. The response was estimated by measuring the intensity of the 253.6 nm Hg emission line (closed circles in Fig. 5) as the Littrow wavelength was changed from a ~254 nm to ~277 nm (e.g., a range of wavelengths that corresponds to a Raman shift of 0 to ~3200 cm$^{-1}$). This is only an estimate because for this measurement the grating angle is changed so that the 253.6 nm Hg emission line is further and further from the Littrow wavelength. In the Raman spectrum measurement, the grating is not moved so the two measurements are not exactly the same. During the instrument response measurement the Hg emission line intensity drops significantly as the wavelength difference between the emission line and the Littrow wavelength increases. However, total intensity of the interferogram cross section remains constant as the Littrow wavelength is changed (see Table 2.1). This suggests that the decrease in the Hg line intensity is not caused by optical light losses. Rather, the emission intensity drops because the fraction of the total collected light that produces a fringe pattern is reduced for the longer wavelengths (e.g., large Raman shifts). This result is consistent with a loss of contrast or focus in the fringe image for fringes that correspond to longer wavelengths, possibly the result of imperfect focusing of the CCD image or table vibrations that can wash out high frequency fringes during an exposure. Optical imperfections in the diffraction gratings might also lead to lower quality fringe images and a reduced ability to fully resolve closely spaced interference fringes in the CCD image. It is important to note that none of the fringe images that were used to produce the Raman spectra shown were processed in any way. For example, image artifacts were not removed, fringes were not straightened and no phase corrections were made before calculating the Raman spectra. correcting issues that lead to decreased fringe visibility will be more fully addressed in a future paper.

Figure 6 shows the SHRS Raman spectrum of acetonitrile for the same spectral region as Fig. 5, but this spectrum was obtained by splicing three separate spectra together, each measured using a Littrow wavelength close to the desired bands of interest. In this way, each region covers a spectral range that is small compared to the theoretical maximum bandpass so that the relative intensities are not as much affected by the instrument response function and fewer artifacts are observed. The low energy Raman bands, from 700 cm$^{-1}$ to 2000 cm$^{-1}$, were acquired in one measurement by setting Littrow close to 650 cm$^{-1}$ and using a 254 nm bandpass filter to block longer wavelengths. The bands at 2263 cm$^{-1}$ and 2943 cm$^{-1}$ were measured by setting Littrow to 2000 cm$^{-1}$ and 2800 cm$^{-1}$, respectively, using long pass filters centered at 248 nm and 257 nm to eliminate the low energy Raman bands. The acetonitrile spectrum obtained in this way matches well with the previously published results[20-21]. Moreover, the spectral resolution also improved. For example, the peaks at 2263 cm$^{-1}$ and 2943 cm$^{-1}$ exhibit the resolution ~10 cm$^{-1}$ and 14 cm$^{-1}$ respectively, better than the Figure 5 acetonitrile spectrum measured in a single attempt. The spectrum in Fig. 6 demonstrates the need for proper bandpass filtering in the SHRS because light that lies outside the spectral bandpass contributes shot noise to the spectrum.

### 3.4.3 Wide Area Measurements

UV Raman measurements can be difficult because strong sample absorption in the UV leads to a very short optical path length and reduced Raman signals. Also, strong UV absorption often leads to photodecomposition of the sample. To minimize laser induced damage, samples are often moved or spun during the measurement. The wide field of view and large entrance aperture of the SHRS allows a different approach to reduce laser-induced sample damage that does not require reducing the laser power. For the SHRS used in these studies the field of view (FOV) is about 1° or 2.5 mm using an f/3, 75 mm focal length collection lens. By comparison, the FOV of a typical f/6 UV dispersive Raman spectrometer using 30 μm slits and the same 75 mm focal length collection lens, f/# matched to the spectrometer would be 15 μm. In this example, the area of the sample that is viewed by the SHRS is ~7000 times larger than the area viewed by the dispersive system. The use of a large laser spot on the sample allows the irradiance at the sample to remain low, avoiding laser sample damage, while still maintaining an overall high laser power.

Figure 7 shows 244-nm excited Raman spectra of sodium sulfate measured using 5 mW at the sample, for a tightly focused 30 μm laser spot (a) and for a much larger 2500 μm laser spot (b), a difference in irradiance of about 7000. Sodium sulfate is very stable in the UV laser beam and the two spectra have similar intensities, showing that no light is lost by the SHRS when a large laser spot is used. In addition, the spectral resolution (~12 $cm^{-1}$) for the 993 $cm^{-1}$ band is the same for spectra acquired using the focused or unfocused laser.

Figure 8 shows UV Raman spectra of ammonium nitrate excited at 244-nm using 5 mW with a 25 µm laser spot on the sample (a), and 1500 µm laser spot (b), a difference in irradiance of about 3600. In A, no Raman bands are observed due to decomposition of the ammonium nitrate by the high laser irradiance, while in (b) the Raman spectrum is observed and the spectral features in Fig. 8(b) match those of ammonium nitrate that were recorded using visible excitation.[26-27]

### 3.4.4 Fluorescence-Free Deep UV Raman

Exciting the sample at 244 nm, sample or impurity fluorescence is not expected to overlap the Raman spectral range. This is known as the fluorescence-free region. However, with the SHRS any fluorescence that occurs will still contribute shot noise to the Raman spectrum even though fluorescence does not show up in the Raman spectrum itself. Therefore, it is important to use optical filters to restrict light outside of the Raman spectral region from reaching the detector. Fig. 9 shows the Raman spectrum using 244-nm excitation of acetonitrile spiked with 1.45 ppm of Rhodamine 6G (Rh6G), a highly fluorescent compound. To obtain this spectrum a 300 nm short pass filter (Semrock FF01-300/SP) was used to block the long wavelength fluorescence without effecting the Raman signal that occurs at much shorter wavelengths. Fig. 10 shows the fluorescence spectrum of Rh6G along with the transmission profile of the 300 nm short pass filter and the position of the 244-nm laser line. In the absence of this filter, the Raman spectrum was extremely noisy. The Raman spectrum in Fig. 9 clearly shows that fluorescence-free Raman spectra can be acquired using deep UV excitation for the first time with the SHRS. This study also shows the importance of proper bandpass filtering in the SHRS, or any nondispersive spectrometer, to minimize shot noise contributions from light collected outside the spectral bandpass range of the instrument.

### 3.5 Conclusions

For the first time, a spatial heterodyne Raman spectrometer is demonstrated for deep UV Raman measurements. Using 244 nm excitation wavelength and SHRS with ~4 $cm^{-1}$ spectral resolution and ~2623 $cm^{-1}$ bandpass, we measured the Raman spectra of several solid and liquid samples with good signal to noise ratio and showed near-theoretical resolution and spectral bandpass. The significance of the wide acceptance angle of the SHRS was also demonstrated by using a large laser spot to eliminate laser-induced damage to a UV-light sensitive compound, ammonium nitrate. In addition the use of deep-UV excitation to mitigate fluorescence was demonstrated by measuring acetonitrile spiked with Rhodamine 6G. Although the deep-UV SHRS Raman instrument looks promising, the SNR of the SHRS is currently limited by poor fringe visibility caused by high background signals from imperfections in the optical components. Future work will focus on assessing the effect of optical quality on interferogram fringe visibility, SNR of the resulting spectra and the use postprocessing techniques to remove spectral artifacts.

### 3.6 Acknowledgements

We would like to thank the National Science Foundation for supporting this work under grant CHE-1308211 and NASA for support under grant NNX14AI34G and NASA/SC Space Grant 21-NE-USC_Angel-RGP. We also thank the Research Corporation of the University of Hawaii (RCUH) /NAVSEA/DOD, for partial support of this work under contract No. ZA01339.

## 3.7 References

1. M. Angel, N.R. Gomer, S.K. Sharma, C. McKay. “Remote Raman Spectroscopy for Planetary Exploration: A Review”. Appl. Spectrosc. 2012. 66(2): 137-150.

2. C.S. Garcia, M.N. Abedin, S. Ismail, S.K. Sharma, A.K. Misra, T. Nguyen, H. Elsayed-Ali. “Study of Minerals, Organic, and Biogenic Materials through Time-Resolved Raman Spectroscopy”. In: T. Vo-Dinh, R.A. Lieberman,G. Gauglitz, editors. Advanced Environmental, Chemical, and Biological Sensing Technologies VI. Proc. SPIE. 2009. 7312:

3. J.J. Freeman, A. Wang, K.E. Kuebler, B.L. Jolliff, L.A. Haskin. “Characterization of Natural Feldspars by Raman Spectroscopy for Future Planetary Exploration”. Can. Mineral. 2008. 46(6): 1477-1500.

4. I.A. Degen, G.A. Newman. “Raman Spectra of Inorganic Ions”. Spectrochimica Acta, Part A. 1993. 49: 859-887

5. H.G.M. Edwards, F. Sadooni, P. Vitek, J. Jehlicka. “Raman Spectroscopy of the Dukhan Sabkha: Identification of Geological and Biogeological Molecules in an Extreme Environment”. Phil. Trans. R. Soc. A. 2010. 368: 3099-3107.

6. T.F. Cooney, E.R.D. Scott, A.N. Krot, S.K. Sharma, A. Yamaguchi. “Vibrational Spectroscopic Study of Minerals in the Martian Meteorite ALH 84001”. American Mineralogist. 1999. 84 (10): 1569-1576.

7. A. Ellery, D. W. Williams. “Why Raman Spectroscopy on Mars?-A Case of the Right Tool for the Right Job”. Astrobiology. 2003. 3(3): 565-579.

8. R. Bhartia, W.F. Hug, R.D. Reid. “Improved Sensing Using Simultaneous Deep UV Raman and Fluorescence Detection”. In: A. W. Fountain, editor. Chemical, Biological, Radiological, Nuclear, and Explosives (CBRNE) Sensing XIII. Proc. SPIE. 2012. 83581: 83581A/1-83581A/9.

9. S.A. Asher and C. R. Johnson, “Raman Spectroscopy of a Coal Liquid Shows that Fluorescence Interference is Minimized with Ultraviolet Excitation”. Science. 1984. 225: 311-313.

10. M. Ghosh, L. Wang, S.A. Asher. “Deep-Ultraviolet Resonance Raman Excitation Profiles of NH4NO3, PETN, TNT, HMX, and RDX”. Appl. Spectrosc. 2012. 66(9): 1013-1021.

11. S.A. Asher. “UV Resonance Raman Spectroscopy for Analytical, Physical, and Biophysical Chemistry. Part 1”. Anal. Chem. 1993. 65(2): 59-66.

12. N.R. Gomer, C.M. Gordon, P. Lucey, S.K. Sharma, J.C. Carter, S.M. Angel. “Raman Spectroscopy Using a Spatial Heterodyne Spectrometer: Proof of Concept”. Appl. Spectrosc. 2011. 65(8): 849-857.J.M. Harlander. Spatial Heterodyne Spectroscopy: Interferometric Performance at any Wavelength Without Scanning. [Ph.D. Thesis]. Madison, Wisconsin: The University of Wisconsin, 1991.

13. J.M. Harlander, F.L. Roesler, S. Chakrabarti. “Spatial Heterodyne Spectroscopy: A Novel Interferometric Technique for the FUV”. In: O. H. W. Siegmund; H. S. Hudson, editors. EUV, X-Ray, and Gamma-Ray Instrumentation for Astronomy. Proc. SPIE. 1990. 1344: 120-131.

14. J.M. Harlander, F.L. Roesler, J.G. Cardon, C.R. Englert, R.R. Conway. “Shimmer: A Spatial Heterodyne Spectrometer for Remote Sensing of Earth’s Middle Atmosphere”. Appl. Opt. 2002. 41(7): 1343-1352.

15. J. Harlander, R. Reynolds, F. Roesler. “Spatial Heterodyne Spectroscopy for the Exploration of Diffuse Interstellar Emission-Lines at Far-Ultraviolet Wavelengths”. Astrophys. J. 1992. 396(2): 730-740.

16. W. Harris, F. Roesler, L. Ben-Jaffel, E. Mierkiewicz, J. Corliss, R. Oliversen, T. Neef. “Applications of Spatial Heterodyne Spectroscopy for Remote Sensing of Diffuse UV–Vis Emission Line Sources in the Solar System”. Journal of Electron Spectroscopy and Related Phenomena. 2005. 144-147(0): 973-977.

17. S. Prawer, R.J. Nemanich. “Raman Spectroscopy of Diamond and Doped Diamond”. Philosophical Transactions of the Royal Society A: Mathematical, Physical and Engineering Sciences. 2004. 362(1824): 2537-2565.

18. A.W. Birley. “Atlas of Polymer and Plastics Analysis (2nd Edition)”. British Polymer Journal. 1990. 22(2): 173-174.

19. M. Wu, M. Ray, K.H. Fung, M.W. Ruckman, D. Harder, A.J. Sedlacek. “Stand-off Detection of Chemicals by UV Raman Spectroscopy”. Appl. Spectrosc. 2000. 54(6): 800-806.

Table 3.1. Table shows the change in interferogram cross section, fringe visibility (FV) and band intensity of Hg 254.5 nm (39370 cm$^{-1}$) line with increase in Littrow wavenumber.

| Littrow Position (nm) | Raman shift (cm$^{-1}$) | Interferogram Cross section(X10$^{7}$) | FV | Intensity (X10$^{6}$) |
|---|---|---|---|---|
| 253.8 | 733 | 8.72 | 0.301 | 4.02 |
| 256.9 | 1200 | 8.74 | 0.300 | 4.54 |
| 259.2 | 1547 | 8.71 | 0.284 | 3.18 |
| 263.0 | 2105 | 8.66 | 0.202 | 0.98 |
| 268.0 | 2824 | 8.47 | 0.188 | 0.48 |
| 270.8 | 3204 | 8.69 | 0.064 | 0.23 |

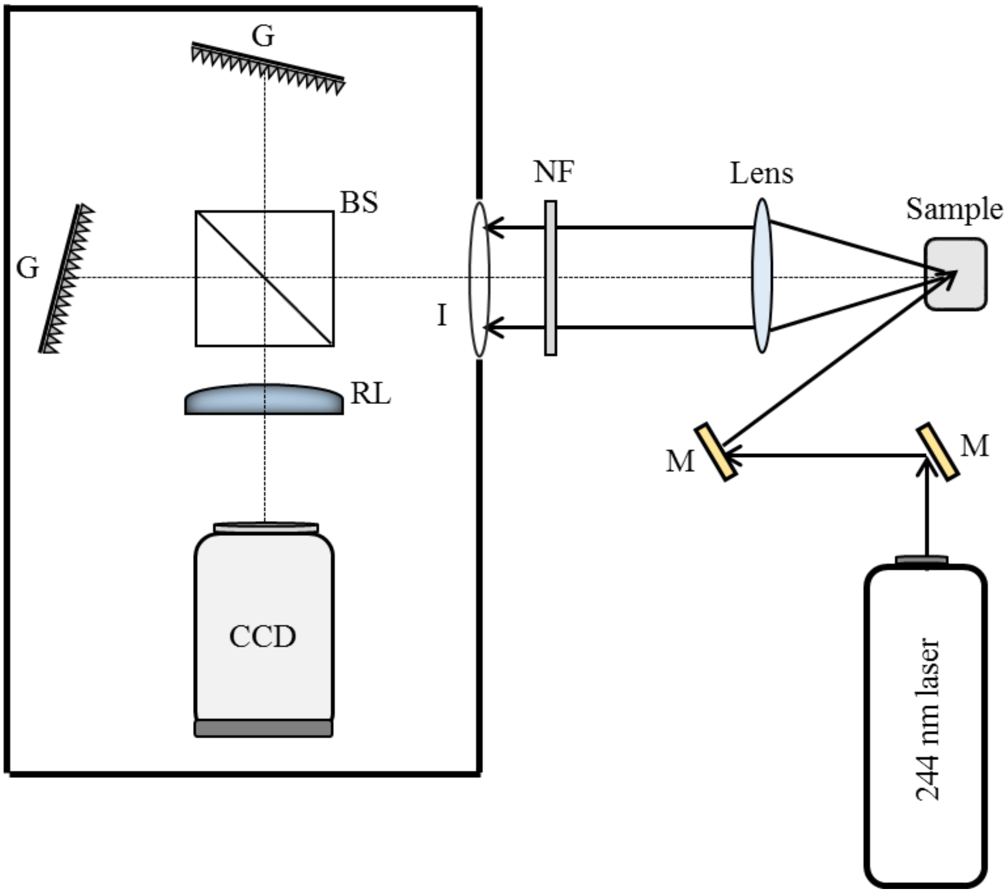

Figure 3.1. Spatial heterodyne Raman spectrometer system layout for UV Raman measurements, with symbols meaning: (M) Mirror, (NF) notch filter/ laser rejection filter, (I) iris/aperture, (BS) beamsplitter, (G) grating, (IL) imaging lens and (CCD) charge coupled device. The sample was illuminated with the 244 nm laser incident on the sample, at 150o with respect to the collection lens optical axis.

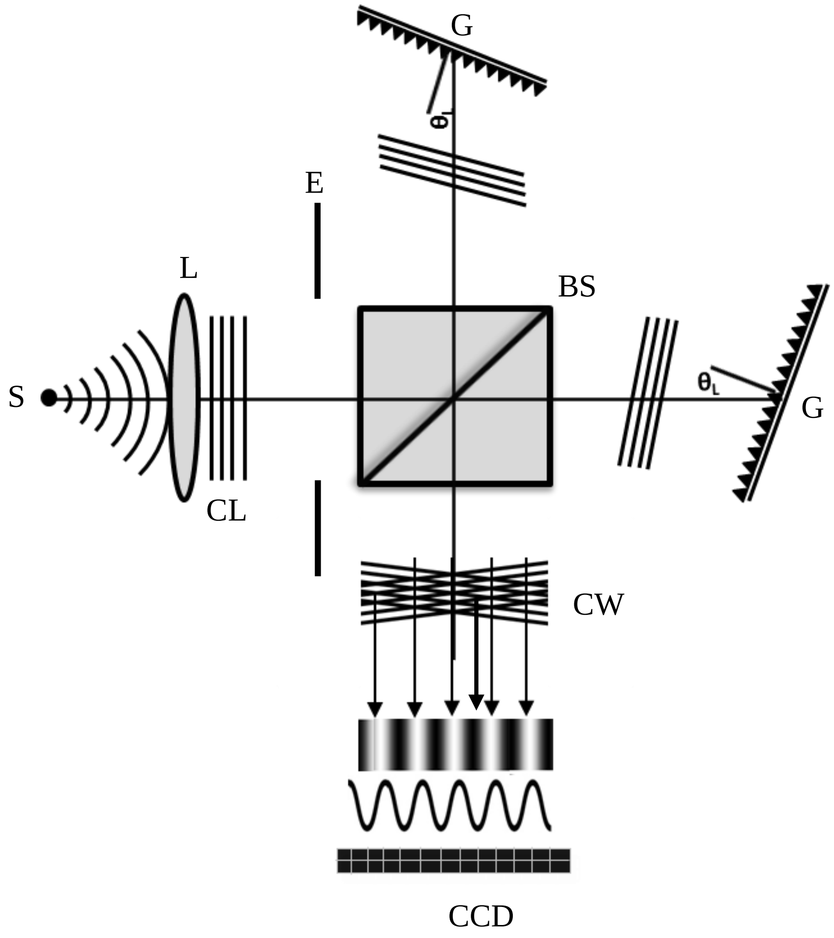

Figure 3.2. Schematic of a spatial heterodyne spectrometer used for Raman measurements. S= scattered light, L=lens, CL= collimated light, E= entrance aperture, G= grating; BS= beam splitter; CW= crossed wavefronts exiting the SHRS.

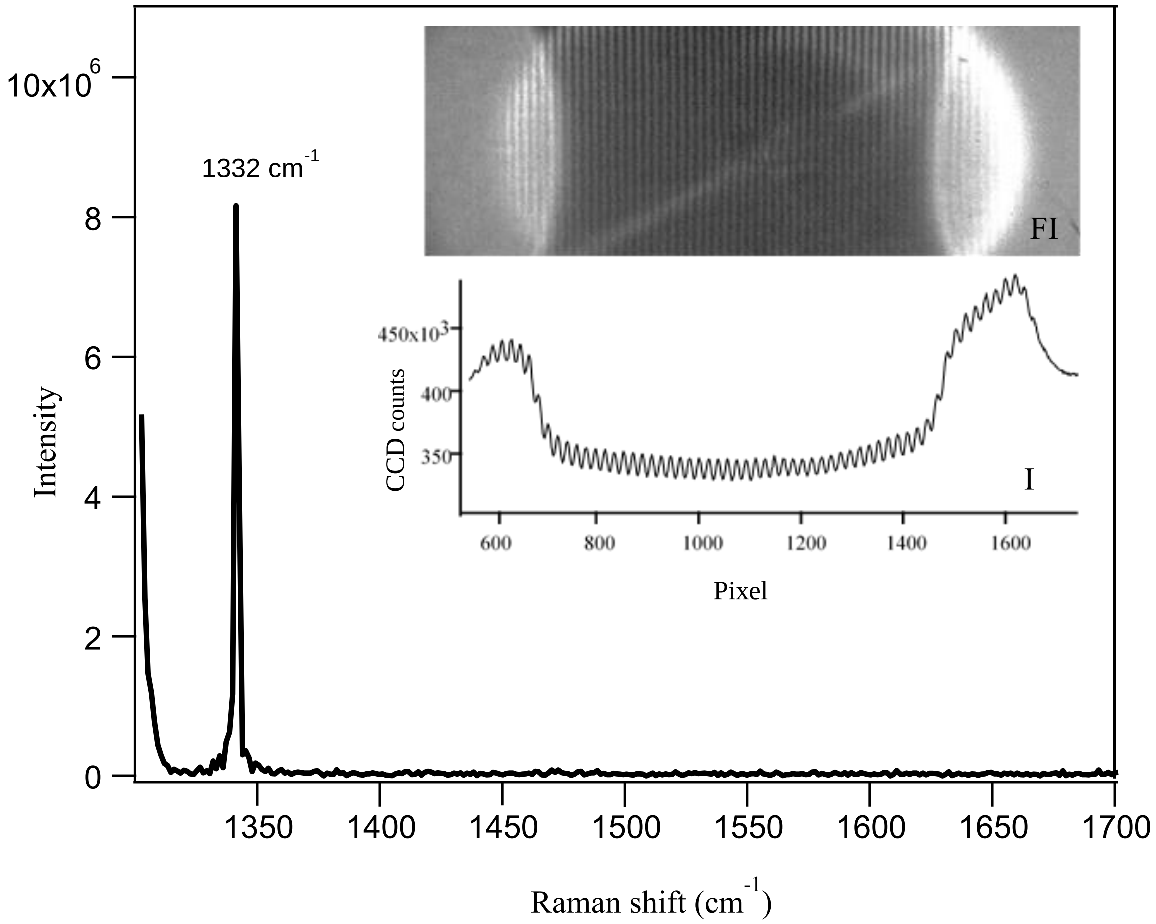

Figure 3.3.SHRS Raman spectrum of diamond shown is the Fourier transform of the interferogram (I) cross section, which is formed by summing the intensity of each column of pixels in the fringe image (FI).The spectrum was acquired using 13 mW, 244 nm excitation, 60 second integration time and Littrow set to 1300 $cm^{-1}$.

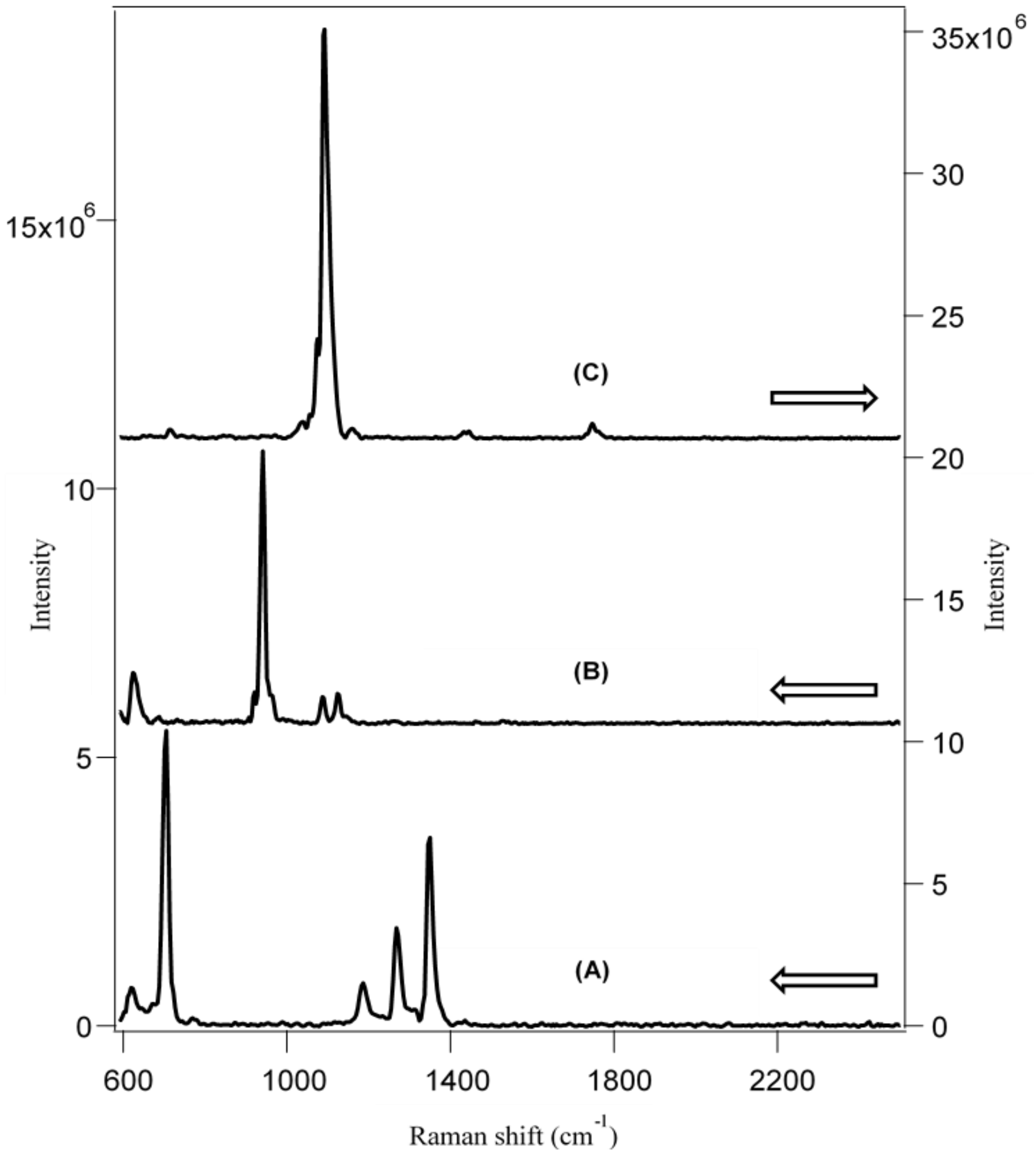

Figure 3.4. SHRS Raman spectra of (A) Teflon, (B) potassium perchlorate and (C) calcite measured using the SHRS spectrometer with Littrow set to ~590 cm$^{-1}$. The arrows above each spectrum refer to the appropriate intensity axis for that spectrum. The other parameters include integration time 60 seconds, 244 nm excitation and 5 mW laser power at the sample. Spectra are offset vertically for clarity.

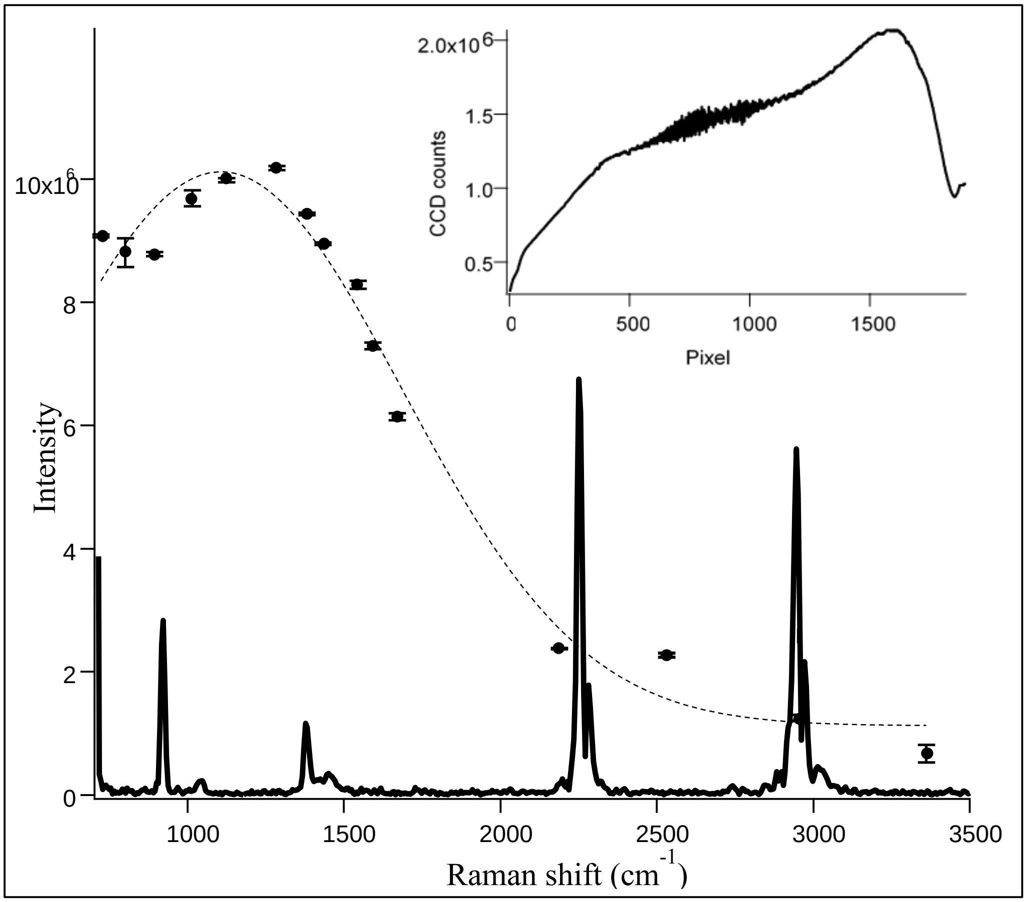

Figure 3.5. SHRS Raman spectrum of acetonitrile and interferogram fringe image cross section (top inset). The spectrum was acquired with the sample in a 1 cm quartz cuvette using 244 nm excitation and 13 mW laser power at the sample with 60-second exposure time. Dashed line: instrument response function for the SHRS system. The SHRS instrument response function was determined by measuring the 253.5 nm Hg emission line intensity (filled circle) as function of Littrow wavelength and fitting a polynomial curve to the resultant response.

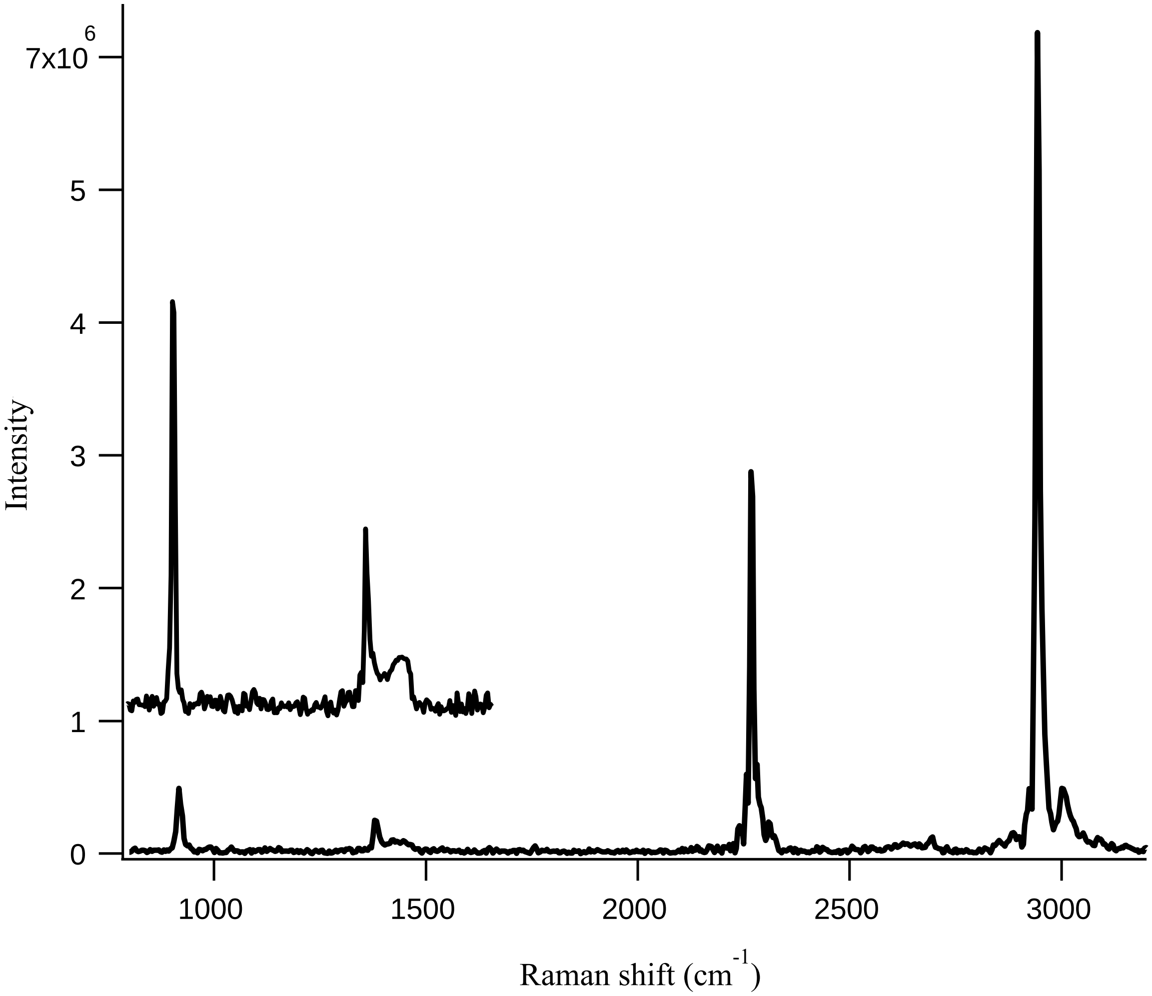

Figure 3.6. SHRS Raman spectrum of acetonitrile acquired by collecting three separate spectra using Littrow settings of ~700 cm$^{-1}$, ~2800 cm$^{-1}$ and 2800 cm$^{-1}$, and stitching the resultant spectra together. Each spectrum was acquired using 244 nm excitation, 5 mW laser power and 60 second exposure time with the samples placed in 1 cm quartz cuvette.

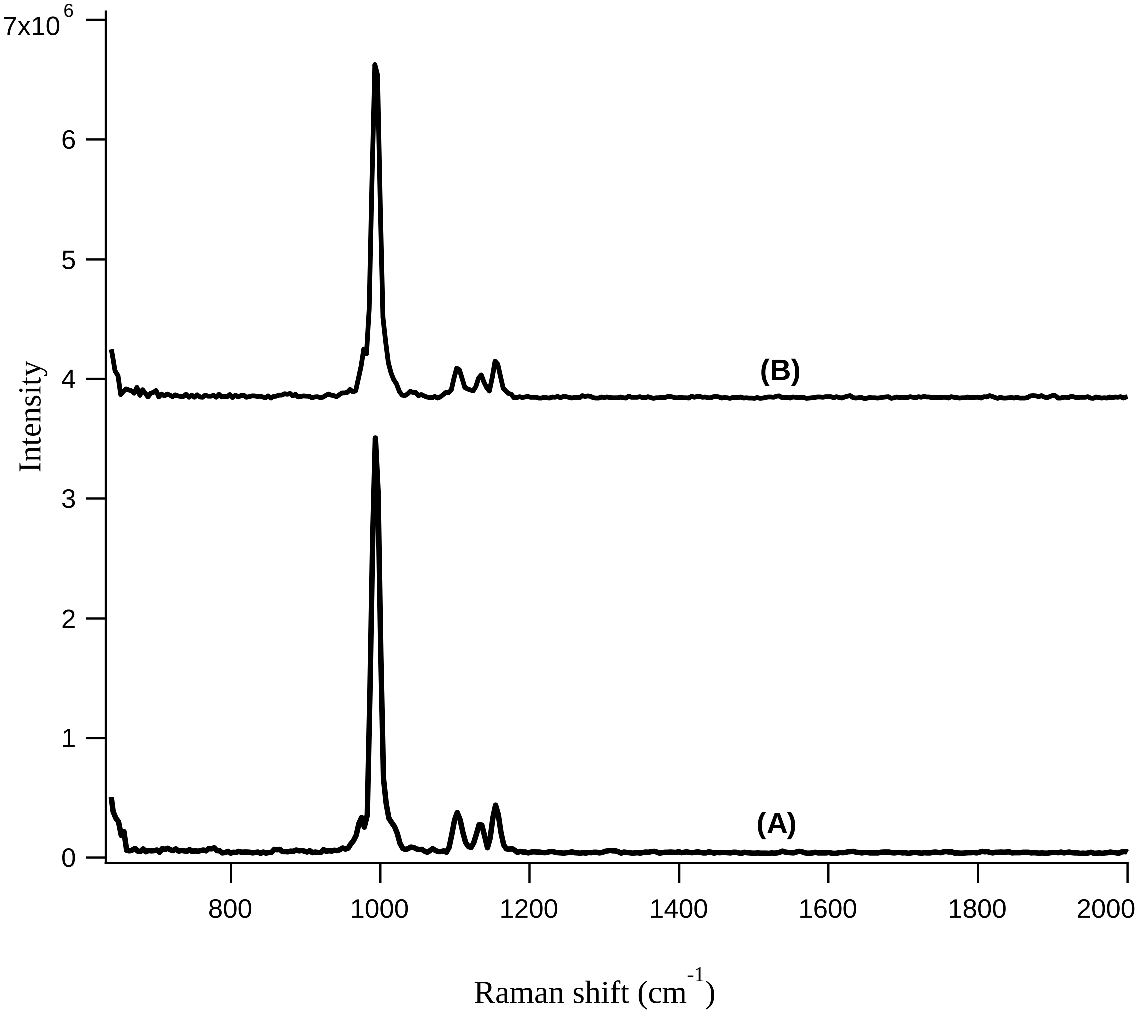

Figure 3.7. SHRS Raman spectra of sodium sulfate for (A) focused (30 μm diameter) and (B) unfocussed (2500 μm) laser spots on the sample. The spectra were obtained using 244 nm excitation, 5 mW laser power at the sample and 60 second exposure time with Littrow setting to ~600 cm$^{-1}$

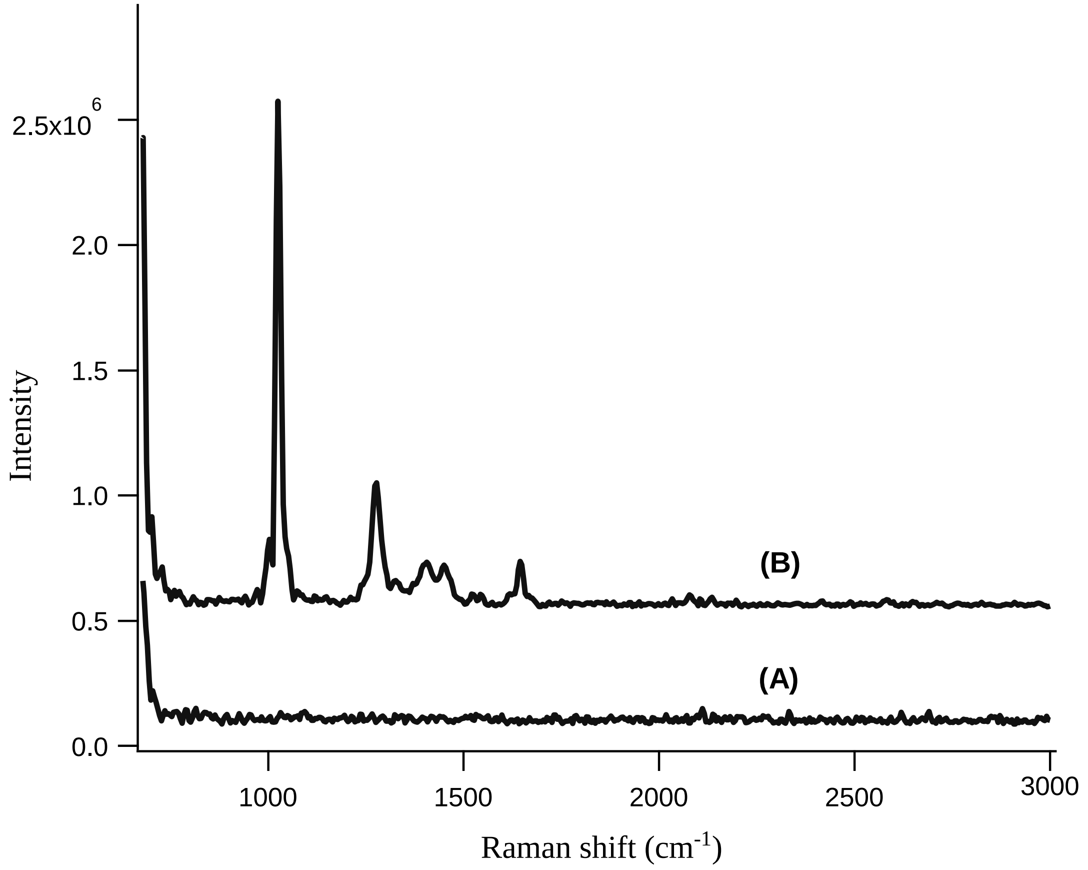

Figure 3.8 SHRS Raman spectra of ammonium nitrate for (A) focused (25 μm diameter) and (B) unfocussed (1500 μm) laser on the sample. The spectra were acquired using 244 nm excitation, 5 mW laser power at sample and 60 seconds exposure time with Littrow set to 670 cm$^{-1}$.

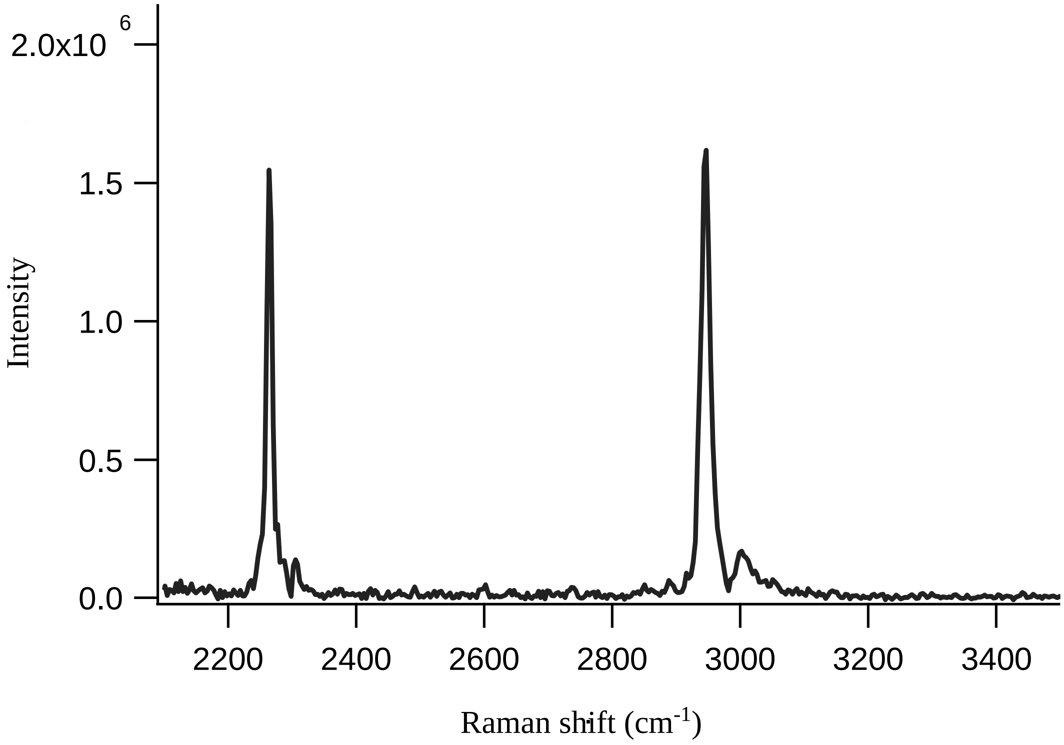

Figure 3.9 SHRS Raman spectrum of acetonitrile spiked with 1.45 ppm Rhodamine 6G. The spectra were acquired using 244 nm excitation, 5 mW laser power at the sample and 60 second exposure time with the Littrow set to ~2000 $cm^{-1}$. A 300 nm short pass optical filter was used to block fluorescence.

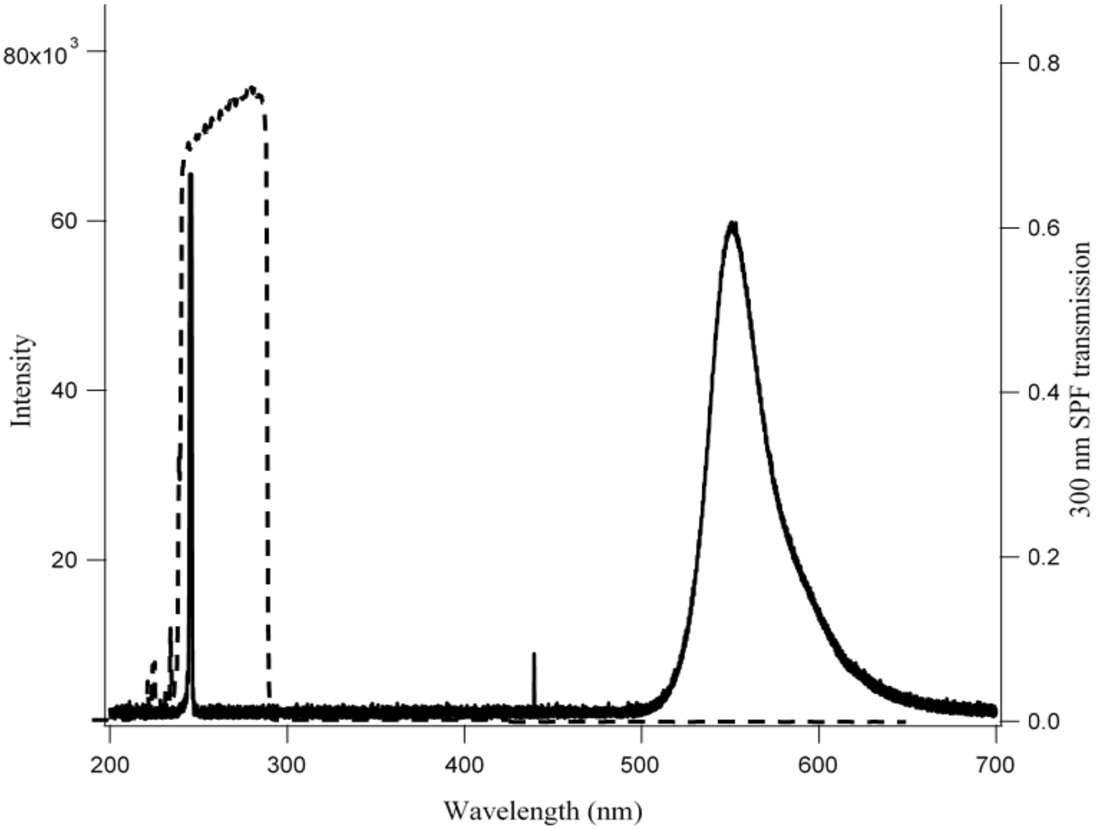

Figure 3.10 UV excited fluorescence spectrum of 1.45 ppm Rhodamine 6G in acetonitrile, measured using ocean optics spectrometer (Model: USB4000-UV-VIS) The dashed line shows the transmission profile of the 300 nm short pass filter that was used to acquire the UV Raman spectrum shown in Fig. 9. Other parameters include 244 nm excitation, 5 mW laser power at sample and one second acquisition time.

# Chapter 4

## Standoff Spatial Heterodyne Raman Spectroscopy

### 4.1. Background

Standoff Raman spectroscopy has been defined as Raman spectroscopy performed where the spectrometer (and therefore the operator) is some distance from the sample under interrogation.[1] The basic idea of standoff Raman spectroscopy is well illustrated in Fig. 4.1. In general, a laser is used to illuminate the sampling region, which can potentially be at any distance from the instrument and the return light is collected by a telescope. Standoff Raman spectroscopy is a valuable tool for remote detection and identification of chemicals for the applications where close proximity to the target is potentially hazardous[2] (e.g., explosives), or where remote measurement is the only option, like space applications.[3] The key features that make Raman spectroscopy an ideal tool for standoff measurements include:1)Raman is a scattering technique, that is, there is no need for sample preparation; a necessary condition for field-based measurements where the sample is inaccessible, 2) Raman shifts are independent of excitation wavelength, consequently, the daylight measurements can be accomplished using a deep UV laser in the solar blind region,[4] 3) The use of a pulsed laser and fast-gated detection system allows measurements to be made in ambient light conditions and also enables real time monitoring of samples, 4) Raman measurements can also be conducted in extreme environmental conditions such as in fog [4] heavy rain,[5] snow[6] and at elevated temperatures[7].

The basic concept of standoff Raman spectroscopy was first described in 1968.[8] However, it was not until the early 1970s that instrumentation was developed to the point that remote Raman of atmospheric gases was possible.[9-12] The first truly portable, stand-off Raman spectrometer was described in 1992 by Angel[13] and his group for the measurement of inorganic compounds such as $K_4[Fe(CN)_6]$, $NaNO_2$ and $NaNO_3$, as well as organic substances like $CCl_4$ and acetaminophen, at tens of meters for analysis of radioactive wastes in underground storage tanks. Since 1992 the number of publications describing standoff Raman systems and applications has steadily increased with measurements described at ranges from meters, up to 500 meters.[14,15]Applications of standoff Raman include analysis of art and archeological artifacts,[16] hazardous chemical detection,[2,17,18] environmental and geochemical measurements,[19] and measurements in space science[3]. The application of standoff Raman to geological measurements is a very active area, pioneered by Sharma and his groups.[19]

## 4.2. Standoff Raman system and Instrumentation Overview

The essential parts of a standoff Raman system are similar to that of a traditional Raman system, with the main component being a laser, collection optics, spectrometer, detector, and optical filters. The major difference is the use of a telescope for collection of scattered radiation from the remote target. The telescope is incorporated to compensate for the diminished signal with distance. Like in conventional Raman measurements, both pulsed and CW lasers have been used, but pulsed lasers are usually preferred for their ability to be coupled with gated detectors, helpful in reducing ambient light background during daytime measurements. Most standoff Raman systems utilize a charge-coupled device (CCD) or intensified CCD (ICCD) detectors. ICCD detectors are most common because they can be synchronized with the pulsed laser, allowing collection only during the arrival time of Raman photons at the detector so that ambient light can be effectively minimized. Additionally a pulsed laser with a gated ICCD detector offers the opportunity of conducting time-resolved measurements, which helps to discriminate fluorescence in luminescent minerals.[21] A number of spectrometer designs have been proposed for analyzing collected light, some of them include, dispersive, coded aperture,[21] AOTF,[22] among which the dispersive spectrometers are the most commonly used. A study by Sharma et al.[23] revealed that small f/# number spectrometers perform better than larger f/# spectrometers for standoff systems.

## 4.3 Geometry of Collection optics

Since, the scattered radiation is collected from a distance, the sample being illuminated with a laser must be in a line of sight of the collection optics, and a minor misalignment could result in a huge loss in signal. Therefore, the collection optics and laser must be properly aligned. The geometry of the laser and the telescope relative to the sample location can be set up in two ways, coaxial and oblique (sometimes referred to as bi-axial). Figure 2 shows a typical co-axial optical layout for standoff configuration. In a co-axial geometry (path A in Fig 2), the sample is illuminated with the laser, which is the optical axis of the telescope, by using small mirrors or prisms. The benefit of this configuration is that the realignment is not necessary while changing the sample position.[23] However, there is the possibility of decrease in signal intensity due to a loss of laser power at the beam steering optics. In an oblique geometry (path B in Fig. 2), the excitation laser is placed next to the telescope, and is focused onto the target that also corresponds to the focal point of the telescope. The primary benefit of oblique geometry is that it retains the full power of the laser. However, the system has to be realigned if the target or sample distance changes.[23] Sharma and his research group showed that co-axial configuration offers a wider range of sampling depth while oblique preserve the scattering signal.[13]

### 4.4 Standoff system coupling

Coupling the SHRS to the light collection optics is relatively straightforward. However, the overall system must be designed accurately to avoid optical losses. Light from the output of the telescope after passing through laser blocking filters can be efficiently transferred to the spectrometer in two ways; directly using intermediate lenses or by using fiber optic cables. The choice of method largely depends on the size of the spectrometer and the available space. A fiber optic coupling is easy to implement, and gives more freedom and flexibility in placing the individual components, but can lead to system inefficiency due to the small fiber size and optical losses inside the fiber. A study by Mishra et al. showed that a directly coupled system offers better performance over a fiber coupled system by a factor of 10 for a system with coaxial geometry.[18] However, directly coupled systems need more space as all components have to be on the same axis and can be much heavier than a fiber optic couple. Both types of coupling have been proven useful for planetary measurements because of their small size, mass, and low power requirements [18]

## 4.5 References

1. A.J. Hobro, B. Lendl. “Stand-off Raman spectroscopy”. TrAC Trends Anal. Chem. 2009. 28(11): 1235–1242.
2. Existing and Potential Standoff Explosives Detection Techniques. National Academies Press, Washington, D.C., 2004.
3. S.M. Angel, N.R. Gomer, S.K. Sharma, C. McKay. “Remote Raman Spectroscopy for Planetary Exploration: A Review”. Appl. Spectrosc. 2012. 66(2): 137–150.
4. M. Wu, M. Ray, K.H. Fung, M.W. Ruckman, D. Harder, A.J. Sedlacek. “Stand-off Detection of Chemicals by UV Raman Spectroscopy”. Appl. Spectrosc. 2000. 54(6): 800–806.
5. A. Pettersson, S. Wallin, H. Östmark, A. Ehlerding, I. Johansson, M. Nordberg, et al. Explosives standoff detection using Raman spectroscopy: from bulk towards trace detection. In: R.S. Harmon, J.H. Holloway, Jr., J.T. Broach, editors. 2010. P. 76641K–76641K–12.
6. A. Pettersson, I. Johansson, S. Wallin, M. Nordberg, H. Östmark. “Near Real-Time Standoff Detection of Explosives in a Realistic Outdoor Environment at 55 m Distance”. Propellants Explos. Pyrotech. 2009. 34(4): 297–306.
7. J.P. Young, S. Dai, Y. Lee, H. Xizo. Application of Raman Spectroscopy to High-Temperature Analytical Measurements. Oak Ridge National Lab., TN (United States), 1997.
8. J. Cooney. "Satellite Observations Using Raman Component of Laser Backscatter". In: Ralph Zirkind editor. New York: Polytechnic Institute of Brooklyn Press, 1967. Pp. P1-P1
9. .T. Hirschfeld. “Remote spectroscopic analysis of ppm-level air pollutants by Raman spectroscopy”. Appl. Phys. Lett. 1973. 22(1): 38.
10. J. Cooney, K. Petri, A. Salik. “Measurements of high resolution atmospheric water-vapor profiles by use of a solar blind Raman lidar”. Appl. Opt. 1985. 24(1): 104.
11. D.A. Leonard. “Observation of Raman Scattering from the Atmosphere using a Pulsed Nitrogen Ultraviolet Laser”. Nature. 1967. 216(5111): 142–143.
12. U.N. Singh, Z. Chu, R. Mahon, T.D. Wilkerson. “Optimization of a Raman shifted dye laser system for DIAL applications”. Appl. Opt. 1990. 29(12): 1730.

13. S.M. Angel, T.J. Kulp, T.M. Vess. “Remote-Raman Spectroscopy at Intermediate Ranges Using Low-Power cw Lasers”. Appl. Spectrosc. 1992. 46(7): 1085–1091.

14. S.K. Sharma, A.K. Misra, P.G. Lucey, S.M. Angel, C.P. McKay. “Remote Pulsed Raman Spectroscopy of Inorganic and Organic Materials to a Radial Distance of 100 Meters”. Appl. Spectrosc. 2006. 60(8): 871–876.

15. R.L. Aggarwal, L.W. Farrar, D.L. Polla. “Measurement of the absolute Raman scattering cross sections of sulfur and the standoff Raman detection of a 6-mm-thick sulfur specimen at 1500 m”. J. Raman Spectrosc. 2011. 42(3): 461–464.

16. P. Vandenabeele, J. Jehli ka. “Mobile Raman spectroscopy in astrobiology research”. Philos. Trans. R. Soc. Math. Phys. Eng. Sci. 2014. 372(2030): 20140202–20140202.

17. S. Sadate. “Standoff Raman Spectroscopy of Explosive Nitrates Using 785 nm Laser”. Am. J. Remote Sens. 2015. 3(1):1.

18. G. Tsiminis, F. Chu, S. Warren-Smith, N. Spooner, T. Monro. “Identification and Quantification of Explosives in Nanolitre Solution Volumes by Raman Spectroscopy in Suspended Core Optical Fibers”. Sensors. 2013. 13(10): 13163–13177.

19. A.K. Misra, S.K. Sharma, C.H. Chio, P.G. Lucey, B. Lienert. “Pulsed remote Raman system for daytime measurements of mineral spectra”. Spectrochim. Acta. A. Mol. Biomol. Spectrosc. 2005. 61(10): 2281–2287.

20. A.K. Misra, S.K. Sharma, P.G. Lucey. “Remote Raman Spectroscopic Detection of Minerals and Organics Under Illuminated Conditions from a Distance of 10 m Using a Single 532 nm Laser Pulse”. Appl. Spectrosc. 2006. 60(2): 223–228.

21. B.J. Bozlee, A.K. Misra, S.K. Sharma, M. Ingram. “Remote Raman and fluorescence studies of mineral samples”. Spectrochim. Acta. A. Mol. Biomol. Spectrosc. 2005. 61(10): 2342–2348.

22. E.C. Cull, M.E. Gehm, B.D. Guenther, D.J. Brady. Standoff raman spectroscopy system for remote chemical detection. In: A.J. SedlacekIII, S.D. Christesen, R.J. Combs, T. Vo-Dinh, editors. 2005. P. 59940H–59940H–8.

23. N. Gupta, R. Dahmani. “AOTF Raman spectrometer for remote detection of explosives”. Spectrochim. Acta. A. Mol. Biomol. Spectrosc. 2000. 56(8): 1453–1456.

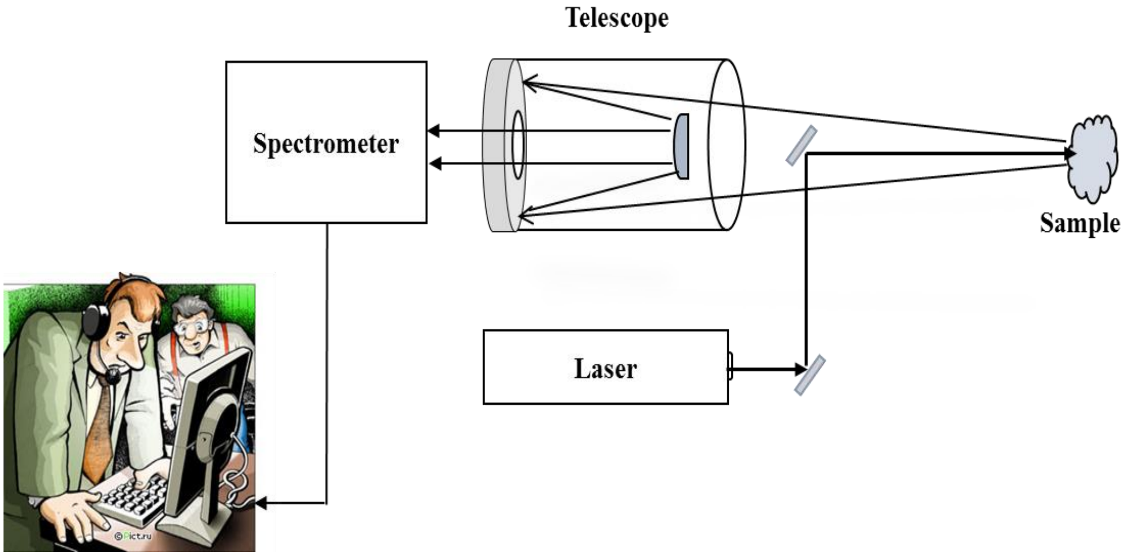

Figure 4.1. Typical optical system schematic for a standoff Raman spectroscopy. The picture in bottom inset was taken from www.pict.ru.

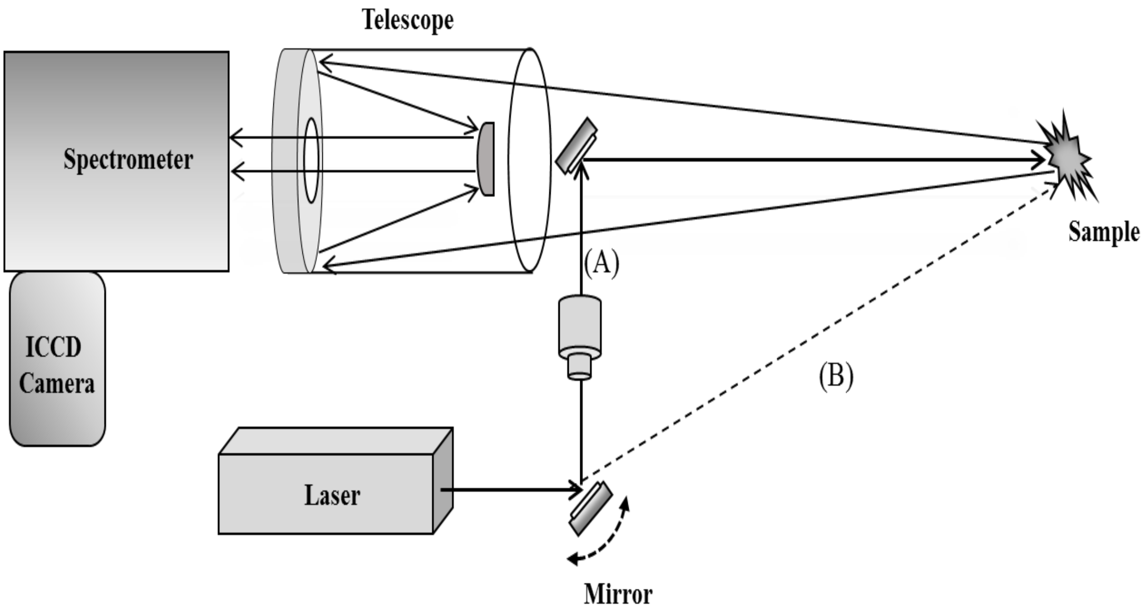

Figure. 4.2. Schematic of standoff Raman system showing (A) co-axial, used for UV excitation, and (B) oblique, used for visible excitation, geometries for laser and telescope optical paths.

## Chapter 5

## UV Standoff Raman Measurements Using a Gated Spatial Heterodyne Raman Spectrometer[B]

### 5.1 Abstract

A spatial heterodyne Raman spectrometer (SHRS) is evaluated for standoff Raman measurements in ambient light conditions using both UV and visible pulsed lasers with a gated ICCD detector. The wide acceptance angle of the SHRS simplifies optical coupling of the spectrometer to the telescope and does not require precise laser focusing or positioning of the laser on the sample. If the laser beam wanders or loses focus on the sample, as long as it is in the field of view of the SHRS, the Raman signal will still be collected. The SHRS is not overly susceptible to vibrations, and a vibration isolated optical table was not necessary for these measurements. The system performance was assessed by measuring standoff UV and visible Raman spectra of a wide variety of materials at instance up to 18 m, using 266 nm and 532 nm pulsed lasers, with 12.4” and 3.8” aperture telescopes, respectively

---

[B] N. Lamsal, S.M. Angel, S.K. Sharma, T.E. Acosta. “UV Standoff Raman Measurements Using a Gated Spatial Heterodyne Raman Spectrometer.” Appl. Spectrosc. 2016. 70(4). Published online ahead of print by Sage Publications Ltd. The online version of this article can be found at http://asp.sagepub.com/content/early/2016/02/16/0003702816631304.full

## 5.2 Introduction

Raman spectroscopy is a valuable tool for chemical identification because the relatively sharp Raman bands provide detailed molecular structural information for organic and inorganic compounds.[1] Raman is a scattering technique and no sample preparation is required, thus Raman measurements can in principle be made for any sample within line of sight. This is taken advantage in standoff Raman spectroscopy where samples are measured from a distance, often desirable to minimize the risk associated with measuring hazardous samples like explosives, and also useful for measuring inaccessible samples. In standoff Raman spectroscopy, a laser is used to excite the sample at a distance (e.g., tens to hundreds of meters) from which the inelastic scattered Raman photons are collected using a large aperture optical system such as a telescope that is coupled to a Raman spectrometer.

Standoff Raman spectroscopy was initially developed in the 1960s,[2,3] and later used primarily for the detection of atmospheric gases such as sulfur dioxide, nitrogen and oxygen.[3-5] In 1992, standoff Raman was extended by Angel et al.,[6] to include the measurement of inorganic compounds such as $K_4[Fe(CN)_6]$, $NaNO_2$ and $NaNO_3$, as well as organic substances like $CCl_4$ and acetaminophen, at tens of meters using a portable standoff Raman system that was developed for analysis of radioactive wastes in underground storage tanks. Some recent improvements in standoff Raman systems include, the use of gated detection for daylight operations,[7,8] extreme range measurements up to 1500 m,[9] systems for explosives detection[8, 10-12] and planetary exploration,[13-15] and deep-UV systems which take advantage of higher Raman cross sections and resonance enhancement in the UV.[10, 16-22] UV excitation provides larger Raman cross sections and it has been shown that deep-UV Raman spectra are free from interference from longer wavelength fluorescence, which often plagues visible wavelength Raman measurements.[23]

Utilizing UV excitation for standoff Raman generally requires a high-resolution spectrometer to discern the Raman signal that occurs over a very narrow spectral range. Moreover, low laser irradiance must often be used to avoid laser-induced photodegradation of the sample. Spectrometers that provide sufficiently high spectral resolution for deep-UV standoff Raman typically are large and have low light throughput because of the need of large, high dispersion gratings, and long focal length optics.

The spatial heterodyne Raman spectrometer is a compact, high resolution instrument that has been shown to be useful in the deep-UV,[24,25] and might be well suited for standoff UV Raman measurements. The first spatial heterodyne Raman spectrometer (SHRS) was described by Gomer et al. for visible Raman measurements,[26] and extended into the deep UV by Lamsal et al.[24,25] The SHRS is based on a stationary diffraction grating, heterodyned interferometer. As such, there is no entrance slit; light enters the spectrometer through a large aperture, and the resolution of the spectrometer is not a strong function of the aperture size. Heterodyning in the interferometer allows high spectral resolution to be achieved with a relatively small number of samples, fixed by the number of horizontal pixels on the imaging detector. The large entrance aperture and wide acceptance angle of the SHRS provides high light throughput and allows large laser spots to be used on the sample without light loss or the loss of spectral resolution.

In the case of standoff Raman, this also makes the SHRS relatively easy to couple with telescopic optics and minimizes laser pointing stability issues, because small movements of the laser spot on the target do not reduce the amount of light collected by the spectrometer slit, unlike the case of a dispersive spectrometer where the output of the telescope has to be held in focus on a narrow input slit. In addition, all wavelengths are measured simultaneously in the SHRS, making it compatible with pulsed lasers and gated detection, which has been shown to be useful for making Raman measurements in daylight.[8] The SHRS is also not overly susceptible to vibrations and does not necessarily require a vibration isolation system. These characteristics make the SHRS especially suitable for UV standoff Raman measurements. In this work, we present standoff Raman spectra of several types of samples located up to 18 m from the spectrometer, using 266 and 532 nm pulsed laser excitation in bright light conditions, and without the use of a vibration isolation system.

### 5.3 Experimental

A schematic of the standoff SHRS instrument for Raman measurements is shown in Fig. 1.1 The system consists of three components; the excitation source, the light collection optics and the SHRS spectrometer.

#### 5.3.1 The excitation source

Q-switched Nd:YAG lasers were used to generate 532 nm (Quantel, Ultra CFR) and 266 nm (Quantel, Brilliant Eazy) laser pulses of pulse width 6 ns and 4 ns, respectively. The visible laser was operated at 20 Hz using 5.3 mJ/pulse, and the sample was illuminated at an angle of about 30° relative to the optical axis of the telescope (path b in Fig. 1). Note: 180° backscatter would have been preferred for this measurement but the proper mirrors were not available at the time of this study. The UV laser was operated at 10 Hz using 10.3

mJ/pulse, and the beam was collinear with the telescope optical axis. A beam expander was used to defocus the beam, creating large laser spots on the sample from ~7 mm for the closest samples, to ~25 mm for the samples at 20 m (path a in Fig. 1), to avoid laser-induced photodecomposition and sample heating. The average laser power was monitored using a power meter. In some cases laser pulse energy is provided, calculated form the average power measurement and the known laser pulse frequency.

### 5.3.2 Collection optics

For 532 nm standoff measurements, an f/16, 3.8-inch aperture telescope (Questar FR-1 MK III) with a collimated beam output was used for light collection. Light collected by the telescope was directly coupled to the SHRS, with laser rejection and spectral bandpass filters placed in the collimated beam before the SHRS entrance aperture. For 266 nm standoff measurements, an f/9.1, 12.4-inch aperture custom-made Ritchey Chretien telescope (Optical Guidance Systems, Model RC12.5), with UV optics was used for light collection. Light collected by the telescope was collimated using an anti-reflection coated, 1-inch diameter, f/12, fused silica lens, and guided to the SHRS by two flat aluminum coated mirrors.

### 5.3.3 SHRS spectrometer

The SHRS interferometer, shown in more detail schematically in Fig. 2, consists of a 20 mm fused silica cube beam splitter (Esco Optics, Model O420120, λ/10 Beamsplitter Cube) and a pair of 300 grooves/mm, 25 mm square diffraction gratings blazed at 300 nm. Two 532 nm or 266 nm laser-blocking filters were employed (Semrock RazorEdge, LP03-532RE-25 and LP02-266RS-25, respectively) before the entrance of the SHRS. In addition, short-pass filters for UV (Semrock BrightLine, FF01-300/SP-25) or band-pass filters for visible (Semrock BrightLine, FF01-558/20-25) were used to block longer wavelengths. The gratings were mounted in piezo motor driven optical mounts connected with a piezo motor controller (Newport, Model AG-UC8) and positioned on a precision rotation stage (Newport, Model URS75BPP) for setting the Littrow angle precisely to the desired wavelength. The interference fringe pattern was produced by imaging the gratings onto a thermo-electrically cooled, gated, 25 mm wide by 6.7 mm high, 1024 by 256 ICCD array detector, (Princeton Instruments, Model PIMAX 3), using a 105 mm focal length, f/4 fused silica lens (JENOPTIK CoastalOpt® 105 mm UV-Vis SLR lens). The imaging lens was placed approximately 245 mm from the gratings and ~185 mm from the detector to form a 15 mm square fringe image on the ICCD detector, with substantial clipping in the vertical direction. The ICCD gate width and delay time were adjusted at each measurement distance to maximize the Raman signal and reduce ambient light.

For most spectra three additional images were acquired for background corrections; two blocking each of the gratings separately and one blocking both gratings. The Fourier transform of the fringe images was performed using the Fast Fourier transform (FFT) function in Matlab. Each spectrum was apodized using a Hamming function to reduce ringing effects in the spectral baseline, though no studies were done to determine if this apodiztaion function was optimal. No flat field or instrument response corrections, smoothing, sharpening, or any other post-processing was used.

## 5.4 Result and Discussions

The working principle of the SHRS has been described in earlier papers.[24-26] As illustrated in Fig. 2, collected light is collimated and directed through the SHRS entrance aperture. A 50/50 beamsplitter divides the light into two coherent beams, directed to the diffraction gratings that are tilted at an angle, the Littrow angle $\Theta_L$, with respect to the grating normal. Heterodyning in the interferometer occurs at the Littrow wavenumber, $\Theta_L$, which corresponds to the wavelength of light that is exactly retro-reflected, back along the optical axis, and hence recombines at the beamsplitter without interference. For any wavenumber ($\sigma$) other than Littrow, the diffracted light leaves the gratings at an angle, resulting in crossed wavefronts in the beamsplitter, generating an interference pattern, which produces a series of wavelength dependent fringes on the array detector. The fringe frequency on the detector is given by Eq. 1, where *f* is in fringes/cm.[24, 27-29] According to Eq. 1, Raman bands above or below the Littrow wavenumber show identical fringe patterns and can lead to degenerate Raman bands. This is discussed in more detail below. The intensity, *I(x)*, of fringes obtained as a function of detector position, *x*, is given by Eq. 2, where B($\sigma$) is the input spectral intensity at wavenumber $\sigma$. The Fourier transform of *I(x)* yields the Raman spectrum.[24, 27-29]

$$f = 4\,(\sigma - \sigma_L)\,\tan\theta_L \tag{1}$$

$$I(x) = \int_0^\infty B(\sigma)[1 + \cos\{8\pi(\sigma - \sigma_L)\,x \tan\theta_L\}]\,d\sigma \tag{2}$$

Like all interferometers, it is important to block all wavelengths outside the spectral regions of interest. Shot noise is distributed equally at all wavelengths in an interferometer, so strong bands outside the spectral region of interest add noise at all wavelengths. Of particular concern is scattered laser light and strong fluorescence. Thus, the use of optical filters to limit the bandpass of the spectrometer is crucial in the SHRS. To prevent elastically scattered laser light entering the spectrometer two 532 nm or 266 nm laser-blocking filters (RazorEdge, Semrock) were employed before the entrance of the SHRS. In addition, short-pass or band-pass optical filters were used to block longer wavelengths.

The theoretical spectral bandpass of the SHRS is a function of the resolving power and the number of detector elements on the ICCD in the spectral direction. The resolving power is equal to the number of grooves illuminated, so in this case $R$=12,000, giving a theoretical resolution of ~3 $cm^{-1}$ for a 1000 $cm^{-1}$ Raman shift, using 266 nm excitation and ~1.5 $cm^{-1}$ using 532 nm excitation. The measured UV spectral resolution was previously determined to be 4.5 $cm^{-1}$ using a diamond sample.[24] Factors that affect the resolution include camera focusing, collimation of input beam, and quality of the gratings and imaging optics, with grating imperfections appearing to be the most important in our current setup. The ICCD used had 1024 spectral resolution elements and can thus be used to measure 512 wavelength elements, giving a theoretical ICCD-limited UV spectral range of ~1600 $cm^{-1}$. The maximum, resolution-limited solid angle field of view (FOV) of the SHRS is, $\Omega_{max} = 2\pi/R$ steradian.[27] Thus the solid angle FOV for this spectrometer is 5.2 x $10^{-4}$ sr, and the full acceptance angle is 1.3°.

Although UV excitation offers potential sensitivity advantages for standoff Raman, UV excitation is difficult to implement because strong sample absorption in the UV often leads to photodecomposition of the sample. For example, in these UV standoff studies, it was found that using the 266 nm laser, calcite was damaged by 23 mJ pulses but was not affected using 10 mJ pulses. Acetaminophen on the other hand was damaged at all laser energies tested. Lowering the laser power is effective at reducing sample decomposition; however, it also has the effect of reducing Raman signal. An alternative approach is to reduce the laser irradiance on the sample while keeping the laser power high, by increasing the size of the laser spot on the sample. In this case, the Raman signal is not reduced as long as the field of view of the spectrometer is at least as large as the laser spot on the sample. We demonstrated this in a previously published study by measuring a photosensitive compound, $NH_4NO_3$, using the SHRS with 244 nm excitation with a large laser spot on the sample.[24] Thus, in this standoff study, using 266 nm excitation, to avoid sample decomposition, the largest possible laser spot that could be viewed by the SHRS was used. As shown above, the full acceptance angle of the UV SHRS was ~1.3°. The magnification of the telescope at 18 m was about 5.3, corresponding to a ~37 mm diameter spot on the sample at 18 m standoff distance (note: the telescope at this range was effectively f/11). The laser spot size for all UV standoff Raman measurements was about 25 mm diameter, well within the FOV of the standoff spectrometer. It is interesting to compare the SHRS FOV to a hypothetical dispersive standoff spectrometer. The slit image of an f/6.7 dispersive spectrometer using a 100-micron wide input slit, f/# matched to the same telescope would be ~0.9 mm wide at 18 m, and the total area viewed at the sample would be ~1800 times smaller, assuming a circular field of view in each case, limited by the shape of the focused laser beam.

### 5.4.1 UV Wavelength Standoff Raman Measurements

Figure 3 shows standoff SHRS UV Raman spectra of several samples that were placed at a distance of 18 m from the telescope. The samples, $KClO_3$ (a), urea (b), calcite (c), and $KClO_4$ (d), were measured using 600, 10.3 mJ laser pulses (i.e., 60 s exposure time) with all laboratory lights on and using a 0.18 µs gate delay and 0.05 µs gate width. The SHRS was tuned to cover the spectral range 600-2000 $cm^{-1}$ (by setting Littrow at ~600 $cm^{-1}$) because this range contains the key spectral features of these samples. The prominent Raman bands of $KClO_3$ at 937 $cm^{-1}$ ($ClO_3^-$ vibrational mode), urea at 1013 $cm^{-1}$ (C-N vibrational mode), calcite at 1087 $cm^{-1}$ ($CO_3^-$ vibrational mode), and $KClO_4$ at 942 $cm^{-1}$ ($ClO_4^-$ vibrational mode), are clearly observed, free from any background ambient light, with a measured spectral resolution of ~10 $cm^{-1}$.

Figure 4 shows the standoff SHRS UV Raman spectrum of Teflon with the sample 18 meters from the telescope using 600, 10.3 mJ, 266 nm pulses (i.e., 60 s exposure time). Littrow was set to ~495 $cm^{-1}$ and all lab lights were on. The gate delay and gate width were 0.18 µs and 0.05 µs, respectively. The fringe image (top inset) and fringe image cross section (middle inset) are also shown in Fig. 4. The fringe visibility (FV) value is ~0.32, much less than the 1.0 theoretical value for monochromatic light. The reason for the low FV is poor UV transmission and optical imperfections in the beam splitter. Poor fringe visibility leads to increased noise in the SHRS spectra and is one of the current limitations of the UV SHRS. A possible improvement to this part of the system would be to use a plate beam splitter, since plate beam splitters are available with much better UV transmission and surface flatness than cube beam splitters.

The SHRS Teflon spectrum in Fig. 4 displays several characteristic Raman bands with no significant ambient light background. The sharp Raman band of Teflon at 734 $cm^{-1}$ corresponds to the F-C-F stretching mode, and the 1200-1400 $cm^{-1}$ spectral region shows bands for the F-C-F anti-symmetric stretching mode (1215 $cm^{-1}$) and C-C vibrational modes (~1296 $cm^{-1}$ and ~1378 $cm^{-1}$). The measured resolution of this band was 11 $cm^{-1}$, much larger than the ~4.5 $cm^{-1}$ spectral resolution of the SHRS as verified previously using a diamond sample.[24] For this measurement, the input beam was focused slightly so that more light hit the small ICCD (e.g., was less clipped vertically), leading to reduced resolution but higher sensitivity.

The Raman bands at ~ 576 $cm^{-1}$ are related to crystal defect structures.[30] The position of the Raman bands and the relative intensities shown in Fig. 4 are in qualitative agreement with published data,[16,31] even though no correction was made for the instrument response function. The two bands at ~611 and ~693 $cm^{-1}$ are likely the 291 $cm^{-1}$ (F-C-F twisting) and 387 $cm^{-1}$ (F-C-F bending) Teflon bands, respectively. As shown by Eq. 1, there is no discrimination between bands that are higher or lower than the Litrrow wavenumber. Heterodyning of Raman bands below the Littrow wavenumber can lead to low energy bands being shifted to higher energy spectral regions. This effect can be useful for extending the spectral range of the SHRS, or this degeneracy can be completely avoided by tilting one of the gratings in the vertical direction.[26]

### 5.4.2 Visible Wavelength Standoff Raman Measurements

Visible wavelength standoff SHRS measurements were made by simply adjusting the Littrow angle of the gratings to the visible wavelength range. Figure 5 shows the standoff Raman spectra of $NH_4NO_3$, $TiO_2$, and sulfur, acquired using the SHRS with a 532 nm, 20 Hz pulse rate laser, and a 96 mm aperture telescope. The spectra were recorded from various standoff distances in the range 3 to 14 m with the laser power from 60-106 mW using a 60 s exposure time. The laser spot size at the sample varied from 7 mm for the closest samples to 25 mm for the most distant samples.

Fig. 5(a) shows the Raman spectrum of $NH_4NO_3$ at a sample distance of 3 m using 62 mW laser power with a 7 mm laser spot size on the sample. Using a 7 mm laser spot, no sample decomposition was observed. The spectrum was obtained using the SHRS with a Littrow wavelength of 550 nm (700 $cm^{-1}$ Raman shift from the laser line) and using a 558 nm band pass filter to block lower frequency Raman signals. Ammonium nitrate is widely used as a precursor for explosives manufacture. Therefore, remote measurements of ammonium nitrate could be useful for explosives detection. The SHRS spectrum of ammonium nitrate shows a strong Raman band at 1040 $cm^{-1}$ due to the $NO_3^-$ symmetric stretching mode, the FWHM of which was 5.4 $cm^{-1}$. Figure 5(b) shows the Raman spectrum of $TiO_2$ measured with the sample 10 m from the telescope, using 103 mW laser power at the sample with the Littrow wavelength set to the laser wavelength (0 $cm^{-1}$ Raman shift). The laser spot size on the sample was ~20 mm, much smaller than the >45 mm field of view (0.27$^o$ FOV) of the SHRS at this distance, calculated assuming a collimated beam. The Raman spectrum of sulfur shown in Fig. 5(c) was measured with the sample at a standoff distance of 14 m using 106 mW laser power with Littrow set to 532 nm and using a 25 mm laser spot on the sample. Figure 5(c) also shows the sulfur fringe image (inset top) and the fringe image cross section (inset middle). The FV value of the fringe cross section is only 0.22, much less than the theoretical value of 1.0 for monochromatic light. The low FV value in this case is because the UV beamsplitter used had poor visible wavelength transmission. The main sulfur Raman bands in the spectrum are at 85 $cm^{-1}$, 154 $cm^{-1}$, 219 and 473 $cm^{-1}$. The relative intensity of the Raman band at 473 $cm^{-1}$ is lower than the band at 85 $cm^{-1}$ because of the decreasing response of SHRS in the higher frequency region.

### 5.4.3 UV Stability Study

An interferometer is susceptible to changes in the optical path length in the arms, usually caused by vibrations, and for this reason, interferometer-based spectrometers are commonly used on a vibration-isolation table. In the standoff SHRS studies described here, it was found that the SHRS was not highly susceptible to vibrational misalignment. Fig. 6 shows Raman spectra of diamond, which has a very sharp band at ~1333 $cm^{-1}$, measured using a 244 nm continuous wave laser, with and without vibration isolation (i.e., using a floating and non-floating optical table). The FV was 0.36 for all spectra. Also, the spectral position of the band and the FWHM are unchanged using short, 0.5 s, and long, 60 s exposures with or without vibration isolation, indicating no effect of system vibrations on the Raman spectrum over this measurement time. Figure 7 shows the results of a similar test using the standoff SHRS. The bandwidth and position of sulfur bands were measured using short, 1s, and long, 60s, exposures with the laser on a lab bench that was not vibration isolated. Figure 7 shows Raman spectra of sulfur measured by integrating 20 (1 s), 600 (30 s) and 1200 (60 s) laser pulses, respectively with the sample at a 10 meter standoff distance. The fringe visibility was the same, 0.25, and the FWHM of the 154 and 219 $cm^{-1}$ bands was 10-11 $cm^{-1}$, for all three exposures. The band positions were also the same within one pixel. This indicates vibrational stability of the standoff SHRS at this time scale.

## 5.5 Conclusions

The spatial heterodyne Raman spectrometer is well suited for both UV and visible standoff Raman measurements. The large aperture and wide acceptance angle of the SHRS simplifies optical coupling of the spectrometer to the telescope, and makes alignment of the laser on the sample very forgiving. The use of a pulsed laser and a gated detector allows SHRS measurements to be made in bright ambient light. The SHRS is sufficiently unaffected by system vibrations for the exposure times used, that a vibration isolated optical table was not necessary for the measurements described. Although signal to noise comparisons between the SHRS and dispersive Raman systems for standoff Raman were not part of this study, this was addressed recently in regard to FT Raman spectrometers.[32]

## 5.6 Acknowledgements

We would like to thank the National Science Foundation for supporting this work under grant CHE-1308211 and NASA for support under grant NNX14AI34G and NASA/SC Space Grant 21-NE-USC_Angel-RGP. We also thank the Research Corporation of the University of Hawaii (RCUH) /NAVSEA/DOD, for partial support of this work under contract number. ZA01339. This work has also benefited in part by the support from the Office of Naval Research under the grant #N00014-12-1-0087.

## 5.7 References

1. J.R. Ferraro, K. Nakamoto, C.W. Brown. “Industrial, Environmental and Other Applications”. In: F. K. Nakamoto C. W. Brown, editors. “Introductory Raman Spectroscopy”. San Diego: Academic Press, 2003. Pp. 325–361.

2. J. Cooney. "Satellite Observations Using Raman Component of Laser Backscatter". In: Ralph Zirkind editor. New York: Polytechnic Institute of Brooklyn Press, 1967. Pp. P1-P10.

3. D.A. Leonard. “Observation of Raman Scattering from the Atmosphere using a Pulsed Nitrogen Ultraviolet Laser”. Nature. 1967. 216(5111): 142–143.

4. T. Hirschfeld. “Range Independence of Signal in Variable Focus Remote Raman Spectrometry”. Appl. Opt. 1974. 13(6): 1435-1437.

5. R.M. Measures. Laser Remote Sensing: Fundamentals and Applications. New York: John Wiley & Sons, 1984.

6. S.M. Angel, T.J. Kulp, T.M. Vess. “Remote-Raman Spectroscopy at Intermediate Ranges Using Low-Power CW Lasers”. Appl. Spectrosc. 1992. 46(7): 1085–1091.

7. J.C. Carter, J. Scaffidi, S. Burnett, B. Vasser, S.K. Sharma, S.M. Angel. “Stand-off Raman Detection using Dispersive and Tunable Filter Based Systems”. Spectrochim. Acta. A. Mol. Biomol. Spectrosc. 2005. 61(10): 2288–2298.

8. J.C. Carter, S.M. Angel, M. Lawrence-Snyder, J. Scaffidi, R.E. Whipple, J.G. Reynolds. “Standoff Detection of High Explosive Materials at 50 Meters in Ambient Light Conditions Using a Small Raman Instrument”. Appl. Spectrosc. 2005. 59(6): 769–775.

9. R.L. Aggarwal, L.W. Farrar, D.L. Polla. “Measurement of the Absolute Raman Scattering Cross Sections of Sulfur and the Standoff Raman Detection of a 6 mm thick Sulfur Specimen at 1500 m”. J. Raman Spectrosc. 2011. 42(3): 461–464.

10. M. Gaft, L. Nagli. “UV Gated Raman Spectroscopy for Standoff Detection of Explosives”. Opt. Mater. 2008. 30(11): 1739–1746. doi:10.1016/j.optmat.2007.11.013.

11. J. Moros, J.A. Lorenzo, K. Novotný, J.J. Laserna. “Fundamentals of Stand-off Raman Scattering Spectroscopy for Explosive Fingerprinting”. J. Raman Spectrosc. 2013. 44(1): 121–130.

12. A. Pettersson, S. Wallin, H. Östmark, A. Ehlerding, I. Johansson, M. Nordberg, H. Ellis, A. Al-Khalili. “Explosives Standoff Detection using Raman spectroscopy: From Bulk Towards Trace Detection”.Proc. SCIE. 2010.76641K: 1–12.

13. P.G. Lucey, T.F. Cooney, S.K. Sharma. "A Remote Raman Analysis System for Planetary Landers". Paper presented at LPSC. 1998. Houston TX; March 16-20 1998.

14. Horton, K. A., N. Domergue-Schmidt, S. K. Sharma, P. Deb, and P. G. Lucey. "Remote Raman System for Planetary Landers: Data Reduction and Analysis". Paper presented at LPSC. 200. Houston TX; March 13-17 2000.

15. S.M. Angel, N.R. Gomer, S.K. Sharma, C. McKay. "Remote Raman Spectroscopy for Planetary Exploration: A Review". Appl. Spectrosc. 2012. 66(2): 137–150. 10.

16. M. Wu, M. Ray, K.H. Fung, M.W. Ruckman, D. Harder, A.J. Sedlacek. "Stand-off Detection of Chemicals by UV Raman Spectroscopy". Appl. Spectrosc. 2000. 54(6): 800-806.

17. M.D. Ray, A.J. Sedlacek, M. Wu. "Ultraviolet Mini-Raman Lidar for Stand-off, In Situ Identification of Chemical Surface Contaminants". Rev. Sci. Instrum. 2000. 71(9): 3485–3489.

18. M. Skulinova, C. Lefebvre, P. Sobron, E. Eshelman, M. Daly, J.-F. Gravel, J. F. Cormier, F.Châteauneuf, G. Slater, W. Zheng, A. Koujelev, R. Léveillé. "Time-resolved Stand-off UV-Raman Spectroscopy for Planetary Exploration". Planet. Space Sci. 2014. 92: 88–100.

19. T.J. Kulp, S.E. Bisson, T.A. Reichardt. "Standoff Ultraviolet Raman Scattering Detection of Trace Levels of Explosives". Sandia Natl. Lab. [Tech. Rep.] SAND. 2011.7955.

20. R.L. McCreery. "Magnitude of Raman Scattering". In: T.D. Winefordner editor. Raman Spectroscopy for Chemical Analysis. New York: John Wiley & Sons, Inc., 2000. Pp.15-33.

21. S.A. Asher. "UV Resonance Raman Spectroscopy for Analytical, Physical, and Biophysical Chemistry. Part 1". Anal. Chem. 1993. 65(2): 59A–66A.

22. M. Ghosh, L. Wang, S.A. Asher. "Deep-Ultraviolet Resonance Raman Excitation Profiles of $NH_4NO_3$, PETN, TNT, HMX, and RDX". Appl. Spectrosc. 2012. 66(9): 1013-1021.

23. S.A. Asher, C.R. Johnson. "Raman Spectroscopy of a Coal Liquid Shows that Fluorescence Interference is Minimized with Ultraviolet Excitation". Science. 1984. 225(4659): 311–313.

24. N. Lamsal, S.M. Angel. "Deep-Ultraviolet Raman Measurements Using a Spatial Heterodyne Raman Spectrometer (SHRS)". Appl. Spectrosc. 2015. 69(5): 525–534.

25. N. Lamsal, S.M. Angel, S.K. Sharma, T.E. Acosta. “Visible and UV Standoff Raman Measurements in Ambient Light Conditions Using a Gated Spatial Heterodyne Raman Spectrometer”. Paper presented at: LPSC 2015. Woodland TX, March 16-20.2015.

26. N.R. Gomer, C.M. Gordon, P. Lucey, S.K. Sharma, J.C. Carter, S.M. Angel. “Raman Spectroscopy Using a Spatial Heterodyne Spectrometer: Proof of Concept”. Appl Spectrosc. 2011. 65(8): 849–857.

27. J..M. Harlander. Spatial Heterodyne Spectroscopy: Interferometric Performance at any Wavelength Without Scanning. [Ph.D. Thesis]. Madison, Wisconsin: The University of Wisconsin, 1991.

28. J.M. Harlander, F.L. Roesler, S. Chakrabarti. ‘‘Spatial HeterodyneSpectroscopy: A Novel Interferometric Technique for the FUV’’. In: O.H.W. Siegmund, H.S. Hudson, editors. EUV, X-Ray, and Gamma-Ray Instrumentation for Astronomy. Proc. SPIE. 1990. 1344: 120-131.

29. J. Harlander, R. Reynolds, F. Roesler. “Spatial Heterodyne Spectroscopy for the Exploration of Diffuse Interstellar Emission-Lines at Far-Ultraviolet Wavelengths”. Astrophys. J. 1992. 396(2): 730–740.

30. D.I Bowers W. F. Maddams. “The Characterization of Polymers”. The Vibrational Spectroscopy of Polymers. Cambridge, UK: University Press, Cambridge, 1989. Pp. 185-190.

31. A.J. Sedlacek III, S.D. Christesen, T. Chyba, P. Ponsardin. ‘‘Application of UV-Raman Spectroscopy to the Detection of Chemical and Biological Threats’’. In: A.J. Sedlacek, R. Colton, T. Vo-Dinh, editors. Chemical and d Biological Point Sensors for Homeland Defense. Proc. SPIE. 2004. 5269: 23-33.

32. S. Dzsaber, M. Negyedi, B. Bernáth, B. Gyüre, T. Fehér, C. Kramberger, T. Pichlerband F. Simona, “A Fourier Transform Raman Spectrometer With Visible Laser Excitation,” J. Raman Spectrosc. 201 (5). 46: 327–332.

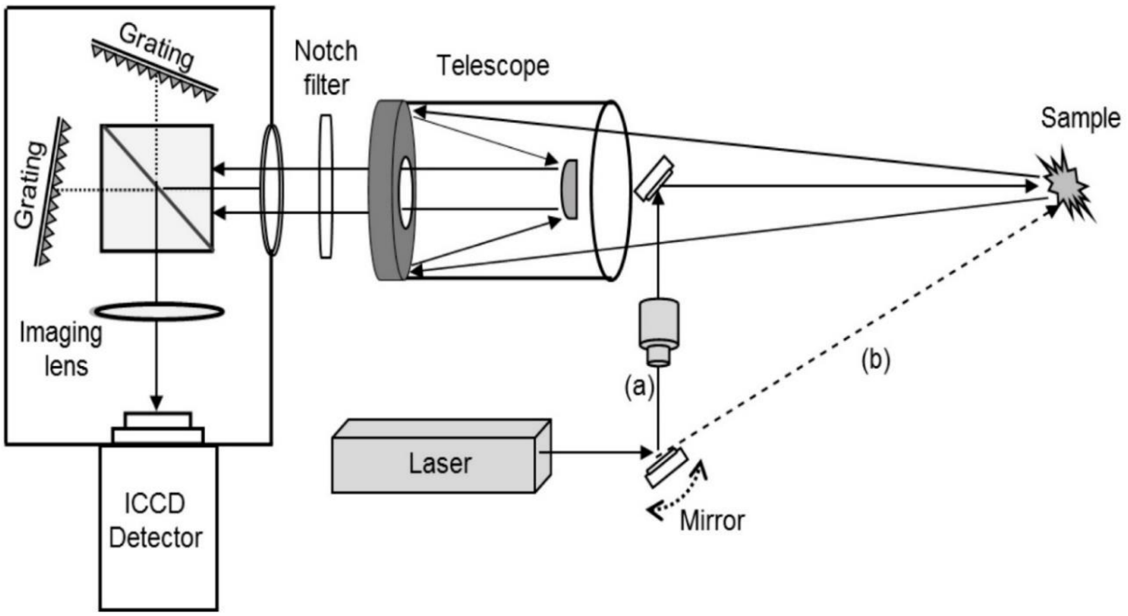

Figure 5.1. Schematic of standoff Raman system showing (a) co-axial and (b) oblique geometries for laser and telescope optical paths. The co-axial geometry was used for UV excitation and oblique geometry was used for visible excitation.

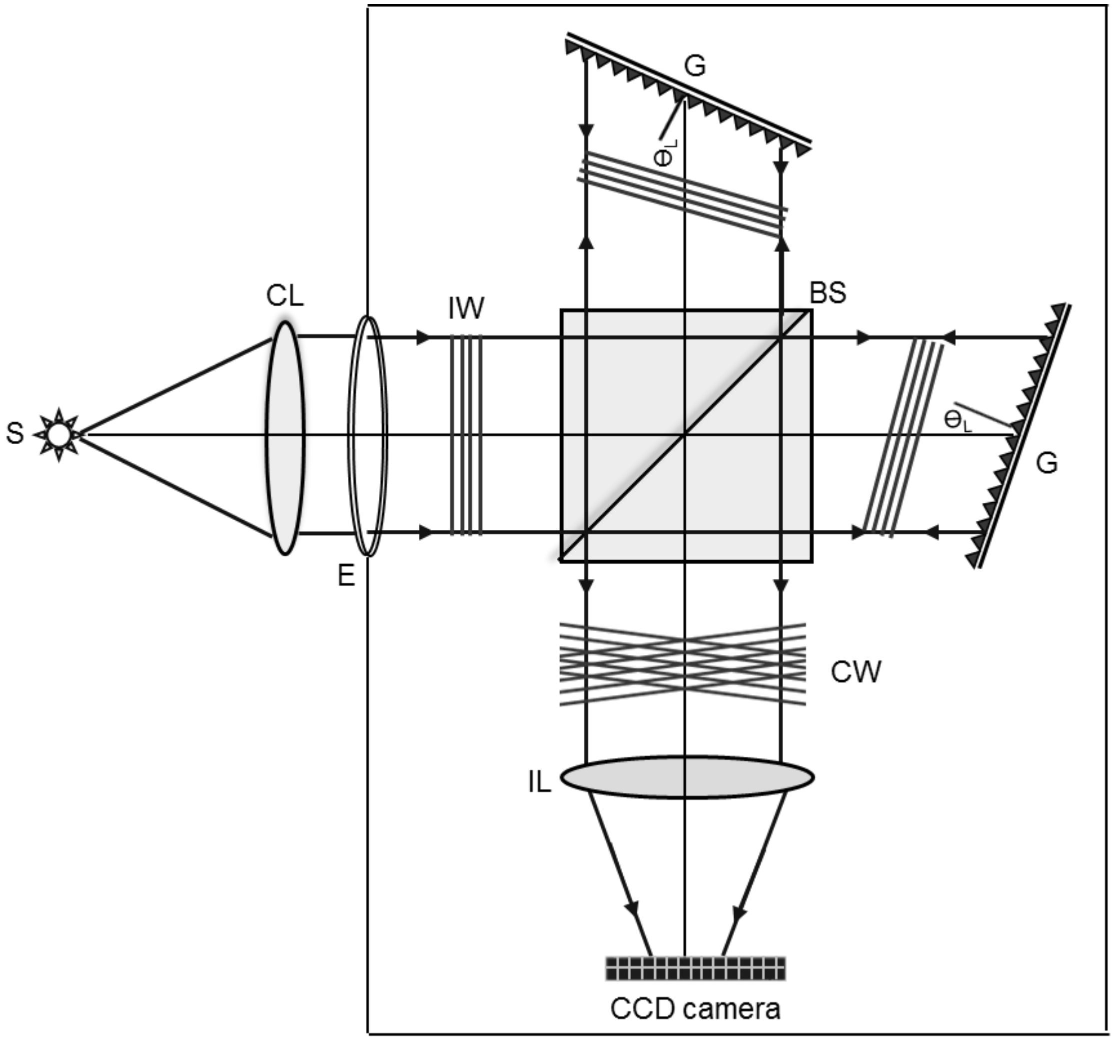

Figure 5.2 Detailed schematic showing the layout and illustrating the working principle of the SHRS. S= light source, CL= collection lens, E= entrance aperture, IW= input wavefront, BS= beamsplitter, G= diffraction grating, CW= crossed wavefront, IL=imaging lens, $\theta_L$= Littrow angle.

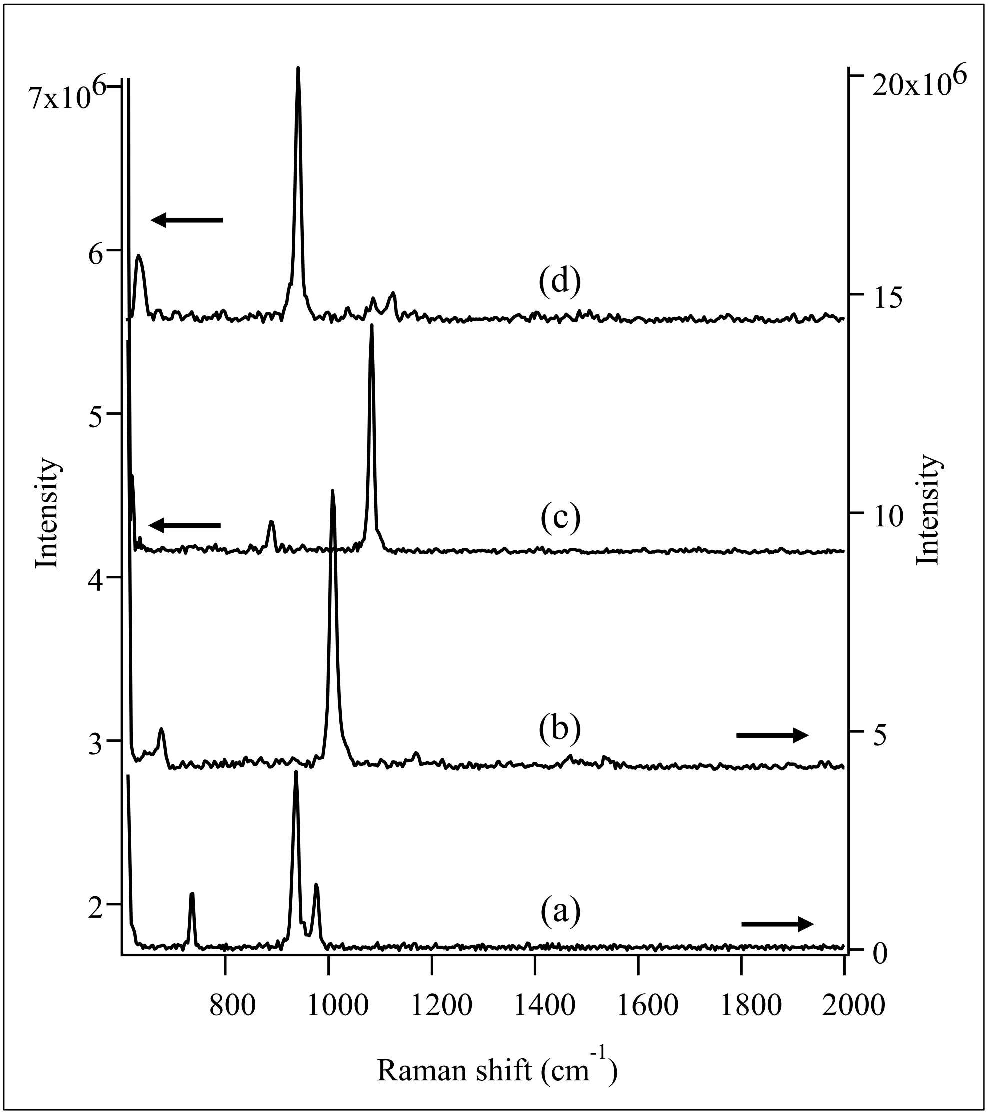

Figure 5.3. UV standoff Raman spectra of (a) potassium chlorate, $KClO_3$ (b) urea (c) calcite (d) potassium perchlorate, $KClO_4$ at ~18 m, measured using the SHRS spectrometer with Littrow set to ~600 cm$^{-1}$. The arrows above each spectrum refer to the appropriate intensity axis for that spectrum. Spectra were measured using 10.3 mJ/pulse, 10 Hz pulse rate, 266 nm excitation laser and a total integration time of 60 s. Spectra are offset vertically for clarity

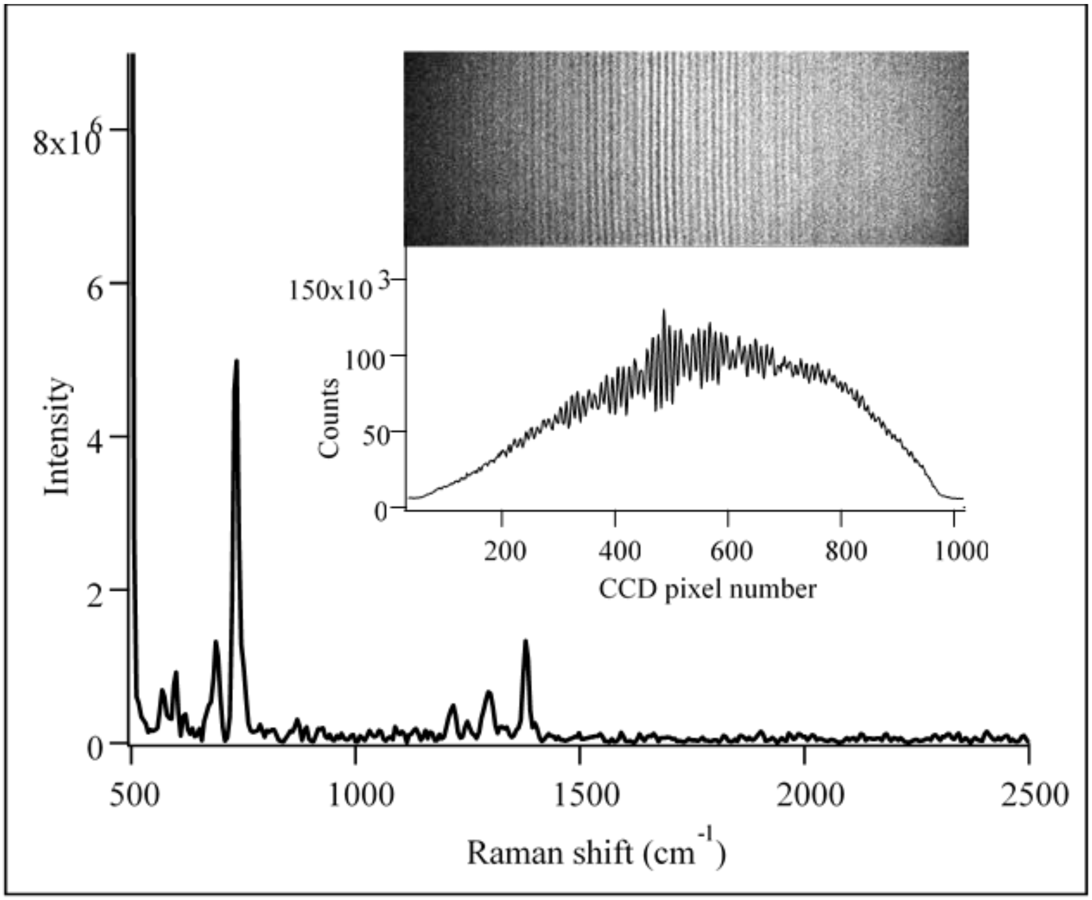

Figure 5.4. Teflon interferogram fringe image (top inset), intensity cross-section (middle inset) and Raman spectrum at ~18 m, obtained using the SHRS with Littrow set to ~500 cm$^{-1}$. The spectrum was measured using 10.3 mJ/pulse, 10 Hz pulse rate, 266 nm excitation laser and a total integration time of 60 s.

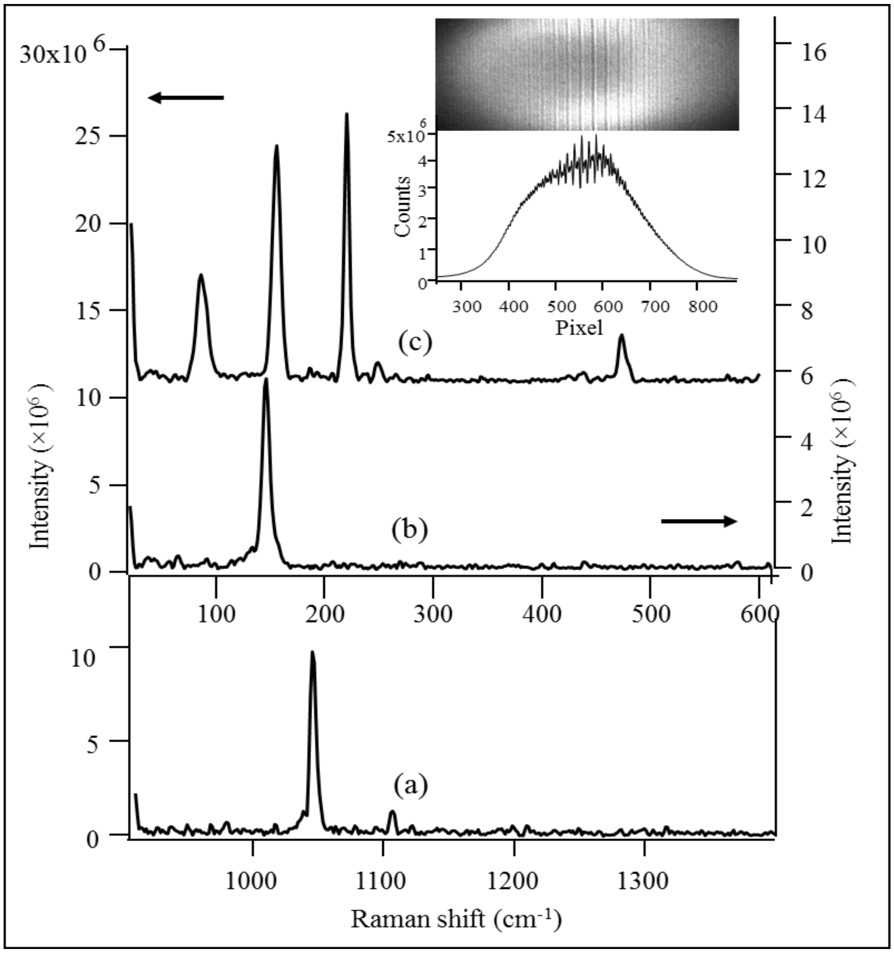

Figure 5.5. Visible standoff Raman spectra of (a) $NH_4NO_3$, (b) $TiO_2$ and (c) sulfur at 3, 10 and 14 m, respectively.The spectra were measured using 532 nm pulsed laser with 62, 103 and 106 mW laser power respectively and 60 s integration time. Littrow was different in each case. The inset shows the fringe image and cross section of sulfur. Spectra are offset vertically for clarity. The arrows above each spectrum refer to the appropriate intensity axis for that spectrum.

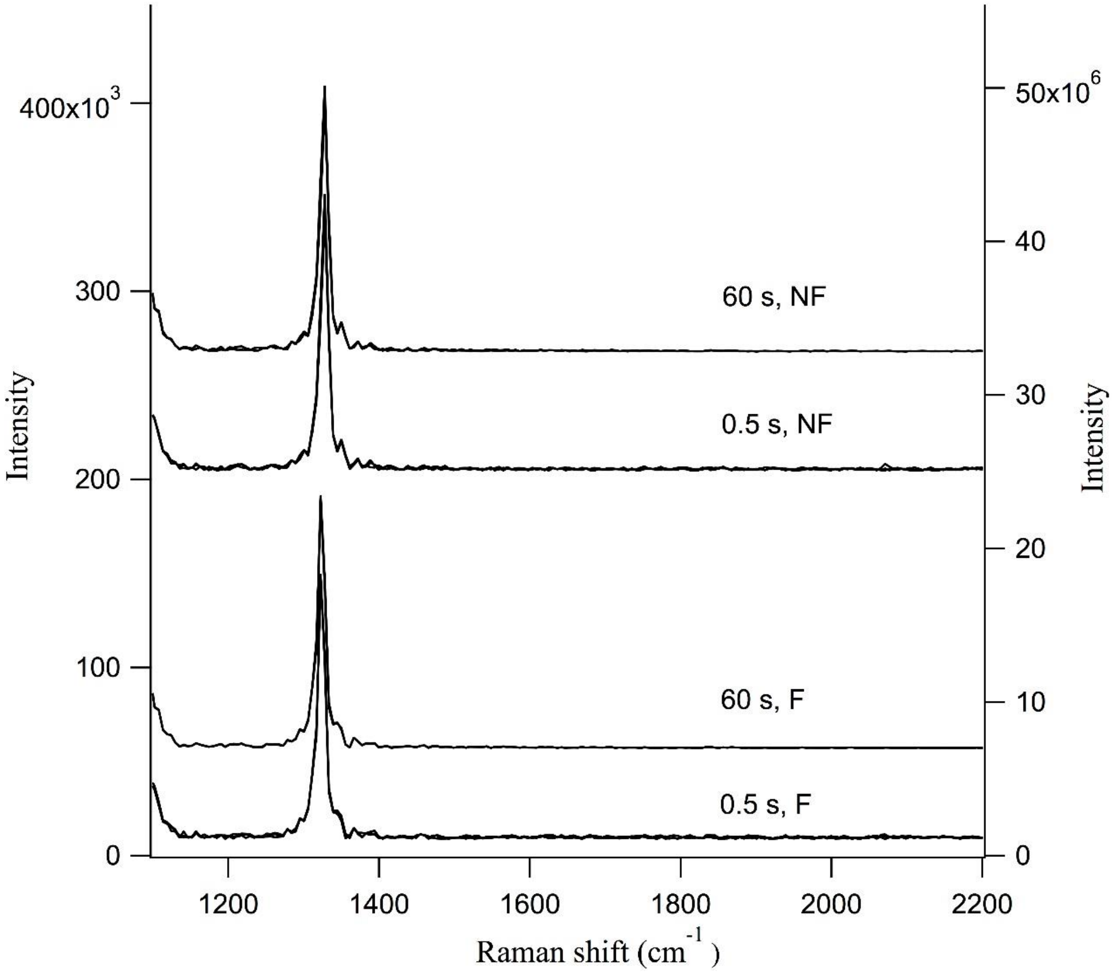

Figure 5.6 SHRS Raman spectra of diamond measured in triplicate, using 16 mW, 244 nm CW laser with 0.5 s and 60 s exposure times, with SHRS mounted on floating (F) and non-floating (NF) optical table. Twelve total spectra are shown in this plot. The triplicate measurements overlap to the extent that they cannot be discerned, indicating vibrational stability in the SHRS during the time required to make the measurements.

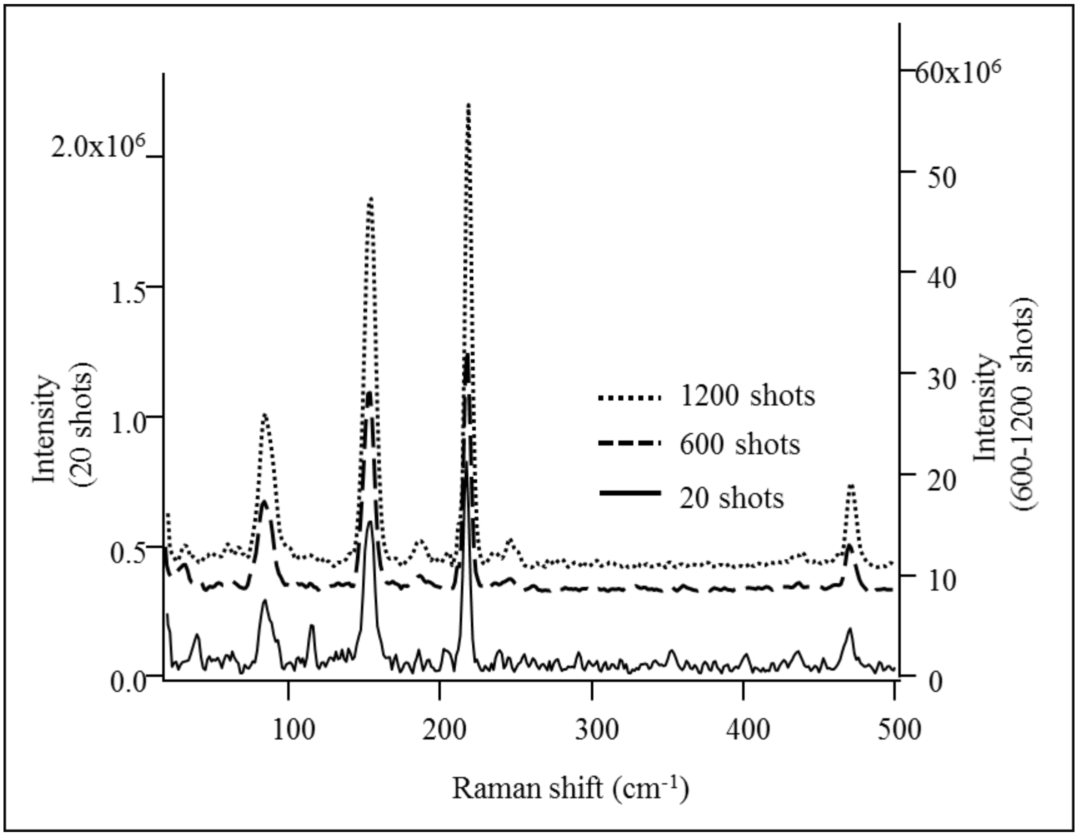

Figure 5.7 SHRS Raman spectra of sulfur at 10 m standoff distance recorded using 20, 60 and 1200, 532 nm laser pulses, 5.3 mJ/pulse and 20 Hz pulse rate with 9.6 cm diameter collection optics.

# Chapter 6

## Performance Assessment of a Plate Beamsplitter for Deep-UV Raman Measurements with a Spatial Heterodyne Raman Spectrometer[C]

### 6.1 Abstract

In earlier works, we demonstrated a high resolution Spatial Heterodyne Raman Spectrometer (SHRS) for deep UV Raman measurements, and showed its ability to measure UV light sensitive compounds using a large laser spot size. We recently modified the SHRS by replacing the cube beamsplitter with a custom-built plate beamsplitter with higher light transmission, higher surface flatness and better refractive index homogeneity than the cube beamsplitter. UV Raman measurements were performed using the modified SHRS and compared to the previous setup. The Raman spectra obtained using the modified SHRS exhibits much higher signal to noise ratio and show fewer spectral artifacts. In this paper, we discuss the new spectrometer design features, the advantages over previous designs and, and discusses some general SHRS issues such as spectral bandwidth, signal to noise ratio characteristics and optical efficiency.

---

[C] N. Lamsal, S. M. Angel. "Performance Assessment of a Plate Beamsplitter for Deep-UV Raman Measurements with a Spatial Heterodyne Raman Spectrometer". Appl. Spectrosc., to be submitted, March.2016.

## 6.2 Introduction

Recently, we developed a new type of Fourier transform (FT) Raman spectrometer; the spatial heterodyne Raman spectrometer (SHRS)[1,2] which addresses many of the issues related to conventional UV Raman spectrometers for planetary and other applications in extreme environments. The SHRS uses an interferometer with stationary diffraction gratings that utilizes a two-dimensional array detector such as a CCD or ICCD to record the interferogram, the design of which was first introduced by Harlander[3,4] for astronomical remote sensing measurements; later modified by Gomer et al for Raman measurements.[5] The SHRS system is small and lightweight, contains no moving parts, and offers the high resolution and wide spectral range needed for deep-UV Raman measurements. Additionally, the absence of entrance slit and the large field of view relieves the necessity to focus the energetic laser onto a sample, thus helps to avoid sample damage. The SHRS is compatible with pulsed lasers and gated detectors allowing the standoff measurements in ambient light conditions. All these characteristics together make the SHRS potentially suitable for planetary exploration such as for Mars missions.

In recent study, we demonstrated the potential of SHRS for deep-UV Raman measurements by collecting the Raman spectra of several solid and liquid samples using SHRS with 4.5 $cm^{-1}$ resolution and ~2600 $cm^{-1}$ bandpass, using a 244 nm excitation laser.[1] We also showed the importance of the wide acceptance angle in reducing the laser induced damage with defocused laser.[1,2] However, the design was not optimal because of likely due to poor optical efficiency, and low fringe visibility caused by the imperfections in the optical components especially the beamsplitter.

In this paper, we report an improved UV SHRS that uses cube beamsplitter by a narrow-band, high-grade plate beamsplitter specifically designed for UV applications. The plate beamsplitter addresses two major issues with the previously described UV SHRS, high optical losses and poor fringe visibility. In this paper, we discuss the performance of the modified UV SHRS with regard to fringe visibility, SNR and instrument response and issues with the SHRS design and instrument response.

## 6.3 Experimental

A schematic of the SHRS for UV Raman measurements is shown in Fig. 1. The spectrometer design follows the one described in previous studies,[1,2] but modified for deep-UV applications by including a high precision plate beamsplitter, designed to operate in the UV range. The SHRS interferometer consists of a pair of one inch, 300 grooves/mm square diffraction gratings blazed for 300 nm, and a 6.25 mm thick, 25.4 mm fused silica plate beamsplitter with Reflectance/Transmission ratio (R/T) of 50/50 (±5) in the range 240-300 nm. A compensator plate with exactly the same material and same dimension as that of the beamsplitter was introduced in the arm reflection in order to equalize the path length for each arms of the interferometer. The front and back surfaces of both the beamsplitter and the compensator are vacuum UV polished with a scratch/dig specification of 10/05. The transmitted wavefront error through each optic is less than λ/10 in the 240-300 nm range or λ/25 at 633 nm, and each optic is provided with a broadband antireflection coating. The gratings were mounted in piezo motor-driven optical mounts (Newport Model AGUC8) with a piezo motor controller and positioned on a precision rotation stepper (Newport URS75BPP Model) for setting the angle precisely to the desired Littrow wavelength. The diffraction gratings were imaged onto a thermo-electrically cooled back-illuminated UV-enhanced 2048×512, 13.5 μm pixels charge-coupled detector (CCD) (Princeton Instruments, Model PIXIS-2048 2KBUV;) using a 105 mm focal length, f/4.5 fused silica achromatic camera lens (JENOPTIK CoastalOpt 105 mm UV visible [Vis] single-lens reflex [SLR] lens;). The imaging lens (IL in Fig. 1) was placed approximately 210 mm (~2 focal lengths) from the gratings and 210 mm from the detector, magnification~ 1, to form a the interferogram image on the 6.9 mm high CCD. After recording an interferogram, the interferogram image on the CCD is binned to produce a single-channel interferogram cross section for each of the 2048 columns of pixels, which is then Fourier transformed to recover the power (i.e., intensity) spectrum.

A CW 244 nm intracavity frequency-doubled Ar-ion laser (95 SHG model; Lexel), was used for excitation with an average power up to 15 mw on the sample. The laser beam was directed onto the sample using two $45^{o}$ laser line dielectric mirrors with reflectivity higher than 98% over the 244–257 nm range, to clean up the 244 nm line from the 488 nm fundamental laser line. The laser was focused onto the sample using a 75 mm focal-length quartz lens mounted on a translational microstage to allow changing the size of the laser spot on the sample. Liquid samples were placed in a 1 cm quartz cuvette, centered on the focus of both the collection lens and the laser focus. Solid samples, either ground and packed in quartz cuvettes or pressed into pellets, were illuminated in the same way but were mounted on an x,y stage for front-surface illumination. Scattered light from the sample was collected using either a 50 mm or 75 mm focal length AR-coated quartz lens, with the laser incident on the sample at $150^{o}$ with respect to the optical axis of the collection lens. To help reduce fluorescence, collimated light was guided into the interferometer by two high performance dielectric mirrors placed in a $90^{o}$ arrangement. These mirrors have reflectivity over 95% in the wavelength range 244-266 nm, which is equivalent to a Raman range of 0-3400 cm$^{-1}$ using 244 nm excitation. In order to avoid overfilling of light on the 25.4 mm beamsplitter tilted at 45°, the input beam size was reduced to 13 mm by using several irises in the beam path before entering into the spectrometer. A long pass filter (Semrock, 229/244 nm stopline dual-notch filter) with OD >4 (at 244 nm) was used to block scattered laser light.

The interferometer Littrow wavelength (i.e., grating angles) was set using either the laser line, narrow lines from a low-pressure mercury lamp, or a narrow Raman band. CCD fringe images were recorded using Princeton Instruments Light Field software provided with the detector. Apart from the fringe image, three other images were acquired for each spectrum; two by blocking each of the gratings separately and one by blocking both gratings simultaneously. These additional images were sometimes used for background corrections of the fringe images. Fourier transforms of the fringe images were performed using the fast Fourier transform (FFT) function in Matlab. Each spectrum was apodized using a Hamming function to reduce ringing effects in the spectral baseline. We examined several other apodizing functions including Hanning, Gaussian, Blackman and Blackman-Harris, but found the Hamming function to be best for retaining the resolution and SNR of the recovered spectrum. The Raman spectra were calibrated by locating the position of known Raman bands and using a polynomial fit. No flat field or instrument efficiency corrections, phase correction, smoothing, sharpening, or any other post-processing such as zero filling was used for any of the data presented in this paper.

## 6.4 Results and Discussions

### 6.4.1 Working Principle of the SHRS

During SHRS measurements, the scattered Raman light is collected, collimated and passed through the entrance aperture and divided into two coherent beams by the 50/50 fused silica plate beamsplitter. The two beams are then diffracted by the diffraction gratings at an angle that depends on the wavelength as:

$$n\,\lambda = d(sin\alpha + sin\beta) \qquad (1)$$

Where n is diffraction order, λ is the wavelength of interest, d is diffraction grating groove density, and α and β are the angles of incidence and diffraction. Heterodyning in the interferometer is achieved by setting the grating angles in such a way that the light at wavelength ($\lambda_L$) or wavenumber ($\sigma_L$) is exactly retroreflected back along the same beam path. For 1st order diffraction,

$$\Theta_L = sin^{-1}(\lambda/2d) \qquad (2)$$

Light at this wavelength, knows as the Littrow wavelength or wavenumber ($\sigma_L$), recombines at the beamsplitter without producing an interference pattern. However, for any wavenumber other than Littrow, the diffracted beams leave the gratings at an angle, resulting in crossed wavefronts, generating an interference pattern, which produces a series of wavelength dependent fringes on the detector. The number of fringes produced on the detector is given by Eqn. 3, where $f$ is in fringes/cm.[4,6,7] The intensity of fringes obtained as a function of detector position, $x$, is given by Eqn. 4,[4,6,7] where $B(\sigma)$ is the input spectral intensity at wave number σ. The Fourier transform of $I(x)$ yields the Raman spectrum:

$$f = 4\,(\sigma - \sigma_L)\tan\theta_L \qquad (3)$$

$$I(x) = \int_0^{\infty} B(\sigma)[1 + \cos\{8\pi(\sigma - \sigma_L)\, x \tan\theta_L\}]\, d\sigma \qquad (4)$$

### 6.4.2 The performance of the SHRS with a plate beamsplitter

Figure 2 shows the UV Raman spectrum of diamond along with the interferogram fringe image (top inset) and the image cross section (bottom inset) measured with the modified SHRS system. The Littrow was set to approximately 1050 cm$^{-1}$ in order to observe the band at 1332 cm$^{-1}$. Similarly, Fig. 3 shows the UV Raman spectrum of $Na_2SO_4$ and its interferogram cross section that was measured using modified SHRS with the Littrow wavenumber at 550 cm$^{-1}$.The high quality interferogram image and the image cross sections are evident from Fig. 2 and 3. The quality of interferograms are far better than that were measured using the UV SHRS previously described. with a cube beamsplitter.[1] A measurement of the quality of the interferogram is the fringe visibility (FV):[8]

$$FV = \frac{I_{max} - I_{min}}{I_{max} + I_{min}} \qquad (5)$$

where, $I_{max}$ and $I_{min}$ are the maximum and minimum intensity in the interference fringe pattern. A FV value of one represents the ideal condition, which means all coherent light interferes to yield a fringe pattern. The diamond and $Na_2SO_4$interferogram shown in Fig 2 and 3 exhibits the FV of a ~0.6 0 and 0.53 respectively, which implies that in the SHRS more than half of the input light that reaches the detector is modulated to form the fringe pattern. Note that the FV of 0.6 is higher than typical FV values reported in the literature for visible FT-Raman spectroscopy.[9,10] FV values up to 0.8 are common for IR interferomters,[9] but this is difficult to achieve in the UV because of the more stringent requirements of optical qualities for UV optics.

### 6.4.3 Raman measurements of rocks and minerals

Figure.4 shows UV SHRS Raman spectra of some rock samples and a sea snail shell along with their pictures in the inset. The measurements were performed in their natural state without pre-cleaning or any other sample treatment. The samples fluoresce in the visible. For these spectra, 254 nm bandpass or 300 short pass filters were used to avoid fluorescence in the UV Raman spectra. The Raman spectra of gypsum, quartz and calcite exhibit strong bands at 1005, 457 and 1080 $cm^{-1}$ indicative of minerals containing $SO_4^{2-}$, O-Si-O and $CO_3^{2-}$ respectively. The Raman spectrum of the snail shell shows a strong calcite band at 1085 $cm^{-1}$ as the major constituent of the shell is calcium carbonate. Few weak spurious bands, mainly in the quartz spectrum are from the plasma line leaking from laser tubes. For each sample measurement, we measured blank in order to identify the plasma lines, labeled with * are laser plasma lines.

### 6.4.4 Performance comparison with a previous design

Figure 5 shows the Teflon UV Raman spectra measured using both the plate and cube beamsplitter SHRS systems with the same experimental conditions. We also maintained a similar laser spot size on the sample, and the collection optics and the geometry of collection were the same for both measurements. The only major difference between the two measurements is the size of the input beam. A 20 mm diameter collimated light input was used in the cube beamsplitter measurement, while for the plate beamsplitter measurements, we limited the input beam to approximately 13 mm diameter using irises in order to avoid the overfilling the 45 degree tilted 1-inch diameter plate beamsplitter. For 6.9 mm high CCD detector used, this means that about 40% of light is lost in the new design because of the smaller input beam diameter. Since, the smaller beam diameter illuminates fewer grooves on the gratings; the modified SHRS design has lower resolving power. Consequently, the Raman bands appear relatively broader in the spectrum measured using the new SHRS design.

A quantitative comparison reveals that the higher intensity or SNR for Raman peak obtained with a new design than the old design for measurements performed in the same experimental conditions, even though the theoretical calculation shows the loss of 40% of light for the new design due to smaller input beam. For example, we observed SNR of 250 and 1157 for the Raman peak at 734 cm$^{-1}$ for old and new SHRS designs respectively. This means that a new design outperforms the old design by almost five times, in spite of the fact that the old design measured with 40% more light. In the Teflon spectrum obtained with a new SHRS design (Fig.5A), 1378 cm$^{-1}$ band is almost 30% higher relative to the 734 cm$^{-1}$ band because the improved fringe visibility for Fig.5A leads to less error in the intensity of higher frequency bands.

One of the reasons for the improvement in the SNR using the plate beamsplitter is the better quality of the interferogram. This is apparent from Fig 5(C) and (D), which compares the fringe image and the image cross section of the Teflon Raman spectra shown in Fig. 5(A) and (B) respectively. The interferogram image recorded with a plate beamsplitter (Top) has higher contrast, with FV of 0.23, compared to FV of 0.07 for the cube beamsplitter, even though both spectra were recorded in similar experimental conditions. A primary reason for the FV improvement is a higher surface flatness (λ/25 at

632 nm), better refractive index homogeneity, and minimum surface defects, all of which minimize optical aberrations and wavefront distortion. In the earlier SHRS design, the cube beamsplitter used had a surface flatness less than ~ λ/4 at 250 nm. UV cube beamsplitters with higher surface flatness tolerance and low wavefront distortion are difficult to find.

Since the quality of the SHRS Raman spectra largely depends on the interference fringe visibility, it is worth studying the relationship between the fringe visibility and the SNR of the intensity spectrum. We established this relationship by comparing the SNR of Raman spectra measured as the interferogram FV was intentionally varied, by deliberately offsetting the SHRS arm lengths, by moving one of the gratings from the zero path-difference position. When the path length difference exceeds the coherence length of the input light, phase relations between rays from the two arms become random, yielding lower fringe visibility. Figure 6 depicts one such plot that relates the SHRS fringe visibility and SNR of the resulting Raman spectrum. The experiment was performed using $Na_2SO_4$, which has a single strong band at 993 $cm^{-1}$ and few weaker bands capable to yield high FV interferogram but not too narrow, therefore very sensitive to the interferometer path length difference. As expected, the, the SNR declines with the decreasing FV. It is worth noting that that the plot shows a linear relationship between the interferogram fringe visibility and the SNR of the reconstructed spectrum. This validates the importance of using high quality beamsplitter (i.e., the one that introduces less wavefront distortion) to obtain Raman spectrum with the highest possible SNR.

The beamsplitter is a crucial component of an interferometer, any losses in it also results into the poor sensitivity and poor SNR. The ability of the beamsplitter to transmit and reflect the input light intensity determines the efficiency (η) of the beamsplitter as shown in equation 6,

$$\eta = 4R_\lambda T_\lambda \qquad (6)$$

where, $T_\lambda$ and $R_\lambda$ are the transmission and reflection coefficients of the beamsplitter at wavelength λ. Equation (6) infers that η =1 only when, $T_\lambda = R_\lambda = 0.5$. An uneven ratio of transmission to reflectance decreases the efficiency of the beamsplitter leading to less light throughput and thus lower Raman intensity. Therefore, low quality beamsplitter decreases the SNR of SHRS spectrum. Unfortunately, the cement used for binding the prisms to make cube beamsplitter tends to absorb UV light strongly. The cube beamsplitter used in earlier system has $T_\lambda = R_\lambda \sim 30/30$ +/-5% (in the range 200-400 nm) yielding an efficiency of approx. ~0.3. The plate beamsplitter specifically designed for the new SHRS system has $T_\lambda = R_\lambda \sim 50$ ($\underline{+}$5 %), in the wavelength range of 240-300 nm, and therefore has a much higher optical efficiency, approx. 1.0, which significantly lowers the optical losses. This is the reason that the Raman band intensity recorded with the plate beamsplitter is always high even with less light throughput compared to the old system. For example, Teflon 734 $\text{cm}^{-1}$ band intensity measured with a new SHRS is almost 4 times higher than the 734 $\text{cm}^{-1}$ measured using old design in same experimental conditions (Fig. 4A and 4B).

In addition to the SNR improvement, the ability to produce evenly spaced, straight fringes on the CCD produces a more accurate, artifact free spectrum. This is illustrated in Fig. 7, which compares acetonitrile Raman spectra measured using the old (B) and new (A) SHRS designs. Using the plate beamsplitter (with FV 0.17), the major Raman bands at ~ 920, 2263 and 2943 $\text{cm}^{-1}$, and a small peak at ~2750 $\text{cm}^{-1}$ are clearly visible without any spurious bands. The spectrum measured with the older SHRS design (with FV 0.07) exhibits artifacts in the form of sidebands, and the weak band around 2263 cm$^{-1}$ is buried in the baseline noise. Sidebands can result from fringes that are not straight resulting from vertical aberration. This is mainly observed for high frequencies.

The bands located further from Littrow wavenumber are more vulnerable to optical aberrations than bands close to Littrow as they yield closely spaced high frequency lines. Figure 8 shows the Raman spectra generated from the top, middle and bottom sections of the interferogram image for each system. Considerable variations in the band intensity, bandwidth are observed among the three spectra measured with earlier SHRS design, which was expected, as the low-grade cube beamsplitter introduces optical aberrations, which reduce the fringe quality, such as straightness and spacing, which must be preserved to a few microns over the entire CCD chip. The weak spectral feature and the high frequency peak at the 2250 cm$^{-1}$ and the peak 2943 cm$^{-1}$ are much affected. In contrast, spectra obtained from different sections of the interferogram image with the SHRS incorporating a plate beamsplitter are nearly identical with similar intensities and without any serious band artifacts. This demonstrates that the incorporation of high quality plate beamsplitter not only help to elevate the SNR, but also reduces the inaccuracies in the SHRS Raman spectra. It is worth mentioning that the fringe defects or wavefront distortion can be corrected to some extent using image correcting software.[8–10] However, such software corrections may result in poor SNR and are limited to narrow spectral range measurements,[7] and are not applicable to broad spectral range measurements such as the Raman measurements of acetonitrile mentioned here.

The difficulty in imaging high frequency lines onto the CCD implies the need of blocking the higher frequency Raman bands, especially those further from Littrow position (even within the bandpass), to retain the quality of Fourier recovered spectra. The inability to accurately image the higher frequency Raman bands may lead to increase in the background and thus decrease the SNR of the system. The possible effect of high frequency bands on the spectrum SNR is illustrated in Fig.9, which compares the Raman spectra of cyclohexane and their interferogram cross sections measured in two different spectral range. Figure 9 (top) shows the spectrum over the wide spectral range from 700 to 3000 cm$^{-1}$ and Fig. 9 (bottom) shown the spectrum in the narrow spectral range from 700 to 1800 cm$^{-1}$ measured setting Littrow at 700 cm$^{-1}$.

It seems that measurements performed over the limited spectral range by blocking the bands far from Littrow wavenumber, those at around 2900 cm$^{-1}$, have a huge advantage on the sensitivity of the system. For example, the SNR of 803 cm$^{-1}$ peak is found to be more than two times higher for the spectrum acquired over narrow spectral coverage with band pass filter. The removal of high frequency band has been shown to be so effective that even the 803 cm$^{-1}$ band intensity drops by a factor of two due to the low transmission profile of a bandpass filter, the overall SNR increased more than two times because the background noise decreases by a factor of 5, see Fig. 9 for details. Note that the increase in the SNR is much higher than expected from decrease in the multiplex noise due to elimination of higher order bands. The calculation based on the number of photons indicates that the background noise should decrease by only a factor of two as opposed to a factor of 5. This is further verified by the quality of interferograms as shown in the inset of Fig. 9, which shows the FV of 0.26 for the cyclohexane measured with limiting bandpass as compared to FV of 0.08 for cyclohexane measured without bandpass filter. Therefore, proper filtering is necessary not only to avoid fluorescence, but also to suppress higher wavenumber bands to which the system responds poorly.

### 6.5 Conclusions

An improved deep-UV SHRS Raman spectrometer based on the use of a plate beamsplitter has been demonstrated, and addresses two major issues in the previously described deep UV SHRS spectrometer i.e. large optical losses and poor fringe visibility. The plate beamsplitter has higher transmission and surface flatness with higher transmission. The new system outperforms the old design by more than a factor of 5 in terms of SNR and by factor of 3 in terms of fringe visibility. In this study, we established that the SNR in the SHRS is a linear function of FV, and demonstrated how improved FV of the interferogram helps to minimize high frequency artifacts in the spectrum.

### 6.6 Acknowledgements

We would like to thank the NSF (grant number, CHE-1308211) NASA (grant number, NNX14AI34G) and NASA/SC (Space Grant 21-NE-USC_Angel-RGP) for supporting this work. We also thank the Research Corporation of the University of Hawaii (RCUH) /NAVSEA/DOD, for partial support of this work under contract No. ZA01339.

## 6.7 References

1. N. Lamsal, S.M. Angel. “Deep-Ultraviolet Raman Measurements Using a Spatial Heterodyne Raman Spectrometer (SHRS)”. Appl. Spectrosc. 2015. 69(5): 525–534.

2. N. Lamsal, S.M. Angel, S.K. Sharma, T.E. Acosta. “Visible and UV Standoff Raman Measurements in Ambient Light Conditions Using a Gated Spatial Heterodyne Raman Spectrometer”. Lunar and Planetary Science Conference. 2015. P. Abstract# 1459.3.

3. J.M. Harlander. Spatial Heterodyne Spectroscopy: Interferometric Performance at any Wavelength Without Scanning. [Ph.D. Thesis]. Madison, Wisconsin: The University of Wisconsin, 1991.

4. J. Harlander, R.J. Reynolds, F.L. Roesler. “Spatial heterodyne spectroscopy for the exploration of diffuse interstellar emission lines at far-ultraviolet wavelengths”. Astrophys. J. 1992. 396: 730. 10.1086/171756.

5. N.R. Gomer, C.M. Gordon, P. Lucey, S.K. Sharma, J.C. Carter, S.M. Angel. “Raman Spectroscopy Using a Spatial Heterodyne Spectrometer: Proof of Concept”. Appl. Spectrosc. 2011. 65(8): 849–857.

6. J.M. Harlander, F.L. Roesler, S. Chakrabarti. Spatial heterodyne spectroscopy: a novel interferometric technique for the FUV. 1990. Pp. 120–131.

7. J.E. Lawler, Z.E. Labby, J.M. Harlander, F.L. Roesler. “Broadband, high-resolution spatial heterodyne spectrometer”. Appl. Opt. 2008. 47(34): 6371.

8. P. Hariharan. “Basics of Interferometry”. Boston: Elsevier Academic Press, 2007. Pp. 6–7.

9. S. Dzsaber, M. Negyedi, B. Bernáth, B. Gyüre, T. Fehér, C. Kramberger, et al. “A Fourier transform Raman spectrometer with visible laser excitation: Fourier transform Raman spectrometer”. J. Raman Spectrosc. 2015. 46(3): 327–332.

10. R. Savoie, P. Beauchesne, D. Lévesque. “Fourier transform Raman spectroscopy in the visible region”. Microchim. Acta. 1988. 95(1-6): 223–225. 10.1007/BF01349757.

11. M.L. Forman, W.H. Steel, G.A. Vanasse. “Correction of Asymmetric Interferograms Obtained in Fourier Spectroscopy”. J. Opt. Soc. Am. 1966. 56(1): 59.

12. C.R. Englert, J.M. Harlander, J.G. Cardon, F.L. Roesler. “Correction of Phase Distortion in Spatial Heterodyne Spectroscopy”. Appl. Opt. 2004. 43(36): 6680.

13. .M. Harlander, H. Tran, F.L. Roesler, K.P. Jaehnig, S.M. Seo, W.T. Sanders III, Field-Widened Spatial Heterodyne Spectroscopy - Correcting For Optical Defects And New

Vacuum-Ultraviolet Performance Tests. In: O.H.W. Siegmund, J.V. Vallerga, editors. 1994. Pp. 310–319.

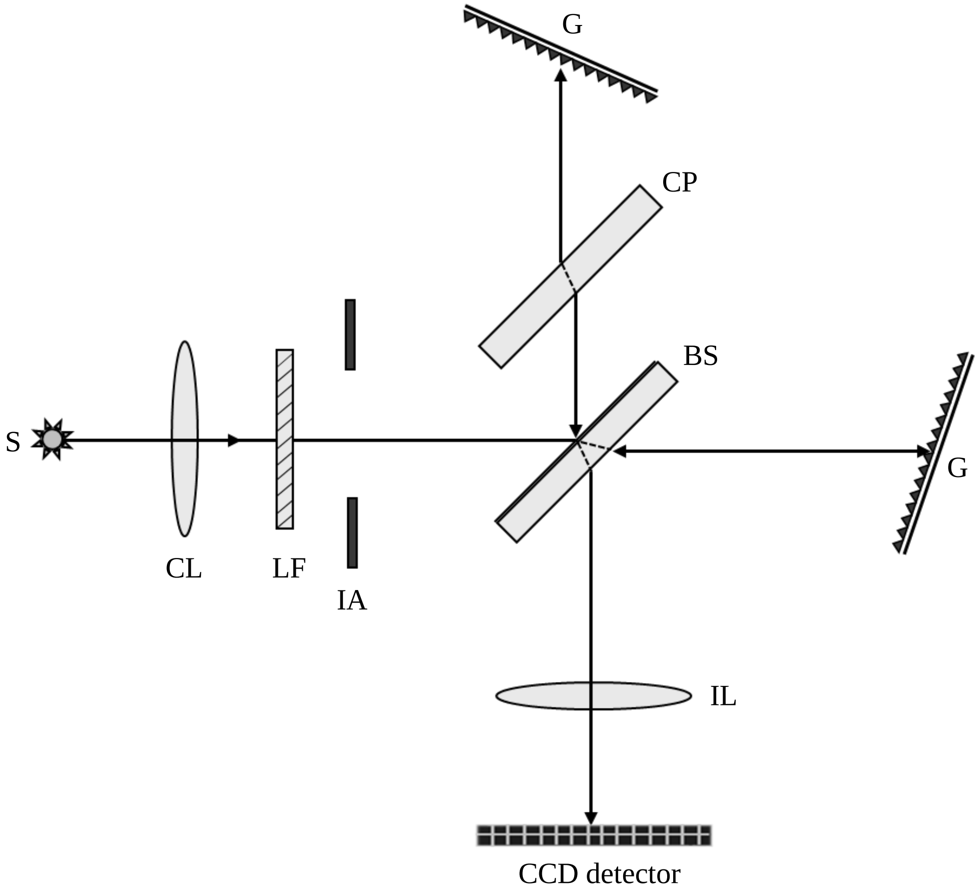

Figure 6.1. Schematic of the spatial heterodyne Raman spectrometer. (S) Light source, (CL) Collection/collimated lens, (LF) Laser rejection filter, (IA) Iris/Input Aperture, (BS) Beamsplitter, (CP) Compensator plate, (G) Grating, (IL) Imaging lens.

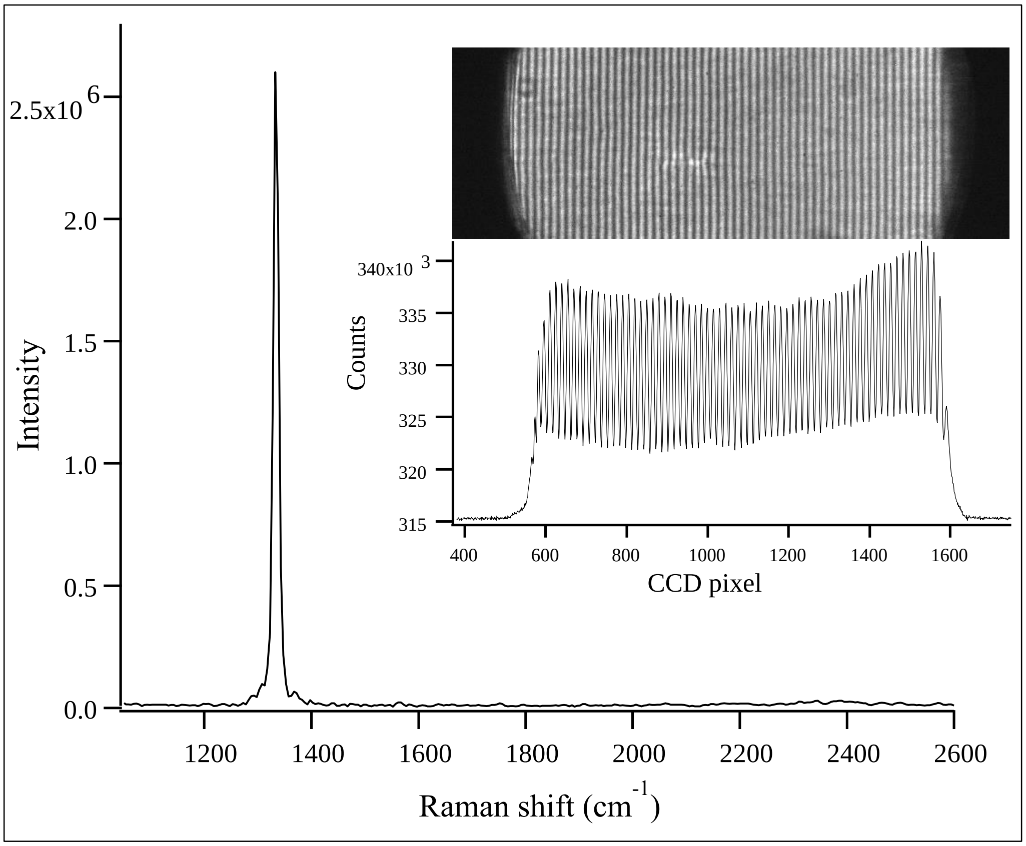

Figure 6.2. SHRS Raman spectrum of diamond measured illuminating 10 mw 244 nm laser for 10 s with improved SHRS design. The interferogram image and its cross section are shown in inset. The Littrow was set at 1050 cm$^{-1}$.

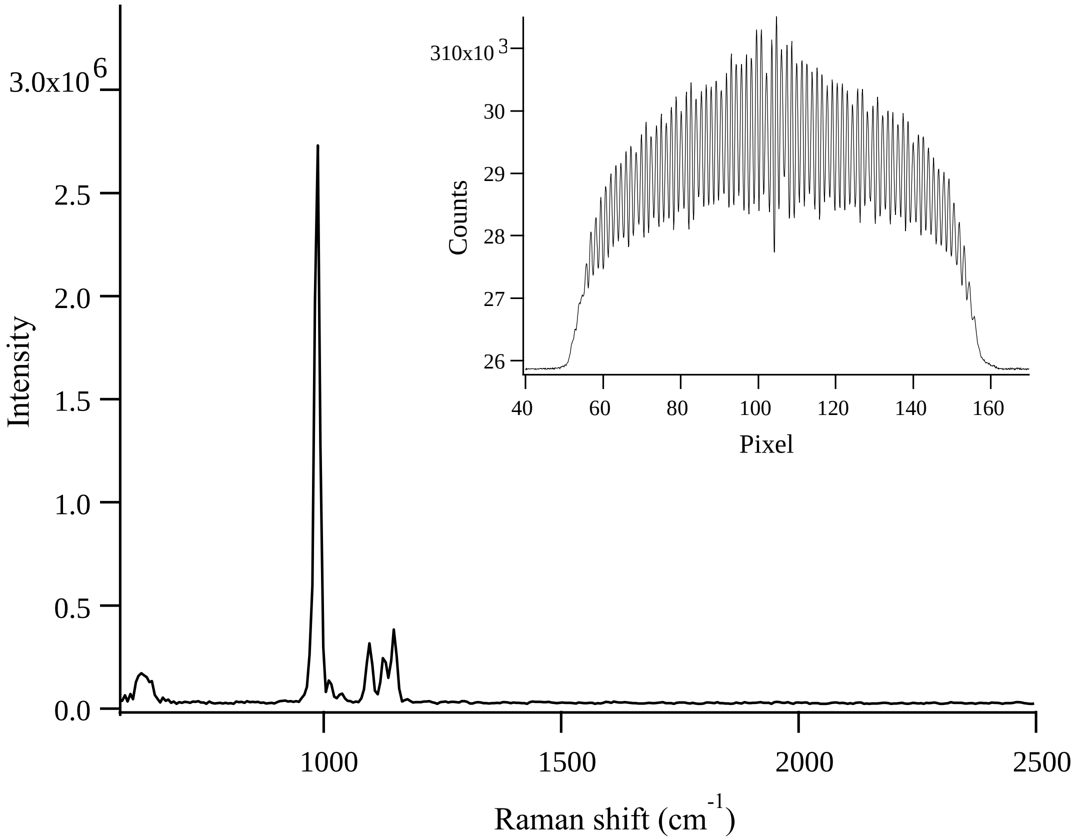

Figure 6.3. The SHRS Raman spectrum of $Na_2SO_4$ spectrum, which is the Fourier transform of the image cross section intensity shown in top inset. The integration time is 10 s with 244 nm 8mW laser power at the sample and Littrow is ~500 $cm^{-1}$.

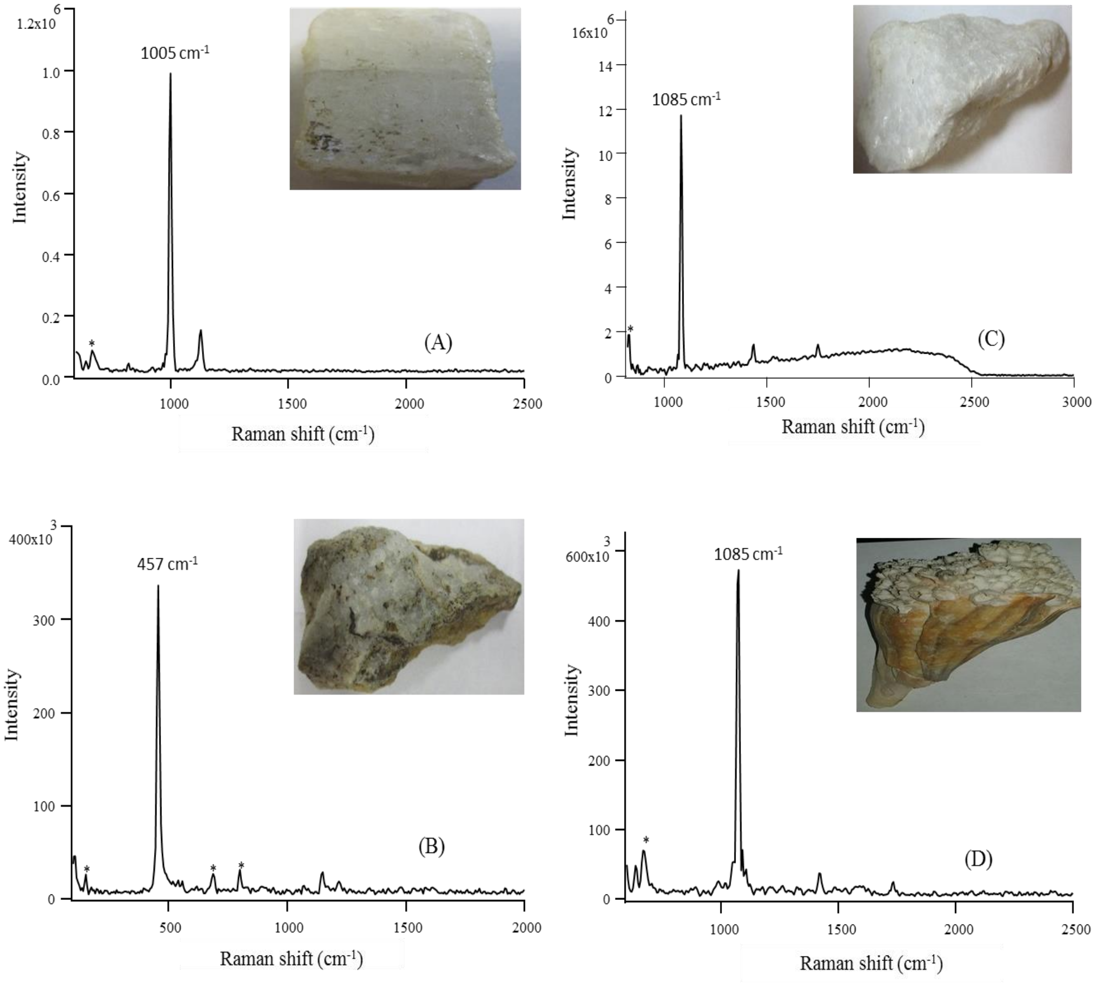

Figure 6.4. Raman spectra of rocks and minerals with major constituents of (A) Gypsum, (B) Quartz, (C) calcite, (D) snail shell. The spectra were obtained by illuminating 10 mW, 244 nm laser at the samples for 30 seconds. The major Raman peak of each samples are labelled.

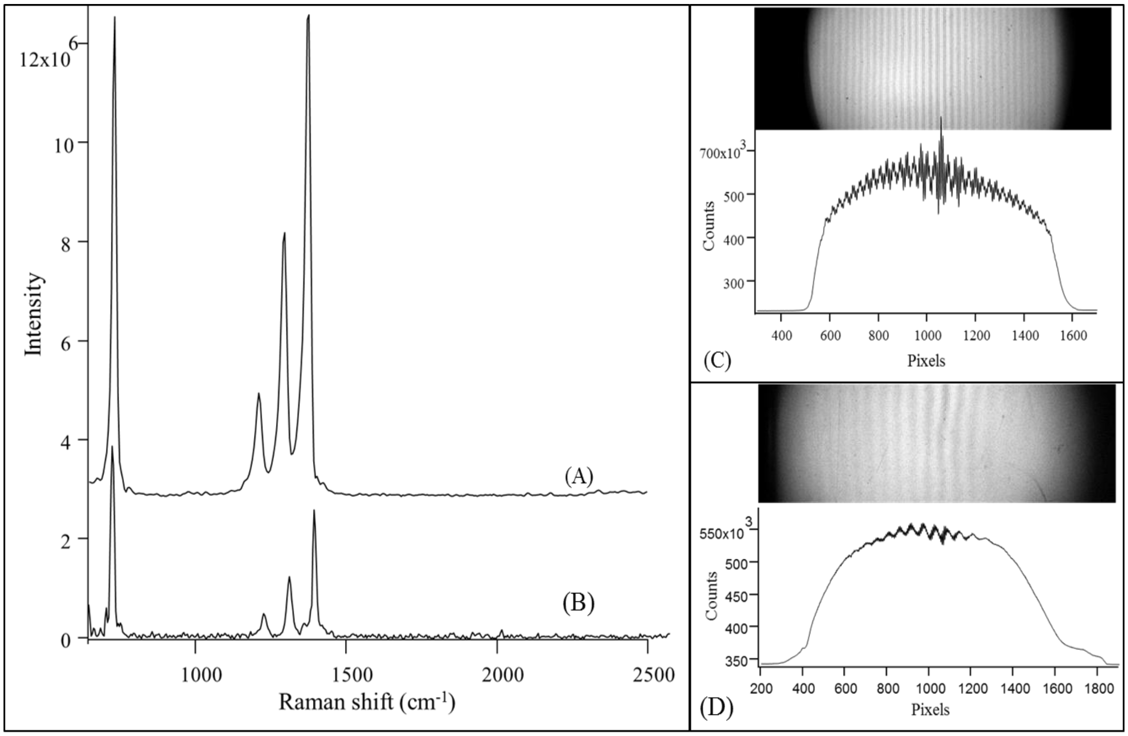

Figure 6.5. Raman Spectra of Teflon measured using 244 nm laser excitation with the SHRS of two different designs (A) with plate BS (B) with cube BS. The experimental conditions including the laser power (5 mW), acquisition time (30 s) and Littrow position (~700 cm$^{-1}$) were same for both measurements. Figure (C) and (D) show the corresponding interferogram fringe image and image cross section for plate BS and cube BS respectively.

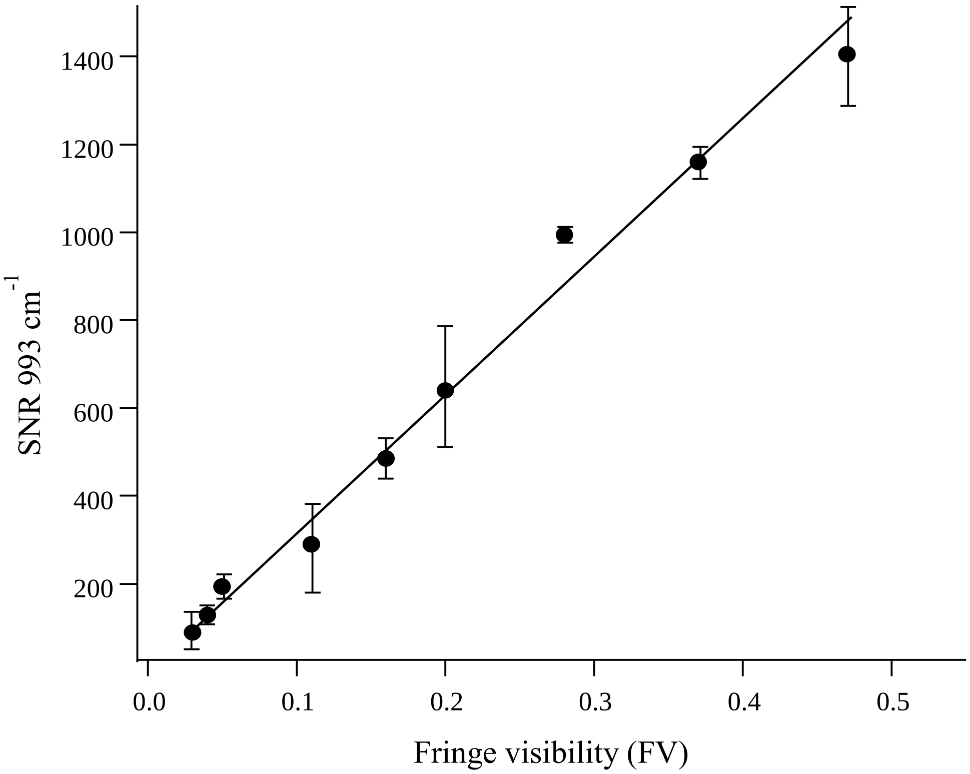

Figure 6.6. A plot showing the effect of fringe visibility of an interferogram on the SNR of reconstructed spectrum. The plot was obtained by recording the interferogram by moving one of the gratings off from its zero path difference position. The sample was $Na_2SO_4$ and other experimental conditions include 8 mW 244 nm laser and 10 s acquisition time. The figure in inset shows the change in the 993 $cm^{-1}$ intensity with fringe visibility.

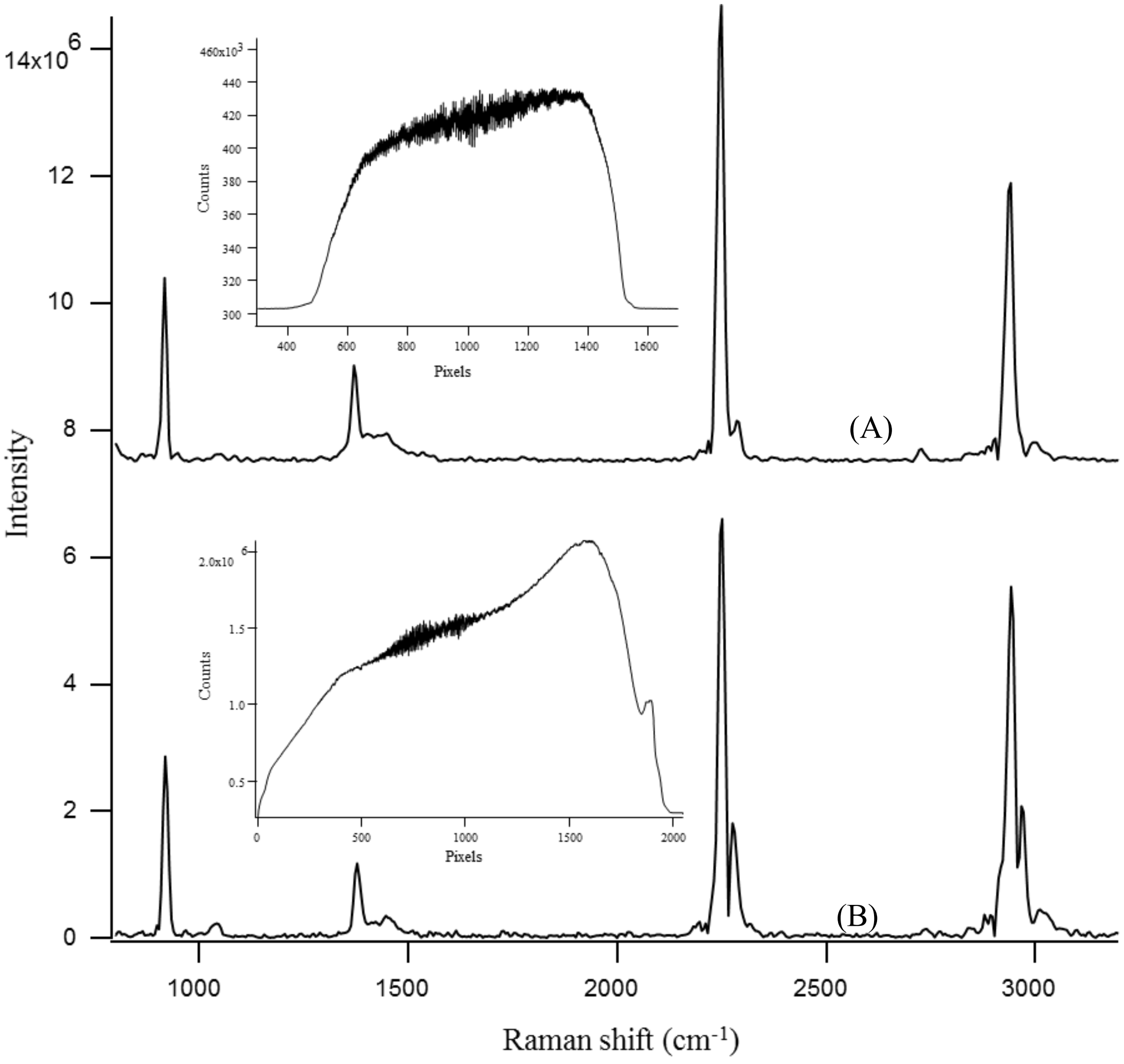

Figure 7. Acetonitrile interferograms and Fourier recovered Raman Spectra measured using SHRS with (A) plate and (B) cube beamsplitter with Littrow set close to 800 cm$^{-1}$. The two measurements were carried out in different experimental conditions. For the measurement involving a plate beamsplitter, 244 nm 6 mW laser was illuminated on the sample for 10 s. For the measurement involving a cube beamsplitter, 244 nm 13 mW laser was illuminated on the sample for 30 s.

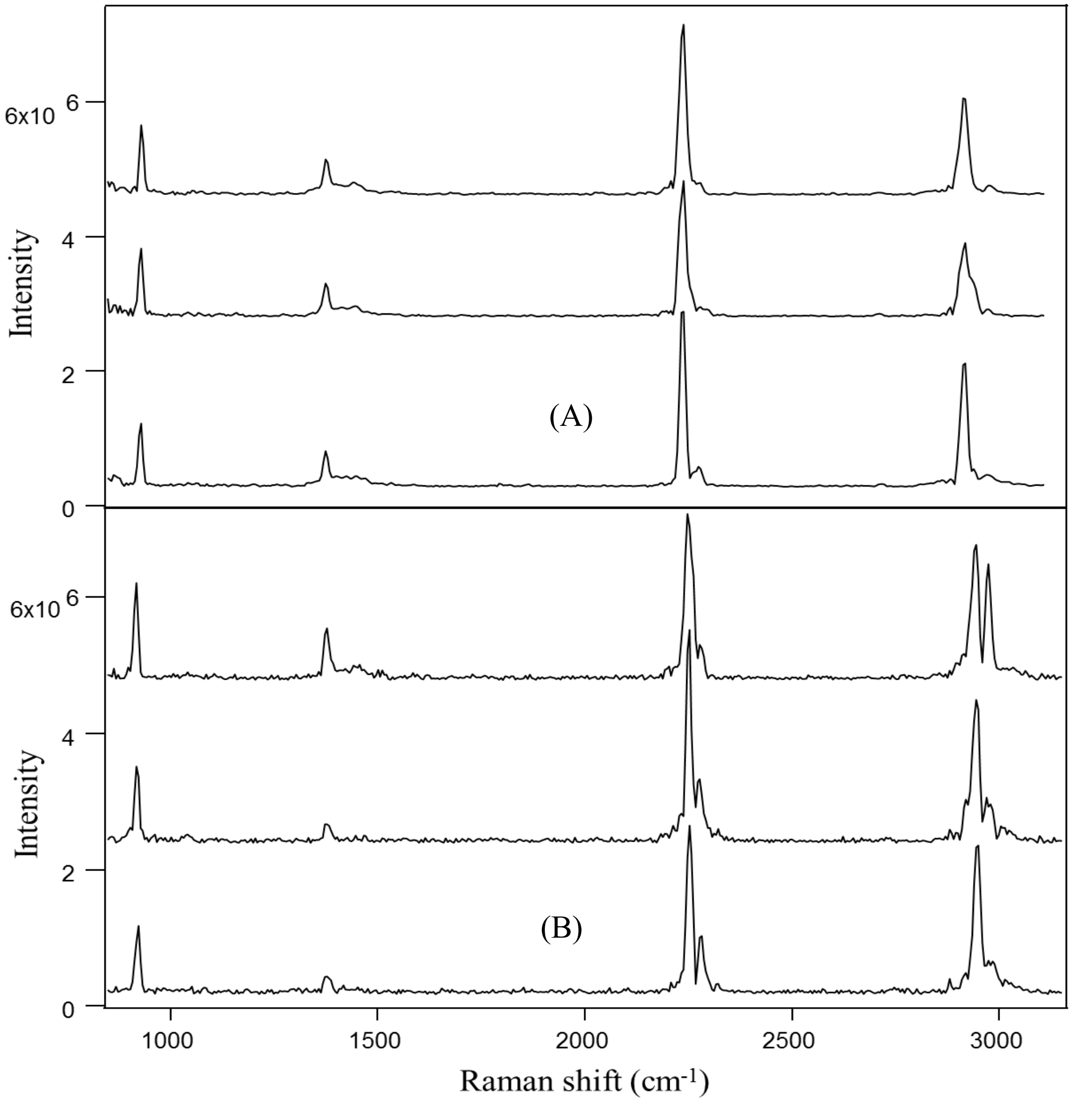

Figure 6.8. The Raman spectra of acetonitrile generated by partitioning the interferogram into three symmetrical halves along Y-axis (vertical) and applying a Fourier transform to each halves individually and correspond to SHRS with (A) a plate beamsplitter (B) a cube beamsplitter. For the CCD camera with 512 pixels along Y- axis, the top spectrum corresponds to 512-341 pixels, the middle spectrum corresponds to 341-170 pixels and the bottom spectrum corresponds to 170-1 pixels

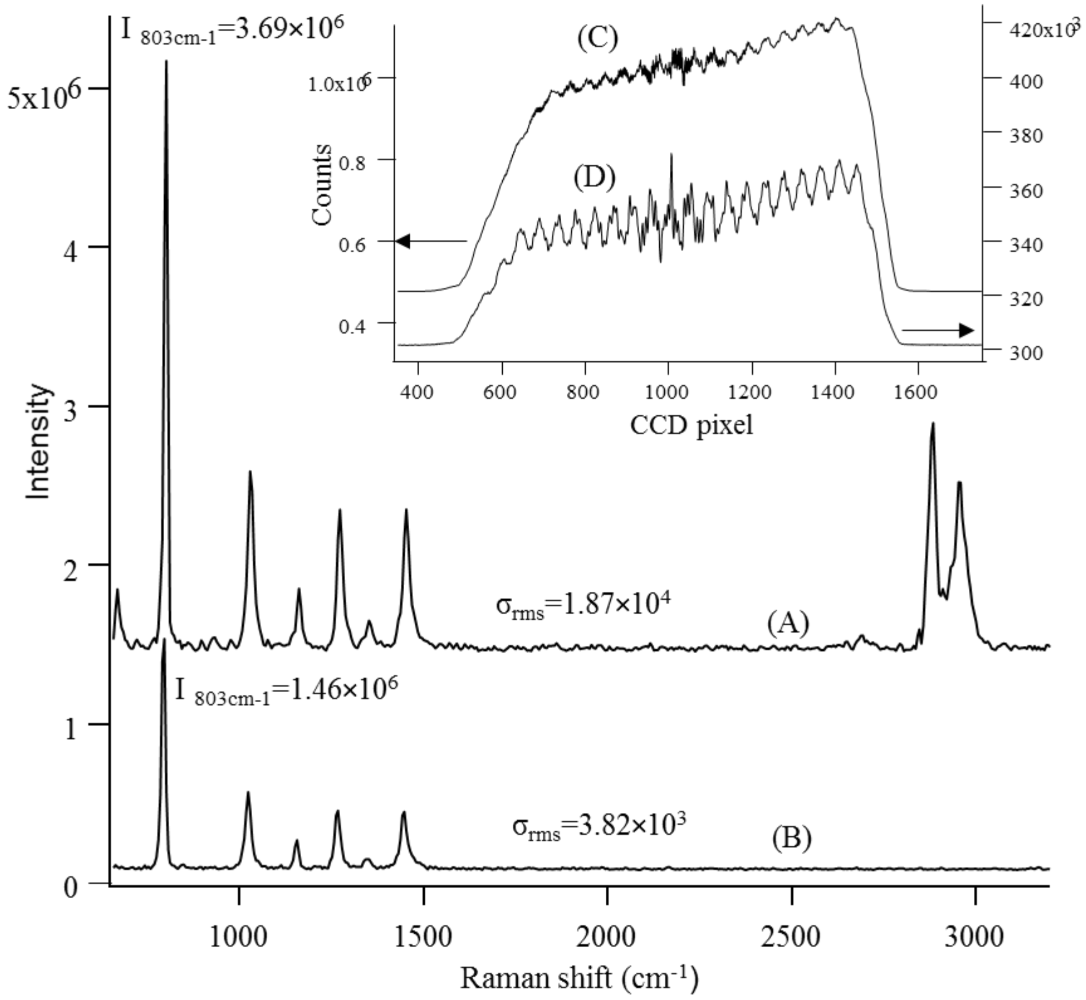

Figure 6.9. SHRS Raman spectrum of cyclohexane measured over (A) wide spectral range (B) limited spectral range using 254 nm bandpass filter. The spectra were acquired using 9 mW, 244 nm laser with 10 s acquisition time. Inset: the cyclohexane's interferogram measured over (C), wide spectral range (D) limited spectral range. The arrows above each interferograms refer to the appropriate intensity axis for that spectrum. The spectra and interferogram cross sections are offset vertically for clarity.

# Appendix A

## Permission to Reprint Chapter 3

**Title:** Deep-Ultraviolet Raman Measurements Using a Spatial Heterodyne Raman Spectrometer (SHRS):

**Author:** Nirmal Lamsal, S. Michael Angel

**Publication:** Applied Spectroscopy

**Publisher:** SAGE Publications

**Date:** 05/01/2015

Copyright © 2015, © SAGE Publications

**If you're a copyright.com user,** you can login to RightsLink using your copyright.com credentials. Already **a RightsLink user** or want to learn more?

**Gratis Reuse**

- Without further permission, as the Author of the journal article you may:
    - post the accepted version (version 2) on your personal website, department's website or your institution's repository. You may NOT post the published version (version 3) on a website or in a repository without permission from SAGE.
    - post the accepted version (version 2) of the article in any repository other than those listed above 12 months after official publication of the article.
    - use the published version (version 3) for your own teaching needs or to supply on an individual basis to research colleagues, provided that such supply is not for commercial purposes.
    - use the accepted or published version (version 2 or 3) in a book written or edited by you. To republish the article in a book NOT written or edited by you, permissions must be cleared on the previous page under the option 'Republish in a Book/Journal' by the publisher, editor or author who is compiling the new work.
- When posting or re-using the article electronically, please link to the original article and cite the DOI.
- All other re-use of the published article should be referred to SAGE. Contact information can be found on the bottom of our 'Journal Permissions' page.

# Appendix B

## Permission to Reprint Chapter 5

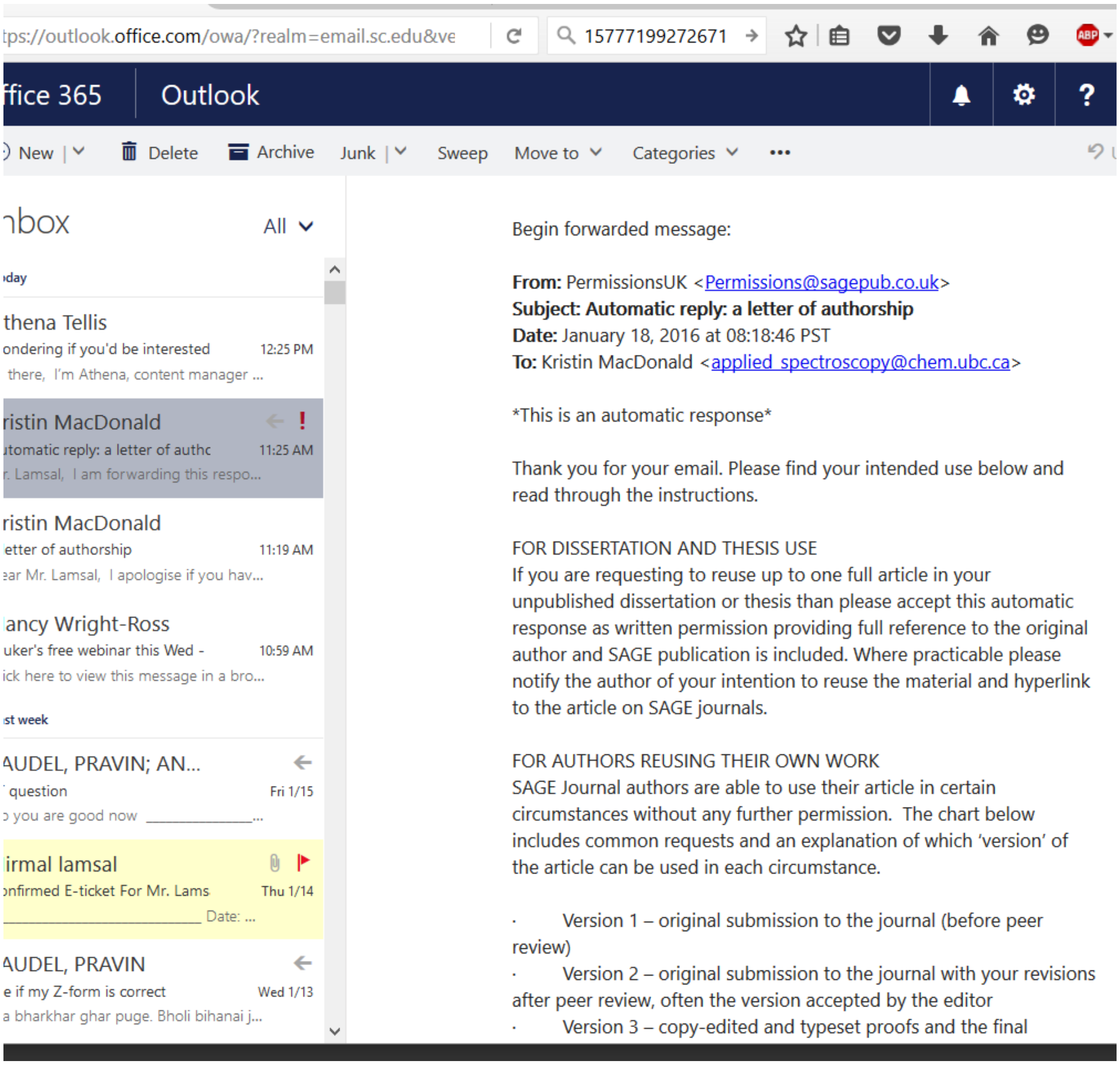

Begin forwarded message:

**From:** PermissionsUK <Permissions@sagepub.co.uk>
**Subject: Automatic reply: a letter of authorship**
**Date:** January 18, 2016 at 08:18:46 PST
**To:** Kristin MacDonald <applied_spectroscopy@chem.ubc.ca>

*This is an automatic response*

Thank you for your email. Please find your intended use below and read through the instructions.

FOR DISSERTATION AND THESIS USE
If you are requesting to reuse up to one full article in your unpublished dissertation or thesis than please accept this automatic response as written permission providing full reference to the original author and SAGE publication is included. Where practicable please notify the author of your intention to reuse the material and hyperlink to the article on SAGE journals.

FOR AUTHORS REUSING THEIR OWN WORK
SAGE Journal authors are able to use their article in certain circumstances without any further permission. The chart below includes common requests and an explanation of which 'version' of the article can be used in each circumstance.

- Version 1 – original submission to the journal (before peer review)
- Version 2 – original submission to the journal with your revisions after peer review, often the version accepted by the editor
- Version 3 – copy-edited and typeset proofs and the final